Diese Arbeit wurde vorgelegt am
Lehrstuhl für Mathematik (MathCCES)

Modellierung der zweidimensionalen Röntgenintensitätsverteilung in der Elektronenstrahl-Mikroanalyse

Modelling the Two-dimensional X-ray Intensity Distribution in Electron Probe Microanalysis

Masterarbeit
Simulation Sciences

May 2020

Vorgelegt von
Presented by

Gaurav Anantha Kumar Achuda
RWTH Aachen University
Matrikelnummer: 384671
gaurav.achuda@rwth-aachen.de

Erstprüfer
First examiner

Prof. Dr. Manuel Torrilhon
Lehrstuhl für Mathematik (MathCCES)
RWTH Aachen University

Zweitprüfer
Second examiner

Dr. rer. nat. Silvia Richter
Gemeinschaftslabor für Elektronenmikroskopie
RWTH Aachen University

Eigenständigkeitserklärung

Hiermit versichere ich, dass ich diese Masterarbeit selbständig verfasst und keine anderen als die angegebenen Quellen und Hilfsmittel benutzt habe. Die Stellen meiner Arbeit, die dem Wortlaut oder dem Sinn nach anderen Werken entnommen sind, habe ich in jedem Fall unter Angabe der Quelle als Entlehnung kenntlich gemacht. Dasselbe gilt sinngemäß für Tabellen und Abbildungen. Diese Arbeit hat in dieser oder einer ähnlichen Form noch nicht im Rahmen einer anderen Prüfung vorgelegen.

Aachen, im May 2020

GAURAV ANANTHA KUMAR ACHUDA

Abstract

Achieving high spatial resolution with Electron Probe Microanalysis requires robust matrix correction procedures. Matrix corrections can be performed if the generated X-ray intensity distribution ϕ in the material sample is known or can be approximated. So far, only empirical models that approximate this distribution along the vertical axis, denoted by $\phi(\rho z)$, have been developed and studied. The aim of this project is to develop an empirical model that describes the distribution in two dimensions. An empirical model based on a skewed generalised normal distribution that approximates $\phi(\rho r, \rho z)$, which describes the distribution along the radial and vertical directions, is proposed. The model is tested and the model parameters are estimated by performing curve fitting on a large set of generated X-ray intensity distribution data acquired from Monte-Carlo simulations. It is shown that there is good agreement between the fitted model and the data acquired from Monte-Carlo simulations.

Acknowledgements

Firstly, I would like to thank Prof. Dr. Manuel Torrilhon for enabling this project by coordinating it as my supervisor and examiner. I'm grateful for his support and collaboration during the course of the project.

I am greatly indebted Dr. Silvia Richter, under whom I have worked as student assistant for 18 months. She provided me with this project and has guided and mentored me throughout the project with great patience and compassion, for which I'm very thankful.

I would like to extend my gratitude to Jonas Bünger who helped me get started with the project by introducing me to the `NISTMonte` Monte-Carlo program and provided me with valuable advice and insights in the many meetings during the course of the project. I would also like to thank Dr. Philippe Pinard who has collaborated in the project and has advised me through web conferencing.

I am grateful to all the faculty and staff at RWTH Aachen who have influenced my educational journey at the institution during my Master's Program. Special thanks to my colleagues from the Simulation Sciences program who have made this journey fun and have supported and guided me when needed. Finally, I would like to wholeheartedly thank my family and friends for providing me much needed support and encouragement during the entire study program.

Contents

List of Figures

List of Tables

List of Algorithms

1 Introduction

Electron Probe Microanalysis is a non-destructive technique for elemental and structural analysis of very small materials at the micron and sub-micron scale. The technique involves bombarding a material with a stream of electrons and analysing the emitted X-rays of specific characteristic wavelengths. The tool used for electron probe microanalysis (EPMA) is called an Electron Microprobe.

1.1 Electron Probe Micro Analyser

In construction the Electron Microprobe is very similar to a Scanning Electron Microscope with the addition of several Energy Dispersive Spectrometers, Wavelength Dispersive Spectrometers (WDS) and an electron beam current which is stabilized for X-ray analysis. A modern electron microprobe typically consists of an electron column, a control console and a detector subsystem.

Within the electron column an electron gun generates electrons and accelerates them to energies in the range of 0.1 - 30 keV. A set of electron lenses collimate and focus the generated electron beam into a very small spot ($<$ 10 nm) on the test sample. The sample is mounted on a stage at the bottom of the electron column. A vacuum is maintained inside the electron column to minimise scattering of the electrons in the beam. Electron microprobes are also often equipped with optical lenses and cameras to observe the specimen and perform any necessary preliminary tests which might be necessary to fulfil the Rowland circle condition. For analysis, the electron beam is generally scanned across the specimen surface using deflection coils or scanning is performed by moving the stage. A control console is used to control the scanning of the beam or the positioning of the stage, respectively.

The interaction of the electron beam with the test sample can produce a variety of signals such as - heat, continuum X-ray radiation (bremsstrahlung), characteristic X-ray radiation, secondary electrons, back-scattered electrons, and Auger electrons. Specialized detectors can be used to detect each of these signals. The characteristic X-rays are of primary interest for X-ray microanalysis. These X-rays are detected and their intensities measured using energy dispersive or wavelength dispersive spectrometers. The measured signals are fed to a computer for imaging and further qualitative and quantitative analysis.

1.1.1 Characteristic X-Rays

The electrons from the electron beam enter the test sample and interact with the material in the form of a series of elastic and inelastic collisions with the material atoms until the kinetic energy of the electrons drop to a very low level or they exit the sample. An electron with a high enough kinetic energy can impart its kinetic energy

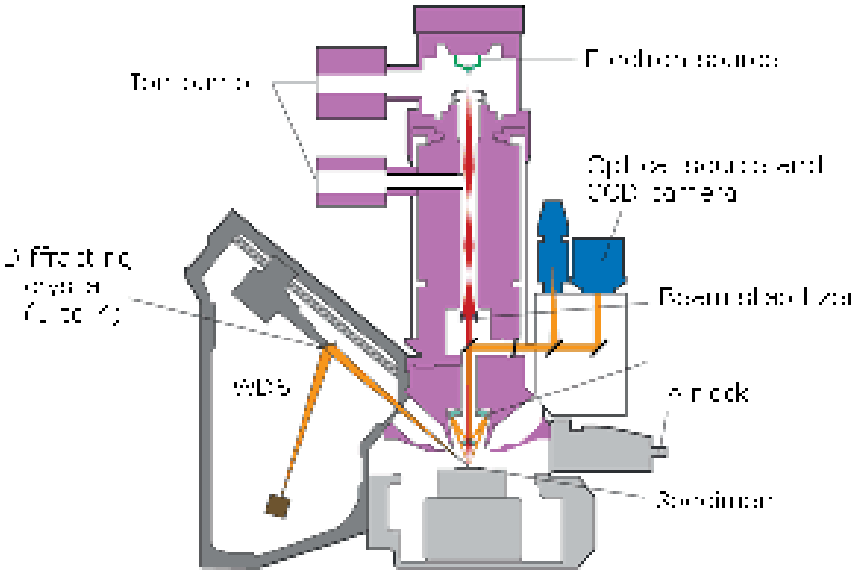

Figure 1: A schematic of an Electron Probe Micro Analyser from CAMECA Science & Technology Solutions [61]

to an inner shell electron of an atom in the sample and knock it out of its shell. This creates a vacancy in such a shell, which is unstable and hence, must be filled by a shell electron of higher energy or a free electron. When an electrons jumps from a higher energy shell to a lower energy shell, it emits energy in the form of a photon. In such interactions, the wavelength of the emitted photon is determined by the energy gap between the shells jumped by the electron. These emitted photons lie in the X-ray range of the electromagnetic spectrum. Since every element has a unique electron structure the emitted X-rays have wavelengths that are characteristic to the scattering element.

The emitted X-rays can get absorbed within the material, result in the emission of other characteristic X-rays through fluorescence or radiate out of the material. The emitted X-rays can be detected with the two types of spectrometers introduced earlier. Wavelength dispersive spectrometers (WDS) operate based on the principle of Bragg's diffraction and use crystals to separate specific wavelengths for the X-ray detectors. Energy dispersive spectrometers (EDS) use solid state semiconductor detectors that convert X-ray energy into voltage pulses. EDS systems are comparitively faster and can detect X-rays of all elements. Wavelength dispersive spectrometers, on the other hand, are more sensitive and have better signal to noise ratios, but cannot be used for very light elements such as H, Li and Be [24, p. 486]. Newer types of WDS system that use gratings and Bragg's reflection law for wavelength separtion are capable of detecting X-rays from Li and Be [55].

1.1.2 Applications

In bulk materials electron microprobe microanalysis can be used for determination of phase compositions and analysis of elemental distributions and can be used for a variety of materials and surfaces such as: semiconductors, metals, ceramics, coatings, composites, surface treated materials, minerals and glass [54]. In thin films and coatings electron probe microanalysis can be used for quantitative determination of composition and thicknesses of the thin layers. It can also be used for quantitative analysis of complex multilayer systems[54].

1.2 Quantitative X-Ray Analysis

With wavelength dispersive spectrometers, electron microprobes can not only be used for qualitative analysis like identifying constituent elements in a sample but also for quantitative analysis such as identifying the chemical composition and several structural features.

The standard procedure for quantitative X-ray analysis involves detecting the intensities of characteristic X-rays from the sample material and intensities of the same X-rays from a material with known composition wich is referred to as a standard. The ratio of sample X-ray intensities to the standard X-ray intensities, referred to as k-ratios, are then computed. Measuring k-ratios helps in eliminating instrumental factors and other factors that are common to the specimen and the standard [14][24, p. 396].

At first glance k-ratios corresponding to a specific element can seem to be perfect indicators of the mass fraction of that element relative to the known composition of the standard. This was first noted by Raymond Castaing [14] and is called Castaing's "first approximation to quantitative analysis". The composition of a specific element in the unknown sample and the standard can thus be represented as

$$C_A/(C_A)_{std} = I_A/(I_A)_{std} = k_A \tag{1}$$

where C_A and $(C_A)_{std}$ are the mass fractions of the element A in the unknown sample and the standard respectively; I_A and $(I_A)_{std}$ are the measured intensities for a characteristic X-ray of the element A in the unknown sample and the standard respectively; k_A is the corresponding k ratio.

But careful measurements of known compositions have shown that there are significant deviations between k-ratios and ratios of mass fractions [23][24, p. 402]. It has been found that for most quantitative chemical analysis the measured intensities from specimen and standard must be corrected for differences in electron backscatter, density, X-ray cross section, energy loss, absorption, fluorescence, etc. [24, p. 402]. These effects are collectively called Matrix effects.

1.3 Matrix Correction Methods

There are many factors that dictate the intensity of generated and thereby detected characteristic X-rays as discussed earlier and as a result, correcting for the matrix effects is not trivial. The most common matrix correction methods employ some form of iterative optimization technique and a function or a computational model which predicts the emitted X-ray intensities for a known sample composition. [24, pp. 402–420]

1.3.1 ZAF Method

One of the most popular correction procedures has been the ZAF procedure [24, p. 402] [46]. It was first conceptualised by Philibert and Tixier [44]. In this procedure the corrections required to compensate for matrix effects are classified into three types - correction for atomic number Z, correction for absorption A and correction for fluorescence F.

Atomic number correction factor Z: When a sample is bombarded with an electron beam, electrons from the beam enter into the sample and scatter repeatedly resulting in, among other phenomena, the generation of characteristic X-rays. The scattering behaviour in a material and hence the interaction volume of electrons is largely dependent on the atomic number, and hence require an atomic number based correction.

Absorption correction factor A: Only a part of the X-rays generated within a material sample get emitted. The rest are absorbed on their way out of the material. The absorption correction factor accounts for this.

Fluorescence correction factor F: Sometimes high energy characteristic X-rays generated within the material can induce ionizations in other atoms and result in the emission of other characteristic X-rays. This phenomenon is called fluorescence. This factor is usually calculated based on the model provided by Reed [50].

Once the Z, A and F factors are know, they can be plugged into equation (1), which yields

$$C_A/(C_A)_{std} = [ZAF]_A I_A/(I_A)_{std} = [ZAF]_A k_A. \tag{2}$$

Thus the unknown concentration of element A in the sample can be calculated as

$$C_A = [ZAF]_A k_A (C_A)_{std} \tag{3}$$

This method has the advantage of being very simple and fast. But because of its simplicity, it is less flexible and not suitable for non-homogeneous or other unusual material samples.

1.3.2 Analytical Methods

As discussed earlier, there exists a finite electron interaction volume within the material were most of the characteristic X-rays are produced. The generated intensity of x-rays varies within this region. Generated charecteristic X-ray photons are often absorbed on their path to the detector and the location where they are generated determines their likelihood of being absorbed. Hence, if the generated X-ray intensity distribution is known the total generated and the total emmited X-rays accounting for absorption can be determined. On the other hand the fluorescence factor is less affected by changes in the ionization distribution. This is because volume of the sample affected by fluorescence, i.e. X-rays generated by other generated X-rays, is 1-2 orders of magnitude greater than the interaction volume of the electron beam [42]. Hence, fluorescence is generally handled separately.

This method is often called the $\phi(\rho z)$ method. It gets this name from the notation, $\phi(\rho z)$, used to describe the generated X-ray intensity distribution with respect to the mass depth ρz. The mass depth ρz is the product of mass density ρ and the depth z. The concept of $\phi(\rho z)$ was first introduced by Castaing [14] and was popularized after formulations by Packwood and Brown [42] and Pouchou and Pichoir [46]. $\phi(\rho z)$ is related to the total emitted X-ray intensity I_A as

$$I_A \propto C_A \int_0^\infty \phi(\rho z) \exp(-\mu_A \rho z \csc \Psi) \mathrm{d}\rho z, \tag{4}$$

where C_A is the mass fraction of element A and $\exp(-\mu_A \rho z \csc \Psi)$ is the correction for absorption; μ_A is the mass absorption coefficient for the X-ray of interest in the material and Ψ is the take off angle to the detector (i.e. the angle of the detector with respect to the sample surface). The emitted X-ray intensity for a standard and thus the k-ratio is given by [14]

$$k_A = \frac{I_A}{(I_A)_{std}} = \frac{C_A \int_0^\infty \phi(\rho z) \exp(-\mu_A \rho z \csc \Psi) \mathrm{d}\rho z}{(C_A)_{std} \int_0^\infty \phi_{std}(\rho z) \exp\left(-(\mu_A)_{std} \rho z \csc \Psi\right) \mathrm{d}\rho z}. \tag{5}$$

The mass fraction C_A can be determined if k-ratio, $(C_A)_{std}$, $\phi(rhoz)$, $\phi_{std}(\rho z)$ and other constants involved are known. $\phi(\rho z)$ method can also resolve features like discontinuities or heterogeneities along the depth as long as the $\phi(\rho z)$ descriptions for such cases are available. One or more compositional or structural features can be determined from an equal or greater number of measured k-ratios. An optimization algorithm is generally used to determine the unknown features based on k-ratios computed from the $\phi(\rho z)$ description.

Numerical Methods: Numerical methods can be used to simulate electron trajectories or transport within a material sample and the corresponding k-ratio can predicted.

Monte-Carlo simulations, which will be discussed in detail in section 2, are most commonly employed for this purpose. Features of the sample can be determined using iterative optimization algorithms which use Monte-Carlo simulations for forward calculations [45]. The Monte-Carlo simulations try to simulate the physics of electron motion and scattering. They are thus more accurate than any of the methods discussed before. They are also very versatile, enabling the use of any kind of sample. Monte-Carlo simulations, however, are stochastic in nature and thus introduce stochastic noise, which can make optimization harder. Deterministic formulations based on transport equations that do not possess this problem have also been developed in recent years [38][12].

1.4 Empirical models for generated X-ray intensity distribution

1.4.1 Why do we need empirical models?

Numerical methods such as the Monte-Carlo method are very good at predicting the physical behaviour of electrons and thus are compelling choices for matrix correction. Modern computers can run a single Monte-Carlo simulation pretty quickly. But complex problems require iterative optimization routines for matrix corrections, which require multiple simulations to be run in a sequence. X-ray data acquired by an electron probe is also, typically, in the form of 2D X-ray map containing many data points and computing matrix corrections for each of these points can result in a very large number of simulations to be run. In such cases, Monte-Carlo methods are just too slow. Empirical models for generated X-ray intensity distribution can thus be a good compromise between speed and accuracy required for such iterative matrix correction procedures. In fact, numerical methods such as Monte-Carlo simulations can be used to build and improve the empirical models so as to very closely mimic their output.

1.4.2 The Story So Far

Although, the generated electron intensity distribution ϕ can be expressed in three or two dimensions, only the one-dimensional distribution $\phi(\rho z)$ defined along the mass depth has been popularly studied and analysed. $\phi(\rho z)$ was originally defined by Castaing [14] as : $\phi(\rho z)$ is the ratio of the generated X-ray intensity in an elemental layer of mass thickness $\mathrm{d}\rho z$ at a mass depth ρz to that of an identical but unsupported layer.

One of the earliest popular empirical descriptions of $\phi(\rho z)$ was provided by Philbert [43]. The analytical form of the Philbert model is given by

$$\phi(\rho z) = A \exp(-\sigma \rho z) \left[1 - \exp\left(-\frac{\sigma \rho z}{h}\right)\right] \tag{6}$$

where A is a constant, σ is the Lenard coefficient and $h = 1.2A/Z^2$; Z is the atomic number, A is the atomic mass of the material sample [42]. This model was popular

and extensively used when there was very little information and experimental data on the real depth distribution of ionization. This model however had an obvious flaw in that $\phi(\rho z)$ was 0 at $\rho z = 0$, while the very definition of $\phi(\rho z)$ according to Castaing requires $\phi(\rho z = 0)$ to be greater than or equal to 1.

Later Packwood and Brown improved on this model and provided a modified Gaussian expression [42]. It was given by

$$\phi(\rho z) = \gamma_0 \exp\left\{-\alpha^2(\rho z)^2\left[1 - \left(\frac{\gamma_0 - \phi_0}{\gamma_0}\right)\exp\left(-\beta\rho z\right)\right]\right\} \tag{7}$$

They also provided empirical expressions for the constants γ_0, α, ϕ_0 and β based on physical arguments.

The most robust description of $\phi(\rho z)$ to date, however, was provided by Pouchou and Pichoir in the form of their "PAP" and "XPP" models [46]. The PAP model is constructed by stitching two parabolas together at a specific mass depth. The model was developed as to satisfy the following condition [46]:

- the integral must be equal to a certain value F,
- at the surface the correct $\phi(0)$ must be obtained,
- the maximum must be at certain mass depth R_m and
- the function must vanish with a horizontal tangent at the maximum range of ionization R_x.

These features are illustrated in figure 2.

Hence, they arrived at the following distribution.

$$\phi(\rho z) = \begin{cases} \phi_1(\rho z) = A_1 \cdot (\rho z - R_m)^2 + B_1 & 0 \leq \rho z \leq R_c \\ \phi_2(\rho z) = A_2 \cdot (\rho z - R_x)^2 & 0 \leq \rho z \leq R_c \end{cases}, \tag{8}$$

where the constants A_1, B_1 and A_2 can be computed from the known values of F, $\phi(0)$, R_m, and R_x [46]. Further they also provided a simplified model called XPP, which could be expressed in the form of exponentials as follows.

$$\phi(\rho z) = A \cdot \exp(-a\rho z) + [B\rho z + \phi(0) - A] \cdot \exp(-b\rho z) \tag{9}$$

The coefficients A, B, a, and b can also be computed from the values of the area of the distribution F, the value of $\phi(0)$, the slope p at $\rho z = 0$ and the average depth of ionization R [46] (see figure 2). The PAP model can also be used for stratified samples by simply computing the four basic parameters as if they were for a fictitious homogeneous material and using the PAP model as usual. The composition of the fictitious material can be determined using a special weighting procedure. A more detailed comparison of the different models can be found in [58].

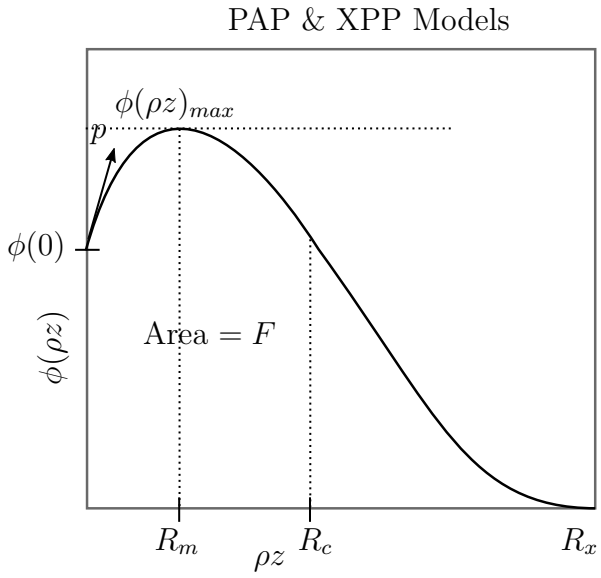

Figure 2: Features of the $\phi(\rho z)$ distribution as required by the PAP and XPP models.

1.4.3 Empirical Models in more Dimensions

Although $\phi(\rho z)$ is a very useful distribution to know, it can only resolve features in the vertical direction. When vertical layers are present in the material $\phi(\rho z)$ can cause mischaracterizations. For example, an element from an adjacent vertical layer might show up as a trace element in the current region. Also, a full three dimensional description of the distribution can be used as an alternative to the computationally more expensive Monte-Carlo simulations for complex matrix correction procedures.

Not much work is visible in literature related to ϕ in other dimensions (for example, $\phi(\rho x)$) or more dimensions (for example, $\phi(\rho x, \rho y, \rho z)$). Armstrong [2] investigated $\phi(\rho x, \rho y, \rho z)$ for micro-particles in order to account for side-scattering, i.e. energetic electrons leaving the material through the sides. The author proposed a simple approximation for the same as

$$\phi(\rho x, \rho y, \rho z) = \left[1 - \left|\frac{x}{D}\right| - \left|\frac{y}{D}\right| + \left|\frac{xy}{D^2}\right|\right] \phi(\rho z), \tag{10}$$

where D is the diameter of the micro-particle.

1.5 Scope of this Project

In this project we study and investigate various forms of the generated intensity distribution. We, particularly focus on the distribution $\phi(\rho r, \rho z)$ which is a description of the distribution along the mass radial distance and the mass depth. Further, we

attempt to obtain an empirical model for the same with the help of curve fitting on a generated database.

1.5.1 Generating data for Analysis and Curve Fitting

In order to develop an empirical function for a multi-dimensional description of the X-ray intensity distribution it is essential to have a set of data describing the distribution for known composition of materials. Physical approaches to obtaining this data include the so called "Tracer method" and "angular distribution method". Experimental methods are not suitable for generating large sets of X-ray intensity distribution data, especially in two and three dimensions because of the difficulties involved in preparing the samples and setting up the experiments. Hence, generating X-ray intensity distribution data from numerical simulations of the motion of energetic electrons in a material matrix can be a good alternative. Several studies (for example [36] [30] [33] [22] [20] [32]) have shown that Monte-Carlo methods can be used to reliably simulate the motion of energetic electrons in a material matrix by comparing simulated quantities with experimentally measured $\phi(\rho z)$ using tracer methods, back scattered electron production and/or continuum X-ray production. A Monte-Carlo simulation generates a random walk for the path of the electron through a material assuming randomly placed atoms. Electron-material interactions like scattering and ionizations are determined by random chance and probabilities. Due to the stochastic nature of the simulation, many electron paths need to generated and their effects be averaged to attain repeatability. Monte-Carlo simulations are also extremely versatile, i.e. it can be adopted for any shape or geometry of the sample with any composition of materials as long as the few fundamental characteristics of the material required for the algorithm are known. In the context of EPMA simulated electron trajectories can be used to approximate the distribution of ionization events. This can give a three dimensional description of the X-ray intensity distribution which is not easy to obtain experimentally without the use of destructive techniques.

2 The Monte-Carlo Method

2.1 Basics of the Monte-Carlo Method

Most Monte-Carlo implementations make use of two important assumptions in order to simplify computation [30]. They are as follows:

1. The angular deflections suffered by an electron and thereby the actual path traversed by the electron is mainly determined by the elastic scattering events in the material alone. Deflections caused from inelastic scattering events are assumed to be insignificant and hence often ignored.

2. The energy loss due to inelastic scattering events is assumed to be continuous. Since inelastic scattering events comprise of many interactions such as continuum X-ray generation, characteristic X-ray generation, Auger electron production and so on, modelling each of these interactions as distinct events can significantly increase computational time and complexity. A continuous energy loss of this kind as an electron travels from one point in the material to another was first modelled by Bethe [7].

These assumptions can be avoided and inelastic scattering events can be modelled similar to elastic scattering events as discrete scattering events, for added accuracy. But the gain in accuracy resulting from this is trivial compared to the negative impact on computational speed [30].

Further there are two popular techniques used to simulate elastic scattering events, which are as follows.

Single Scattering Model: The single scattering model tries, in principle, to simulate every elastic scattering event in an electron trajectory until the electron leaves the material or its energy falls below the simulation threshold. Some of the first implementations of this technique include those by Reimer et al. [52] and Murata et al. [39]. In this method a random mean path length is generated at every step of an electron trajectory and is used to displace the electron from its current position to the next. This method is, potentially, more accurate compared to the multiple scattering model which is discussed below [39] [30].

Multiple Scattering Model: In the multiple scattering model an analytical maximum trajectory length for electrons is first calculated. This can be done for example by integrating the Bethe energy loss ($\mathrm{d}E/\mathrm{d}s$). The total trajectory length is then divided into a small finite number of steps (say 50) and at each step multiple elastic scattering events are carried out based on Lewis' Multiple Scattering Theory [34]. Essentially, the effects of several scattering events that could have occured along the path of the electron during a step are summed up. Some of the first Monte-Carlo methods that were developed for the simulation of energetic electron in materials made use of this technique, for example [25] [8] [60]. The

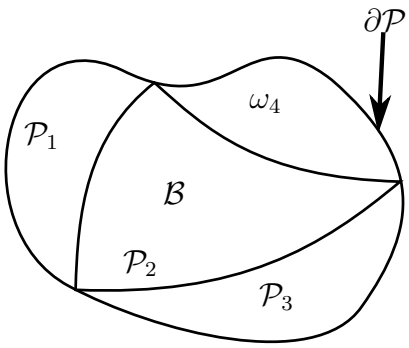

Figure 3: Material Sample: region $\mathcal{B}$ bounded by surface $\partial\mathcal{B}$

multiple scattering model has the benefit of being faster compared to the single scattering model because the number of steps in single electron trajectory can get very large in the single scattering method.

2.2 NISTMonte and NIST DTSA-II

Several implementations of the Monte-Carlo method for simulation of electron scattering are available today like `Monaco` [1], `PENELOPE` [59] and `PENEPMA` [35], `CASINO` [21], `WinX-Ray` [18] and `NIST DTSA-II` [57].

Among these programs, `NIST DTSA-II` was the most convenient for our purpose of generating ionization distribution data since it is available as source code and contains a large library of algorithms useful in electron probe quantitation called the `EPQ` library. `NIST DTSA-II` stands for National Institute of Standards and Technology Desktop Spectrum Analyser II. `NISTMonte` [56] was a stand-alone Monte-Carlo simulation tool which has now been incorporated into and replaced by `NIST DTSA-II`. The program is open source and is written in the Java programming language.

2.3 The Monte-Carlo Algorithm

The following is a brief overview of the Monte Carlo method used to simulate electron trajectories in the context of EPMA.

2.3.1 Material Sample

The material sample must be well defined as a three dimensional solid object during the setup of the simulation. Let $\mathcal{B}$ bounded by the surface $\partial\mathcal{B}$ be a the three dimensional

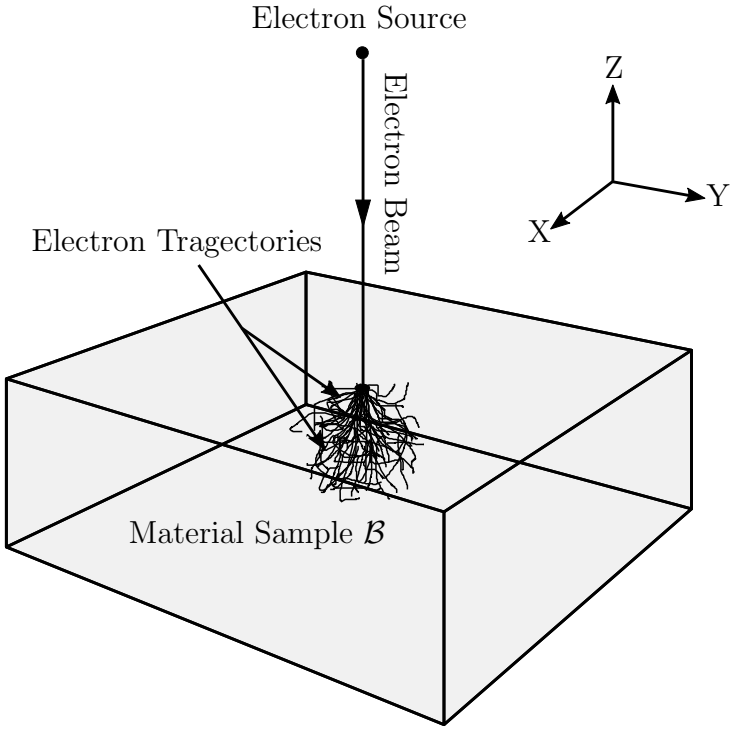

Figure 4: A simple experimental setup for Monte-Carlo simulations

region of space that defines the material sample. $\mathcal{B}$ can be made up of one or more non-overlapping sub-regions $\mathcal{P}_i$ with $i = 1, 2, \ldots, n_{\mathcal{B}}$ bounded by surfaces $\partial\mathcal{P}_i$ respectively, as illustrated in figure 3. The sub regions must satisfy the conditions: $\mathcal{P}_i \cap \mathcal{P}_j \equiv \partial\mathcal{P}_i \cap \partial\mathcal{P}_j \; \forall i \neq j$ and $\bigcup_{i=1}^{n_{\mathcal{B}}} \mathcal{P}_i = \mathcal{B}$. Every sub-region $\mathcal{P}_i$ must be homogeneous with mass density ρ_i and material compositions defined by atomic numbers Z_{iA} and corresponding mass fractions C_{iA}.

`NISTMonte` provides an interface to define custom shapes. The `EPQ` library also provides several standard shapes like spheres, cylinders, multi-planar shapes, etc. as templates. For a bulk sample it is convenient to choose simple cuboid region as $\mathcal{B}$. The cuboid should be, ideally, much larger than the interaction volume of the electron beam, so that electrons can only escape the material through back-scattering. We chose pure element homogeneous materials as our samples because they are of primary interest for us to obtain the initial function fits for $\phi(\rho r, \rho z)$. Figure 4 shows such a simple experimental setup.

2.3.2 Electron Beam

The shape of the electron beam, the beam energy E_0, the position $\boldsymbol{x}_0$ of the source and the direction $\boldsymbol{u}_0$ in which the beam is fired are required to define the electron beam.

Electron beam shape: There are three major parameters defining the shape of the electron beam - the convergence angle of the beam α_p, the distribution of the incident electrons on the sample surface and the associated beam diameter d_p. The convergence angle is a consequence of focusing the beam using electron lenses. The distribution of incident electrons is generally modelled as a bivariate Gaussian, where the d_p describes the standard deviation of the said Gaussian. In the case of a uniform distribution, d_p describes the actual diameter of the beam. In this project only a point beam with $\alpha_p = 0$ and $d_p = 0$ is used. Although this is not representative of the real electron beams, knowing the X-ray intensity distribution for a point beam gives us the flexibility of convoluting the distribution for any combination of beam parameters. In other words it helps us generalize the X-ray distribution.

Electron beam energy: Denoted by E_0, it is the energy of the electrons when they are generated at the source. It might be convenient to calculate the beam energy from an over-voltage ratio, denoted by U, because many of the properties of X-ray intensity distribution are tied to it. It is the ratio of the beam energy E_0 to the edge energy E_{nl} of the atomic shell whose vacancy when filled, results in the generation of the X-ray line of interest E_{nl}, i.e.

$$U = \frac{E_0}{E_{nl}}. \tag{11}$$

The position of the source : This is the point in three dimensional space $\boldsymbol{x}_0 \in \mathbb{R}^3$ from where the electrons start their trajectories.

Direction of the beam : This is the direction given by a unit vector $\boldsymbol{u}_0 \in \mathbb{R}^3$ in which electrons are fired from $\boldsymbol{x}_0$. It is more convenient to specify the direction in spherical coordinates as angles $\theta_0 \in [0, \pi]$ and $\phi_0 \in [0, 2\pi)$ for Monte-Carlo simulations. θ_0 is the polar angle, i.e. the angle between $\boldsymbol{u}_0$ and the positive Z axis in Cartesian coordinates. ϕ_0 is the azimuthal angle, i.e. the angle made by the projection of $\boldsymbol{u}_0$ on the XY-plane and a reference azimuth direction, which is by convention, the positive X-axis, and is measured in the anti-clockwise direction. For the setup shown in figure 4 where the beam is directed along the negative Z axis, $\boldsymbol{u}_0 = [0, 0, -1]$ in Cartesian coordinates. In spherical co-ordinates, it would be equivalent to $\theta = \pi$ and $\phi \in [0, 2\pi)$ or $\phi = 0$ without loss of generality.

In `NISTMonte`, the electron beam is set up by defining an electron gun (`ElectronGun`) object which stores these parameters and is responsible for initializing electron trajectories.

2.3.3 State of the Electron

It might be necessary to keep track of the following properties of an electron while simulating its trajectory: its position $\boldsymbol{x} \in \mathbb{R}^3$, its energy E, its direction given by

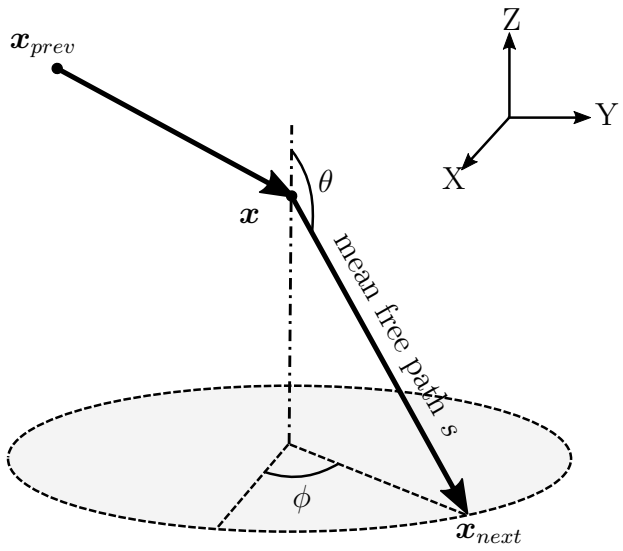

Figure 5: Monte-Carlo simulation: electron trajectory step

$\theta \in [0, \pi]$ and $\phi \in [0, 2\pi)$, the region of space $\mathcal{R}$ the electron is currently in. θ and ϕ are defined in the same way as in the previous section (2.3.2). At the start of each electron trajectory, an electron object is created by the electron gun and is initialized with $\boldsymbol{x} = \boldsymbol{x}_0$, $E = E_0$, $\theta = \theta_0$ and $\phi = \phi_0$. For the region $\mathcal{R}$, a vacuum region $\mathcal{V}$ defining the chamber is created. This region facilitates the first step in the electron trajectory where the electron is transported from the electron source to the surface of the material sample.

2.3.4 Simulating Electron Trajectories

`NISTMonte` makes the same assumptions as those mentioned in section 2.1. Only elastic scattering events determine the deflection of electrons and hence, the trajectory of the electron. Energy loss due to inelastic scattering events is continuous. `NISTMonte` makes use of Java interfaces to make the choice of algorithms very versatile. Using the scattering material model interface, any scattering model from the `EPQ` library can be used or a new one be implemented. This makes it possible to implement any variation of either the single scattering or the multiple scattering model. We used the "basic scattering model" (`BasicMaterialModel`) provided in the `EPQ` library. This model implements a simple single scattering algorithm without secondary electron generation. For the modelling of the elastic scattering events another set of algorithms must be chosen or implemented. We used the `NISTMottScatteringAngle` algorithm from the `EPQ` library which is based on [28].

An electron trajectory is initialized by the electron gun object. It then goes through a series of scattering steps until it is no longer necessary to track the electron. At the

start of every step, it is checked whether the electron requires tracking. An electron requires tracking if its energy is above a minimum threshold energy E_{min} and if its region $\mathcal{R}$ is valid, i.e $\mathcal{R}$ is either $\mathcal{V}$ or $\mathcal{B}$. Next, a new candidate point $\boldsymbol{x}_{next}$ is calculated by displacing $\boldsymbol{x}$ along its current direction by a randomly generated mean free path length s. This is depicted in figure 5.

2.3.5 Calculating the Mean Free Path

The random mean free path s tries to mimic the distance an electron would travel between two successive elastic scattering events, given its current state. If the electron is in vacuum $\mathcal{V}$ at the start of the trajectory, s is chosen as a large value so that the path intersects with the the surface of the sample. If the electron is in the sample $\mathcal{B}$, s is generated as follows.

$$s = -\lambda \log\left(R \sim \mathcal{U}(0,1)\right) \tag{12}$$

where $R \sim \mathcal{U}(0,1)$ is a uniformly distributed random number between 0 and 1. λ is the mean path length in m. It represents the average distance an electron with energy E would travel between successive elastic scattering events in the material region $\mathcal{R}$ it is currently travelling in. For a pure element sample it is calculated as follows.

$$\lambda = \frac{A}{\rho \sigma_E} \tag{13}$$

A is the atomic mass in kilograms; ρ is the mass density in kg/m^3 and σ_E is the total elastic cross section in m^2. σ_E for electron energies greater than $20keV$ is computed using the Screened Rutherford Scattering Model [27, p. 459] -

$$\sigma_E = \frac{7.670843088080456 \times 10^{-38} \cdot Z^{1/3}(1+Z)}{E + 5.44967975966321 \times 10^{-19} \cdot Z^{2/3}} \tag{14}$$

For energies less than 20 keV, σ_E is calculated using the NIST Mott electron scattering model [28] and the NIST SRD 64 database [48]. If the material is a composition of n elements of atomic numbers $Z_{I=1,2,...,n}$ with mass fractions $C_{I=1,2,...,n}$ respectively, the random mean free path length s is computed as follows -

$$\begin{aligned} \lambda_I &= \frac{A_I}{C_I \rho \sigma_E A} \qquad \forall I = 1,2,...,n \\ s_I &= -\lambda_I \log\left(R \sim \mathcal{U}(0,1)\right) \qquad \forall I = 1,2,...,n \\ s &= \min_{i=1}^{n} s_I \end{aligned} \tag{15}$$

The element that results in this least mean free path length is recorded as the scattering element, indicating that the electron has elastically collided into an atom of that element.

After the candidate-point $\boldsymbol{x}_{next}$ is calculated, a lookup algorithm is used to determine where this candidate point lies. Depending on where $\boldsymbol{x}_{next}$ lands, there can be one of two outcomes, which are as follows.

- If the candidate point $\boldsymbol{x}_{next}$ lands in the same sub-region as $\boldsymbol{x}$ the electron is simply moved to the new point and a scattering event is initiated.
- If the candidate point $\boldsymbol{x}_{next}$ is in a different sub-region or outside the material sample $\mathcal{B}$, the electron is moved to the intersection of the line connecting $\boldsymbol{x}$ to $\boldsymbol{x}_{next}$ and the boundary of the current sub-region. The electron is then given a small displacement into the next region. No scattering event is triggered.

2.3.6 Continuous Energy Loss from Inelastic Scattering

The continuous energy loss ΔE due to inelastic scattering resulting from a displacement s is computed from the stopping power $\mathrm{d}E/\mathrm{d}S$ as

$$\Delta E = \frac{\mathrm{d}E}{\mathrm{d}s} \cdot s. \tag{16}$$

Stopping power is the resistance offered to the motion of electrons in a material and is a combined effect of various inelastic scattering events and the continuous deceleration of electrons due to the Coulomb field of the electrons of the material atoms. The most well known expression for calculating the stopping power was provided by Bethe [7] as

$$\frac{\mathrm{d}E}{\mathrm{d}s} = -78500 \cdot \frac{\rho Z}{AE} \cdot \log\left(\frac{1.166E}{J}\right) \qquad [keV/cm], \tag{17}$$

where ρ is the mass density in g/cm^3, Z is the atomic number, A is the atomic weight in g, E is the energy of the electron in keV and J is the mean ionization potential in keV. Negative sign in the expression indicates loss of energy. The mean ionization potential J is the mean of the energies required for all possible inelastic scattering interactions for the electron along its path in the current step. We used the `Berger83MeanIonizationPotential` implementation available in the `EPQ` library for the computation of J. It is based on the data tabulated by Berger and Seltzer [6].

Bethe energy loss provides satisfactory values for stopping powers for high beam energies but will result in discrepancies for low beam energies [29]. Hence a modification was proposed by Joy and Luo [29] which introduces a modified mean ionization potential J^* to be used in the Bethe energy loss expression as follows:

$$\frac{\mathrm{d}E}{\mathrm{d}s} = -78500 \cdot \frac{\rho Z}{AE} \cdot \log\left(\frac{1.166E}{J^*}\right) \qquad [keV/cm], \tag{18}$$

$$J^* = \frac{J}{1 + k \cdot J/E} \qquad [keV], \tag{19}$$

$$k = 0.731 + 0.0688 \log_{10} Z.$$

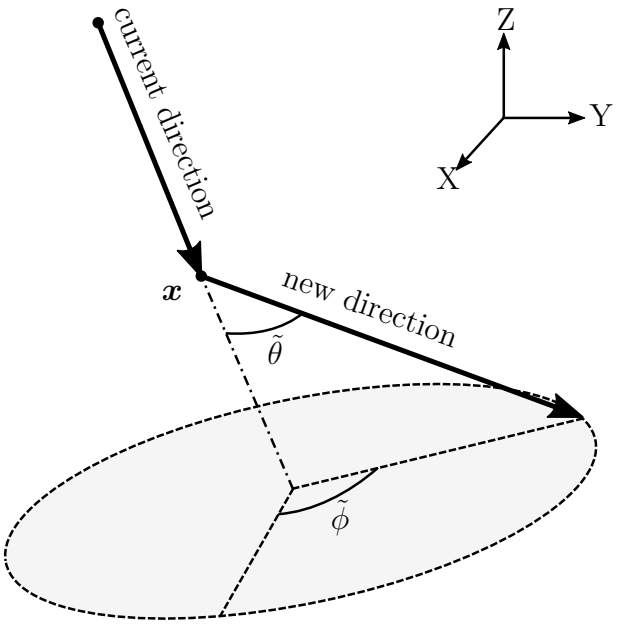

Figure 6: Monte-Carlo simulation: deflection of electron due to elastic scattering

2.3.7 Elastic Scattering

When an elastic scattering event is triggered, an elastic collision of the electron with an atom of the scattering element is simulated. In this process the direction of the electron is changed to mimic its deflection after the collision. To obtain the deflection, the co-ordinate axis is first rotated such that the Z-axis of the rotated system is aligned along the current direction of the electron. A new direction vector is determined by deflecting the current direction vector from the rotated Z-axis by a randomly generated scattering angle $\tilde{\theta} \in [0, \pi]$ followed by a deflection about the Z-axis by another random angle, resulting in a new azimuthal angle $\tilde{\phi} \in [0, 2\pi)$ in the rotated co-ordinate system. This process is illustrated as in the figure 6. The new θ and ϕ values are then obtained from the new direction vector by rotating the co-ordinate system back to the global co-ordinate system.

$\tilde{\phi} \in [0, 2\pi)$ is generally chosen as a random number from the uniform distribution $\mathcal{U}(0, 2\pi)$ and is not affected by any electron or material parameters. $\tilde{\theta} \in [0, \pi]$, on the other hand, is calculated based on elastic scattering models. For electron energies greater than 20 keV, $\tilde{\theta}$ is obtained using the screened Rutherford scattering model [40].

$$\begin{aligned} \alpha &= 5.44968 \times 10^{-19} \cdot \frac{Z^{2/3}}{E} \\ \tilde{\theta} &= \cos^{-1}\left(1 - \frac{2\alpha R}{1 + \alpha - R}\right) \end{aligned} \tag{20}$$

R is a random number between 0 and 1 generated from a uniform distribution $\mathcal{U}(0, 1)$. For energies less than 20 keV the scattering angle is computed using the NIST Mott

elastic scattering model [28]. Similar to the NIST Mott elastic cross section this method makes use of the NIST SRD 64 [48] database to generate random scattering angles.

2.3.8 Pseudocode

The pseudocode provided in algorithm 1 summarizes the Monte-Carlo method described so far.

Data: The material sample $\mathcal{B}$ with subregions $\mathcal{P}_{i=1,2,...,n}$; electron beam parameters (type, position $\boldsymbol{x}_0$, energy E_0 and direction: θ_0 and ϕ_0); no. of electrons $n_e l$; minimum energy for tracking $E_m in$
Result: Simulation of electron trajectories
for $i \leftarrow 0$ *to* n_e **do**
  generate *electron* and initialize trajectory;
  position $\boldsymbol{x} \leftarrow \boldsymbol{x}_0$;
  direction: $\theta \leftarrow \theta_0$ and $\phi \leftarrow \phi_0$;
  energy $E \leftarrow E_0$;
  region $\mathcal{R} \leftarrow \mathcal{V}$ (vacuum) ;
  `exit_material` $\leftarrow$ `false` ;
  repeat
    $s \leftarrow$ `random_mean_free_path`$(\mathcal{R}, E)$;
    $\boldsymbol{x}_{new} \leftarrow \boldsymbol{x} + s$ along current `direction`(θ, ϕ);
    $\mathcal{R}_{next} \leftarrow$ region where $\boldsymbol{x}_{new}$ lies;
    if $\mathcal{R} = \mathcal{R}_{next}$ **then**
      $\boldsymbol{x} \leftarrow \boldsymbol{x}_{new}$;
      $E \leftarrow E -$ `energy_loss`$(\mathcal{R}, E, s)$;
      $[\theta, \phi] \leftarrow$ `scatter`$([\theta, \phi], \mathcal{R}, E)$;
      if *secondary electron produced* **then**
        track secondary electron;
      end
    else
      $\boldsymbol{x}_{new} \leftarrow$ intersection point of `path`$(\boldsymbol{x}, \boldsymbol{x}_{new})$ and $\partial\mathcal{R}$ (boundary of $\mathcal{R}$);
      $\boldsymbol{x}_{new} \leftarrow \boldsymbol{x}_{new}+$ small displacement along $\boldsymbol{x}_{new} - \boldsymbol{x}$;
      $\mathcal{R}_{next} \leftarrow$ region just beyond $\partial\mathcal{R}$ along $\boldsymbol{x}_{new} - \boldsymbol{x}$;
      if $\mathcal{R} \in \mathcal{B}$ *and* $\mathcal{R}_{next} \notin \mathcal{B}$ **then**
        `exit_material` $\leftarrow$ `true`
      end
      $s \leftarrow |\boldsymbol{x}_{new} - \boldsymbol{x}|$;
      $\boldsymbol{x} \leftarrow \boldsymbol{x}_{new}$;
      $E \leftarrow E -$ `energy_loss`$(\mathcal{R}, E, s)$;
      $\mathcal{R} \leftarrow \mathcal{R}_{next}$;
    end
  until `exit_material` = `true` *or* $E < E_{min}$;
end

Algorithm 1: Pseudocode for the Monte-Carlo algorithm

3 Generated X-ray Intensity Distribution

In this section we will explore of X-ray intensity distributions and the process of extracting them from `NISTMonte`. Denoted by ϕ, the generated X-ray intensity distribution can be described in one or more dimensions and hence can have different definitions depending on the context. In general, this distribution gives us a measure of the probability of characteristic X-rays being generated in a small region within the sample when the sample is bombarded with an electron beam. The most general way of representing ϕ would be in three dimensions, for example $\phi(\rho x, \rho y, \rho z)$ in Cartesian co-ordinates. In one dimension, we can define ϕ as the depth distribution $\phi(\rho z)$, the lateral distributions $\phi(\rho x)$ and $\phi(\rho y)$, and the radial distribution $\phi(\rho r)$. Two dimensional distributions can be obtained by considering any two of these dimensions, such as $\phi(\rho x, \rho z)$ and $\phi(\rho r, \rho z)$. So far, only the depth distribution $\phi(\rho z)$ have been extensively studied and used to calculate the atomic number and absorption correction factors for matrix correction.

We can arrive at a distribution of lower dimension by integrating a distribution of higher dimension. For example,

$$\phi_{xz}(\rho x, \rho z) = \int_{-\infty}^{\infty} \phi_{xyz}(\rho x, \rho y, \rho z) \mathrm{d}\rho y, \tag{21}$$

$$\phi_{z}(\rho z) = \int_{-\infty}^{\infty} \int_{0}^{\infty} \phi_{xyz}(\rho x, \rho y, \rho z) \mathrm{d}\rho x \mathrm{d}\rho y, \tag{22}$$

$$\phi_{r}(\rho r) = \int_{0}^{\infty} \phi_{rz}(\rho r, \rho z) \mathrm{d}\rho z, \tag{23}$$

$$\phi_{z}(\rho z) = \int_{0}^{\infty} \phi_{rz}(\rho r, \rho z) \cdot 2\pi\rho r \mathrm{d}\rho r. \tag{24}$$

$\phi(\rho r, \rho z)$ is of primary interest in this work and will be described in detail in later sections.

3.1 Depth Distribution of the Generated X-ray Intensity from Experiments

As introduced in section 1.5.1, there are two main experimental techniques which can be used to obtain the depth distribution of generated X-ray intensity, namely the Tracer method and the Angular Distribution method.

The tracer method was first described and used by Castaing and Descamps [16] to obtain experimental $\phi(\rho z)$ distributions and absorption factors for Al, Cu and Au. In the tracer method two pure elements A and B are chosen such that their atomic numbers are close by on the periodic table and they are not affected by characteristic X-ray fluorescence. A thin layer of element B which acts as a tracer is sandwiched

between one polished block of element A at the bottom and one or more thin layers of element A on the top. By changing the total thickness of element A on the top, the X-ray generated from the tracer at various depths in A can be determined. $\phi(\rho z)$ can then be calculated by computing the ratio of the obtained intensities at various depths to that from a similar but unsupported layer of B. The total generated intensity $\phi_B(\rho z)\delta\rho z$ for a chosen X-ray line of element B is then given by

$$\phi(\rho z)\delta\rho z \cdot \exp(-\mu_B \rho z \csc\Psi) = (I_B)_{\rho z}/(I_B)_{free} \tag{25}$$

where $(I_B)_{\rho z}$ is the measured X-ray intensity in the sandwich setup with the tracer element layer of thickness $\delta\rho z$ being at mass depth ρz. $(I_B)_{free}$ is the measured X-ray intensity from a similar layer of element B without the top and bottom layers of element A. $\exp(-\mu_B \rho z \csc\Psi)$ is the correction for absorption, where μ_B is the mass absorption coefficient for element B in the sample and Ψ is the take of angle to the X-ray detector. The absorption correction is sometimes represented as $\exp(-\chi_B \rho z)$ where $\chi_B = \mu_B \csc\Psi$. Castaing and Descamps [16] used the experimentally obtained $\phi(\rho z)$, to determine absorption correction factors required for the ZAF procedure as follows.

$$f(\chi_B) = \frac{F(\chi_B)}{F(0)} = \frac{\int_0^\infty \phi(\rho z)\exp(-\chi_B \rho z)\mathrm{d}\rho z}{\int_0^\infty \phi(\rho z)\mathrm{d}\rho z}. \tag{26}$$

In the angular distribution technique the depth distributions are obtained by analysing the angular distribution of X-rays emitted from a bulk [26]. For a given take off angle Ψ_i, this technique yields the Laplace transform of $\phi(\rho z)$:

$$F(\chi_i) = \int_0^\infty \phi(\rho z)\exp(-\chi_i \rho z)\mathrm{d}\rho z. \tag{27}$$

Compared to the tracer method the experimental setup is much easier but a complex numerical evaluation is required to obtain $\phi(\rho z)$ from $F(\chi_i)$ [32] [26].

3.2 The Interaction Volume

When an electron beam impinges on the surface of a material sample, electrons penetrate into the sample and hence characteristic X-rays are generated from within the material. The interaction volume defines the volume of the sample where the most meaningful part of all characteristic X-rays are generated. In the context of Monte-Carlo simulations, information about the interaction volume can help us optimize the dimensions of the sample or the volume to be tracked for increased data density. For this reason, it is also convenient to express the interaction volume in terms of the maximum ranges along its linear dimensions. Since, typically, the beam is fired on to the

sample at right angles to the surface, the resulting interaction interaction volume is radially symmetric. Hence, we only need to to know two ranges: the maximum depth range of X-ray generation or depth of the interaction volume, denoted by R_x, and the maximum radial range of X-ray generation or the diameter of the interaction volume, denoted D_x.

The main factors that have been shown to affect R_x and D_x include the beam energy E_0, the relevant edge energy E_{nl} and the atomic number Z or any equivalent metric of the sample [24, pp. 68–72]. The interaction volume expands if E_0 is increased because electrons starting with more energy can travel longer distances before their energy falls below the minimum energy required to cause the emission of the characteristic X-ray line of interest. Characteristic X-rays are produced when an electron from higher energy shell jumps through a fixed energy gap to fill a vacancy in a lower energy shell nl. The edge energy E_{nl} is the energy required to knock an electron out of the nl shell to create such a vacancy. E_{nl} can be calculated from analytical models such as [62] or be obtained, for better accuracy, from databases such as [17] [19] and [9]. As E_{nl} increases the interaction volume contracts based on the same argument provided for E_0. For pure materials the interaction volume decreases with increase in atomic number Z. This is because of the increased cross sections of higher atomic number elements which results in shorter mean free paths and more scattering.

A crude method of estimating R_x and D_x would be by manipulating and integrating an expression for the stopping power $\mathrm{d}E/\mathrm{d}s$ in the interval E_{nl} to E_0. For example, from (18) which is the Bethe energy loss expression [7] modified by Joy and Luo [29], we can get

$$R_x = \int_0^{R_x} \mathrm{d}s = \int_{E_{nl}}^{E_0} \left[-78500 \cdot \frac{\rho Z}{AE} \cdot \log\left(\frac{1.166E}{J^*}\right)\right]^{-1} \mathrm{d}E \qquad [cm]. \tag{28}$$

This method actually yields the maximum trajectory length and since electrons don't travel in straight lines it is not ideal to use this measure directly as R_x [24, pp. 72–74]. Numerous other expressions have been suggested to compute R_x empirically, for example Castaing [15] provided the expression

$$R_x = \frac{33A}{\rho Z}\left(E_0^{1.7} - E_{nl}^{1.7}\right) \qquad [nm], \tag{29}$$

while Kanaya and Okayama [31] have suggested the expression

$$R_x = \frac{27.6A}{Z^{0.89}\rho} E_0^{1.67} \qquad [nm]. \tag{30}$$

In both expressions E_0 and E_{nl} are in keV, ρ is in g/cm^3, A is the mean atomic weight in g and Z is the atomic number. Similarly, few methods have been suggested in literature for approximating the diameter of the interaction volume D_x. An easy estimate would be to assume $D_x \approx R_x$ [63]. Reed [51] has recommended the use of

$D_x \approx 3R_x$ as a better estimate. A more robust expression for the relation between R_x and D_x can be found in [5], which is as follows:

$$D_x = \frac{2.2GR_x}{(1+G)} \qquad [nm], \tag{31}$$
$$G = 0.187Z^{2/3}.$$

Another way to obtain the dimensions of the interaction volume is to use Monte-Carlo Simulations. Due to the stochastic nature of the algorithm it is not a good idea to use the the maximum depth from which X-rays could be generated directly. Hence, a threshold has to be used, for example, R_x and D_x can be defined as the depth range and diameter, respectively, in which approximately 99% of all the X-rays are generated. A Monte-Carlo simulation can be run before an actual simulation to determine the range or have these data precomputed and stored in a database which can be accessed before a simulation is run.

3.3 Depth Distribution of Generated X-ray Intensity

For an X-ray line of an element A, ignoring fluorescence, $\phi(\rho z)$ is related to the total generated X-ray intensity I_A as follows.

$$I_A = C_A Q_{nl}(E_0) \int_0^\infty \phi(\rho z) \exp(-\mu_A \rho z \csc \Psi) \mathrm{d}\rho z \tag{32}$$

where C_A is the mass fraction of A, E_0 is the beam energy, μ_A is the the mass absorption coefficient of the sample for X-rays of element A, Ψ is the take off angle to the detector and $Q_{nl}(E)$ is the absolute ionization cross-section for the atomic shell nl and Energy E.

Absolute Ionization Cross-Section

Characteristic X-rays are produced when a vacancy created in an atomic shell nl is filled by an electron from an atomic shell of higher energy. The absolute ionization cross-section, also called the inelastic cross-section, is a measure of the probability with which an electron of energy E would create nl shell vacancies by knocking of the electrons in the shell per unit length of electron trjectory through the material. One of the most widely used expressions for computing ionization cross sections was provided by Casnati et al. [13]. With relativistic corrections suggested by Quarles [49] this expression is as follows [47]:

$$Q_{nl}(E) = \frac{n_{nl} a_0^2 F R^2 \psi \phi \ln U}{E_{nl}^2 U}, \tag{33}$$

$$\phi = 10.57 \exp\left(-\frac{1.736}{U} + \frac{0.317}{U^2}\right), \tag{34}$$

$$\psi = \left(\frac{E_{nl}}{R}\right)^d, \tag{35}$$

$$d = -0.0318 + \frac{0.3160}{U} - \frac{0.1135}{U^2}, \tag{36}$$

$$U = \frac{E}{E_{nl}}, \tag{37}$$

where

E_{nl} = the edge energy for nl shell,
R = the Rydberg energy unit in Joules $\approx 2.17987209 \times 10^{-18}\, J$,
n_{nl} = no. of electrons in the nl shell in the ground state of the atom,
a_0 = the Bohr radius in $m \approx 5.291772083 \times 10^{-11}\, m$.

F is the the relativistic correction calculated as

$$F = \left(\frac{2+I}{2+T}\right)\left(\frac{1+T}{1+I}\right)^2\left(\frac{(1+T)(2+T)(1+I)^2}{T(2+T)(1+I)^2 + I(2+I)}\right), \tag{38}$$

$$I = \frac{E_{nl}}{m_e c^2}, \tag{39}$$

$$T = \frac{E}{m_e c^2}, \tag{40}$$

where

m_e = electron rest mass,
c = speed of light in vacuum.

This expression is sufficient for computing K-shell ionization cross sections, but L and M shells are not characterized well. Another model that is at least as good as the model described so far for the K-shell and with a better fit for L and M shells can be found in [9] [10].

3.3.1 Obtaining the Distribution from Electron Density Distribution

In order to calculate $\phi(\rho z)$ from simulated electron trajectories, we shall make use of another quantity called the electron energy density distribution $N(E, \rho z)$. It is a distribution of the average of length of electron trajectories with energy E in a layer of infinitesimal thickness $\delta\rho z$ at a mass depth ρz. It is computed as the sum total of lengths of electron trajectories passing through the region with energies in the range $E \pm \delta E/2$ divided by the total number of electron trajectories simulated, where δE is an infinitesimal change in energy. The intensity of characteristic X-rays of an element A generated in a thin layer of thickness $\delta\rho z$ at mass depth ρz in the sample can then be calculated as

$$I_A = C_A \int_{E_{nl}}^{E_0} Q_{nl}(E) N(E, \rho z) \mathrm{d}E \tag{41}$$

where C_A is the mass fraction of A in the layer considered. Now, consider a similar experimental setup but where the sample is swapped for just this thin layer. If we assume that the electron beam is always incident along the normal to top surface of the sample, for small values of $\delta\rho z$, the average length of electron trajectories passing through the unsupported thin layer is equal to $\delta\rho z$ and the energy is nearly uniform and equal to E_0. The intensity of X-rays generated from such a thin unsupported layer would then given by

$$(I_A)_{free} = C_A Q_{nl}(E_0)\delta\rho z. \tag{42}$$

$\phi(\rho z)$ according to Castaing's definition is then given by the ratio

$$\phi(\rho z) = \frac{I_A}{(I_A)_{free}} = \frac{1}{Q_{nl}(E_0)} \int_{E_{nl}}^{E_0} \frac{Q_{nl}(E)N(E,\rho z)}{\delta\rho z} \mathrm{d}E. \tag{43}$$

This also gives us an alternate way to define $\phi(\rho z)$ and ϕ in general, i.e as the ratio of generated X-ray intensity per unit mass length at a depth ρz to the inelastic cross-section corresponding to the beam energy E_0.

3.3.2 Obtaining the Distribution from Monte Carlo Simulations

One of the ways to obtain $\phi(\rho z)$ numerically is by discretizing ρz and E and computing a histogram of $\phi(\rho z)$ from trajectories simulated using a Monte-Carlo algorithm. We start with the discretization of the sample along mass depth, in the range 0 to R_x, into a set of $N_z + 1$ nodes

$$\hat{\mathcal{G}}_{\rho z} := \left\{\hat{\rho z}_0, \hat{\rho z}_1, \ldots, \hat{\rho z}_{N_z} \mid \hat{\rho z}_0 = 0,\ \hat{\rho z}_{N_z} = R_x,\ \hat{\rho z}_i > \hat{\rho z}_{i-1}\ \forall i = 1, 2, \ldots, N_z\right\} \tag{44}$$

This is illustrated in figure 7. Without loss of generality, $\hat{\rho z}_i$ can be denoted as positive, despite moving along the negative Z axis as shown in figure 7. Conventionally, ρz has always been denoted with positive values when discussing $\phi(\rho z)$ in literature. Hence, we chose to do the same for the sake of convenience and consistency. The intervals bounded by successive nodes will function as bins to accumulate $\phi(\rho z)$ as a histogram. We can now define the mean positions of the N_z bins along ρz as

$$\mathcal{G}_{\rho z} := \left\{\rho z_i = \frac{\hat{\rho z}_{i-1} + \hat{\rho z}_i}{2};\ i = 1, 2, \ldots, N_z\right\}. \tag{45}$$

The bin sizes corresponding to these bins are then.

$$\Delta\mathcal{G}_{\rho z} := \left\{\Delta\rho z_i = \hat{\rho z}_i - \hat{\rho z}_{i-1};\ i = 1, 2, \ldots, N_z\right\}. \tag{46}$$

Essentially, the sample is subdivided into horizontal layers. These layers are not modelled as subregions in the sample and are stored in a separate data structure. Making sub regions was avoided when possible because adding sub-regions increases the number of individual steps in a trajectory and therefore penalises performance . We can

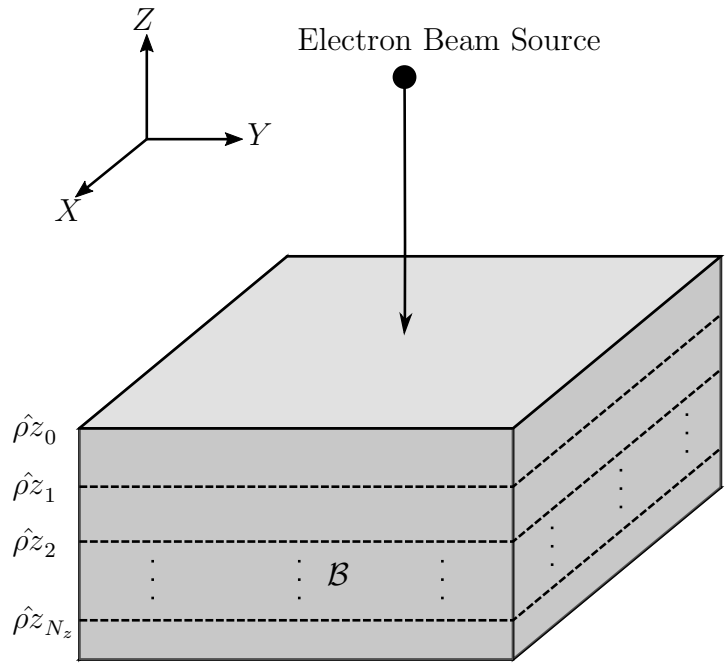

Figure 7: Discretization of the mass depth ρz

apply the same treatment to electron energy and obtain the discretization of energy into N_E bins in the range $[E_{nl}, E_0]$ as

$$\begin{aligned}
\hat{\mathcal{G}}_E &:= \left\{ \hat{E}_0, \hat{E}_1, \ldots, \hat{E}_{N_E} \mid \hat{E}_0 = E_{nl},\ \hat{E}_{N_E} = E_0,\ \hat{E}_i > \hat{E}_{i-1}\, \forall i = 1, 2, \ldots, N_E \right\}, \\
\mathcal{G}_E &:= \left\{ E_i = \frac{\hat{E}_i - \hat{E}_{i-1}}{2};\ i = 1, 2, \ldots, N_E \right\}, \\
\Delta\mathcal{G}_E &:= \left\{ \Delta E_i = \hat{E}_i - \hat{E}_{i-1};\ i = 1, 2, \ldots, N_E \right\}.
\end{aligned} \tag{47}$$

We can then obtain the quantity $N(E, \rho z)\mathrm{d}E$ from equation (43) in the discrete form, as a two dimensional matrix, from a Monte-Carlo simulation. The matrix dimensions are determined by the number of material bins N_Z and energy bins N_E. N_Z and N_E are the number of rows and number of columns of the N matrix respectively. The matrix

$$N = \begin{bmatrix} N_{11} & N_{12} & \cdots & N_{1N_E} \\ N_{21} & N_{22} & \cdots & N_{2N_E} \\ \vdots & \vdots & \ddots & \vdots \\ N_{N_z1} & N_{N_z2} & \cdots & N_{N_zN_E} \end{bmatrix} \in \mathbb{R}^{N_z \times N_E} \tag{48}$$

is defined such that

$$N_{ij} = \frac{\sum \begin{pmatrix} \text{electron path segments with energies between } \hat{E}_{j-1} \text{ and } \hat{E}_j \\ \text{at depths between } \hat{\rho z}_{i-1} \text{ and } \hat{\rho z}_i \end{pmatrix}}{\text{total no. of electrons}}. \tag{49}$$

The depth distribution in discrete form $[\phi(\rho z_i)] \in \mathbb{R}_z^N$, i.e. as a histogram, can then be found from the discrete form of equation (43), by substituting E, ρz and $N(E, \rho z)\mathrm{d}E$ for their discrete counterparts, as

$$\phi(\rho z_i) = \frac{1}{Q_{nl}(E_0)} \sum_{j=1}^{N_e} \frac{Q(E_j) N_{ij}}{\Delta \rho z_i}. \tag{50}$$

3.3.3 Pseudocode

`NISTMonte` makes use of `Java`'s built in event handling mechanism to announce to the rest of the program when specific scattering and non-scattering events during electron trajectories take place. Event listeners can be defined before the program is run, and any action event triggered during the execution of the program will be broadcast to all the available event listeners. Since the code uses object oriented programming, all simulation parameters are stored as objects which can be accessed by the event listeners to perform additional tasks when an event is fired. Three types of events are listened to for computing $\phi(\rho z)$. They are the events signalling elastic scattering, barrier transport (movement of electrons across sub-regions) and the end of electron trajectory (due to loss of energy beyond the cut-off energy or the escape of the electron from the material). `NISTMonte`, conveniently, also stores the previous state of the electron in the electron object along with its current state. Details about the parameters that define an electron's state can be found in section 2.3.3. The current and previous states of the electron being tracked can thus be extracted from the simulation and the path traversed by the electron after the previous event until current simulation time can then be determined. This path is then subdivided into smaller paths that fit within individual ρz and E bins. The mass lengths of these mini-paths can then be accumulated in corresponding positions in N matrix as shown in equation (50). A pseudocode for the procedure is provided in algorithm 2.

3.3.4 Examples

Some plots of $\phi(\rho z)$ obtained using `NISTMonte` Monte-Carlo simulations can be found in figure 8. The figures confirm that $\phi(\rho z = 0) \geq 1$. The distribution appears skewed to the right. This is a result of the back-scattered electrons leaving the sample at $\rho z = 0$.

Data: A Monte-Carlo simulation `MCSim`; ρz bins ($\hat{\mathcal{G}}_{\rho z}$, $\mathcal{G}_{\rho z}$, $\Delta\mathcal{G}_{\rho z}$ and N_z); E bins ($\hat{\mathcal{G}}_E$, $\mathcal{G}_E$, $\Delta\mathcal{G}_E$, and N_E); Beam energy E_0.
Result: $[\phi(\rho z_i)] \in \mathbb{R}^{N_z}$
initialize;
$N \leftarrow [0]^{N_z \times N_E}$;
$\phi \leftarrow [0]^{N_z}$;
start `MCSim`
  when *any event* $\in$ {*`scatter`, `barrier transport`, `trajectory end`*} *fired* **do**
    `electron` $\leftarrow$ `current_electron(MCSim)`;
    $\boldsymbol{x}_s \leftarrow$ `previous_position(electron)`;
    $\boldsymbol{x}_e \leftarrow$ `position(electron)`;
    $\rho z_s \leftarrow$ `mass_depth`($\boldsymbol{x}_{prev}$, `electron`);
    $\rho z_e \leftarrow$ `mass_depth`($\boldsymbol{x}$, `electron`);
    $P \leftarrow$ `path`($\boldsymbol{x}_{prev}$, $\boldsymbol{x}$, `electron`);
    $\{p_i\ ;\ i \in i_s\ to\ i_e\} \leftarrow$ `segment_path`(P, ρz_s, ρz_e, $\hat{\mathcal{G}}_{\rho z}$);
    for $i \leftarrow i_s\ to\ i_e$ **do**
      $E_s \leftarrow$ `start_energy`(p_i, `electron`);
      $E_e \leftarrow$ `end_energy`(p_i, `electron`);
      $\{q_j\ ;\ j \in j_s\ to\ j_e\} \leftarrow$ `segment_path`(p_i, E_s, E_e, $\hat{\mathcal{G}}_E$);
      for $j \leftarrow j_s\ to\ j_e$ **do**
        $\rho s \leftarrow$ `path_length`(q_j);
        $N_{ij} \leftarrow N_{ij} + \rho s$;
      end
    end
  end
end
for $i \leftarrow 1\ to\ N_z$ **do**
  `sum` $\leftarrow 0$;
  for $j \leftarrow 1\ to\ N_E$ **do**
    `sum` $\leftarrow$ `sum` $+Q_{nl}(E_j)N_{ij}$;
  end
  $\phi_i \leftarrow \dfrac{\texttt{sum}}{Q_{nl}E_0\Delta\rho z_i}$;
end

Algorithm 2: Pseudocode for obtaining $\phi(\rho z)$ from a Monte-Carlo simulation

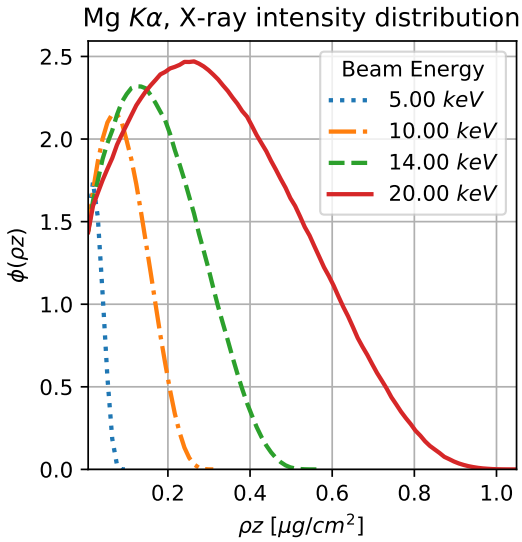

(a) Mg $K\alpha$ line in Mg

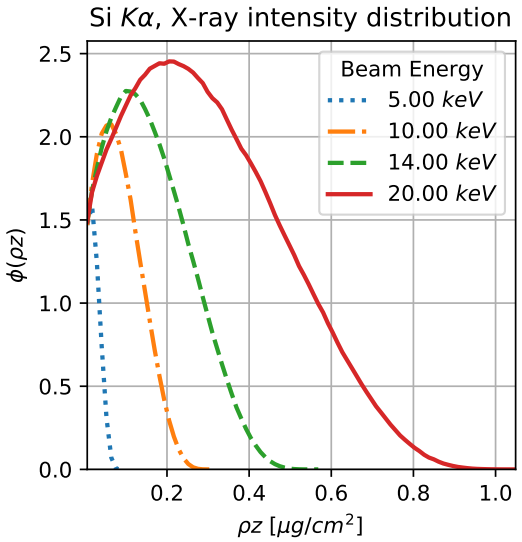

(b) Si $K\alpha$ line in Si

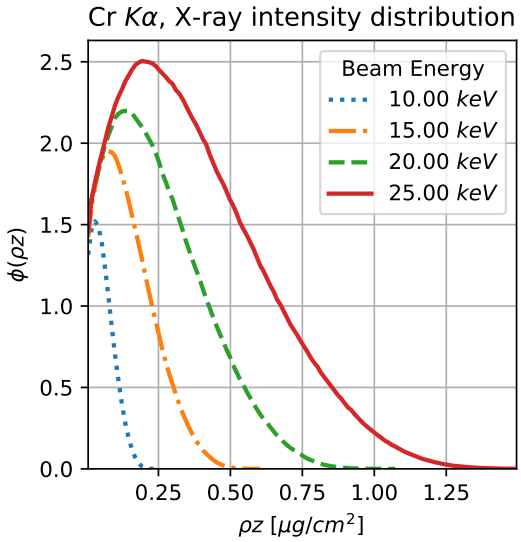

(c) Cr $K\alpha$ line in Cr

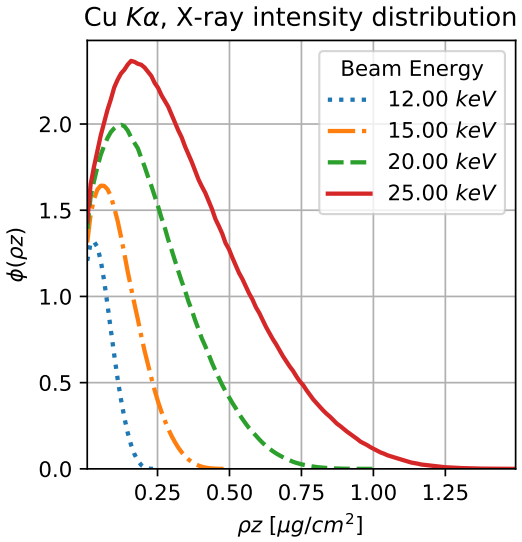

(d) Cu $K\alpha$ line in Cu

Figure 8: Some examples of generated X-ray intensity distributions in pure eleement materials obtained from Monte-Carlo simulations

3.4 Lateral Distribution of Generated X-ray Intensity

The lateral distribution of the generated X-ray intensity describes the distribution along the X or the Y axis for an experimental setup such as in figure 4. The distribution is denoted as $\phi(\rho x)$ or $\phi(\rho y)$ respectively. For flat-topped homogeneous samples bombarded by electron beams perpendicular to the top surface, the interaction volume has radial symmetry. In such cases, we can assume $\phi(\rho x) = \phi(\rho y)$. Since we are focusing on similar conditions, we will only focus of $\phi(\rho x)$.

Analogous to $\phi(\rho z)$, $\phi(\rho x)$ describes the amount of X-rays generated in a vertical layer of small thickness $\delta\rho z$, parallel to the YZ plane and at a distance ρx from the origin. But Castaing's [14] definition for $\phi(\rho z)$ cannot directly be applied here. It is because if we isolate a thin vertical layer of the sample at distance ρx, electrons from the electron beam won't be able to reach it without a scattering medium. Hence $\phi(\rho x)$ is best defined using an expression similar to equation (32), i.e. $\phi(\rho x)$ is that quantity which is related to the generated X-ray intensity at a distance ρx as

$$I_A = C_A Q_{nl}(E_0) \int_{-\infty}^{\infty} \phi(\rho x) \exp\left[-\mu_A g(\rho x)\right] \mathrm{d}\rho x, \tag{51}$$

where I_A, C_A, E_0, μ_A and $Q_{nl}(E)$ have the same definitions as in equation (32). The new quantity $g(\rho x)$ is a measure of the average distance an X-ray generated in vertical layer at ρx must travel through the material on its way to the detector assuming a straight line of travel. $\phi(\rho x)$, in the continuous form, can be obtained from an expression similar to equation (43), i.e.

$$\phi(\rho x) = \frac{1}{Q_{nl}(E_0)} \int_{E_{nl}}^{E_0} \frac{Q_{nl}(E) N(E, \rho x)}{\delta\rho x} \mathrm{d}E. \tag{52}$$

3.4.1 Obtaining the Distribution from Monte Carlo Simulations

Similar to the method used for obtaining the depth distribution of generated X-rays, as described in section 3.3.2, we start with the discretization the material and energy into bins. For the material, we define

$$\begin{aligned}
\hat{\mathcal{G}}_{\rho x} &:= \left\{ \hat{\rho x}_0, \hat{\rho x}_1, \ldots, \hat{\rho x}_{N_x} \mid \hat{\rho x}_0 = -\frac{D_x}{2},\ \hat{\rho x}_{N_x} = \frac{D_x}{2},\ \hat{\rho x}_i > \hat{\rho x}_{i-1}\ \forall i = 1, 2, \ldots, N_x \right\}, \\
\mathcal{G}_{\rho x} &:= \left\{ \rho x_i = -\frac{\hat{\rho x}_{i-1} + \hat{\rho x}_i}{2};\ i = 1, 2, \ldots, N_x \right\} \text{ and} \\
\Delta\mathcal{G}_{\rho x} &:= \left\{ \Delta\rho x_i = \hat{\rho x}_i - \hat{\rho x}_{i-1};\ i = 1, 2, \ldots, N_x \right\}.
\end{aligned} \tag{53}$$

This is illustrated in figure 9. The discretization of energy is identical to equation (47).

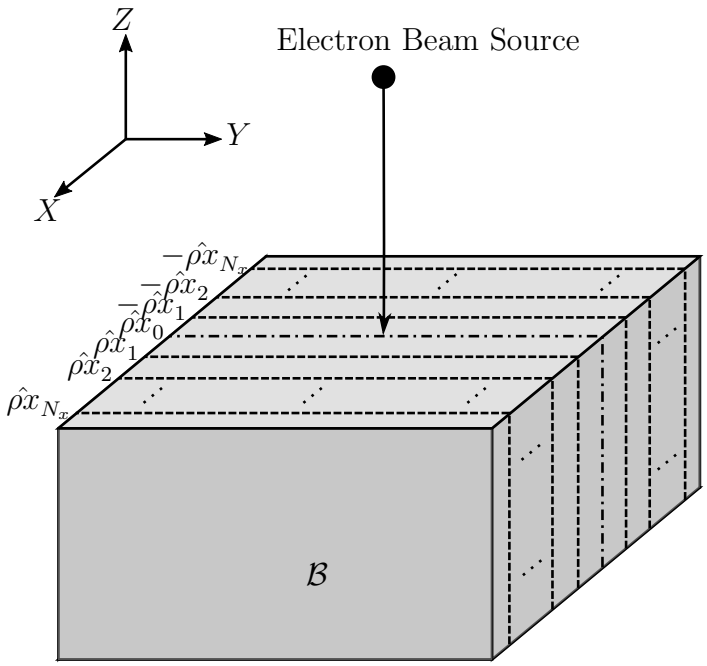

Figure 9: Discretization of the lateral distance ρx

The electron density matrix $N \in \mathbb{R}^{N_x \times N_E}$ can then be accumulated by running a Monte-Carlo Simulation, i.e. as

$$N_{ij} = \frac{\sum \begin{pmatrix} \text{electron path segments with energies between } \hat{E}_{j-1} \text{ and } \hat{E}_j \\ \text{at lateral distances between } \hat{\rho x}_{i-1} \text{ and } \hat{\rho x}_i \end{pmatrix}}{\text{total no. of electrons}}. \tag{54}$$

$\phi(\rho x)$, in the discrete form $[\phi(\rho x)] \in \mathbb{R}^N_x$, is now obtained using

$$\phi(\rho x_i) = \frac{1}{Q_{nl}(E_0)} \sum_{j=1}^{N_e} \frac{Q(E_j) N_{ij}}{\Delta \rho x_i}. \tag{55}$$

The pseudo-code is identical to the one in algorithm 2 after defining $\hat{\mathcal{G}}$, $\mathcal{G}$ and $\Delta\mathcal{G}$, the only difference being that the electron paths are subdivided along ρx instead of ρz.

3.4.2 Examples

Figure 10 shows examples of $\phi(\rho x)$ obtained from Monte-Carlo simulations for pure elemental materials. Symmetry about the origin resulting from the radial symmetry of the interaction volume is evident here. The distribution has a sharp peak at $\rho x = 0$ and has an exponential or Gaussian like tail. It also shows that the diameter of the

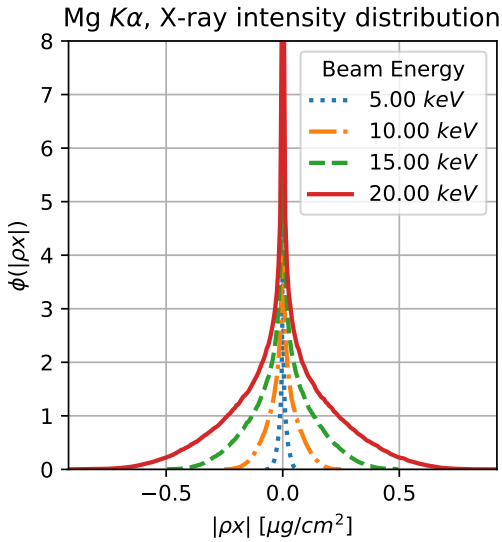

(a) Mg $K\alpha$ line in Mg

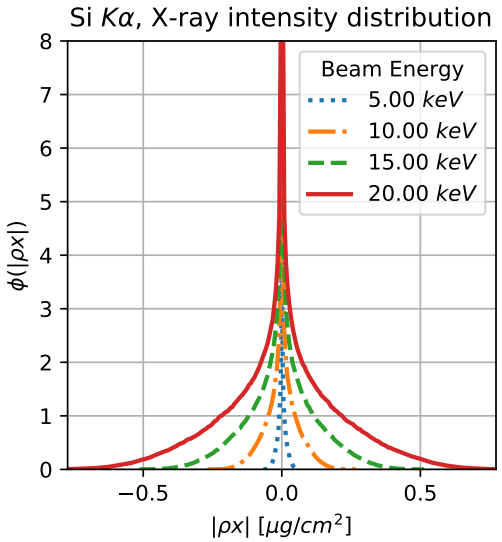

(b) Si $K\alpha$ line in Si

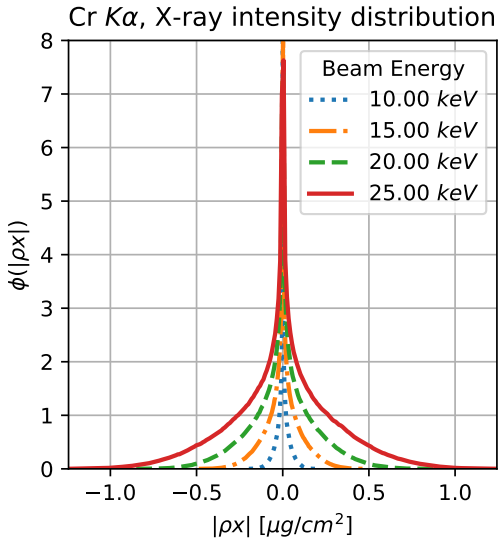

(c) Cr $K\alpha$ line in Cr

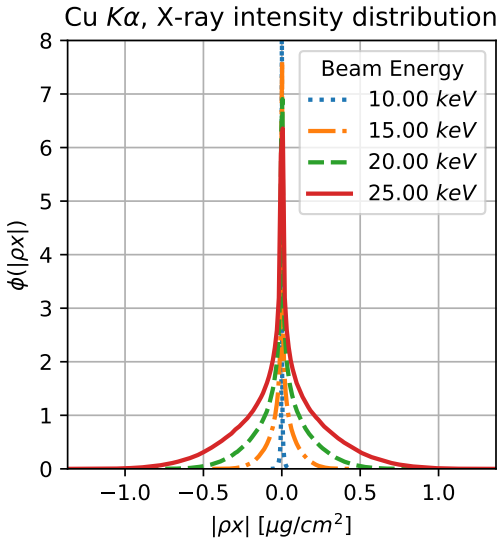

(d) Cu $K\alpha$ line in Cu

Figure 10: Generated X-ray intensity distributions in pure elemental materials obtained from Monte-Carlo simulations

interaction volume can be significantly reduced by using a lower energy beam. This principle can be used to increase spatial resolution in electron probe microanalysis with low energy electron beams [5].

3.5 Radial distribution of Generated X-ray Intensity

The radial distribution $\phi(\rho r)$ is a measure of the amount of X-rays generated in a hollow cylinder with radius ρr and thickness $\delta\rho r$ that runs through the material from its top surface to the bottom. Extending equation (32) for the case of radial distribution, we get

$$I_A = C_A Q_{nl}(E_0) \int_0^\infty \phi(\rho r) \exp\left[-\mu_A g(\rho r)\right] 2\pi\rho r \mathrm{d}\rho r. \tag{56}$$

All terms have the same meaning as in equations (32) and (51). Here the integration is carried out with $2\pi\rho r dr$, which happens to be the cross-sectional area of the cylindrical layer of radius r and small thickness dr. Because of the addition the ρr term in the integrand, $\phi(\rho r)$ also has different units compared to $\phi(\rho x)$ and $\phi(\rho z)$. In fact it has the same units as a traditional two-dimensional distribution such as $\phi(\rho x, \rho z)$ and $\phi(\rho x, \rho y)$. Under radial symmetry, $\phi(\rho z)$ can completely describe the two dimensional distribution $\phi(\rho x, \rho y)$ as

$$\phi_{xy}(\rho x, \rho y) = \phi_r\left(\rho r = \sqrt{(\rho x)^2 + (\rho y)^2}\right) \tag{57}$$

The equation for $\phi(\rho r)$ in terms of the corresponding electron energy density distribution $N(E, \rho r)$ is then given by

$$\phi(\rho r) = \frac{1}{Q_{nl}(E_0)} \int_{E_{nl}}^{E_0} \frac{Q_{nl}(E) N(E, \rho r)}{2\pi\rho r \delta\rho r} \mathrm{d}E. \tag{58}$$

3.5.1 Obtaining the Distribution from Monte Carlo Simulations

Similar to the previous cases we start with the discretization of the material and energy into bins. For the material, we define

$$\begin{aligned}
\hat{\mathcal{G}}_{\rho r} &:= \left\{ \hat{\rho r}_0, \hat{\rho r}_1, \ldots, \hat{\rho r}_{N_r} \mid \hat{\rho r}_0 = 0,\ \hat{\rho r}_{N_r} = \frac{D_x}{2},\ \hat{\rho r}_i > \hat{\rho r}_{i-1}\ \forall i = 1, 2, \ldots, N_r \right\}, \\
\mathcal{G}_{\rho r} &:= \left\{ \rho r_i = -\frac{\hat{\rho r}_{i-1} + \hat{\rho r}_i}{2};\ i = 1, 2, \ldots, N_r \right\} \text{ and} \\
\Delta\mathcal{G}_{\rho r} &:= \left\{ \Delta\rho r_i = \hat{\rho r}_i - \hat{\rho r}_{i-1};\ i = 1, 2, \ldots, N_r \right\}
\end{aligned} \tag{59}$$

as illustrated in figure 9. The discretization of energy remains the same as in equation (47).

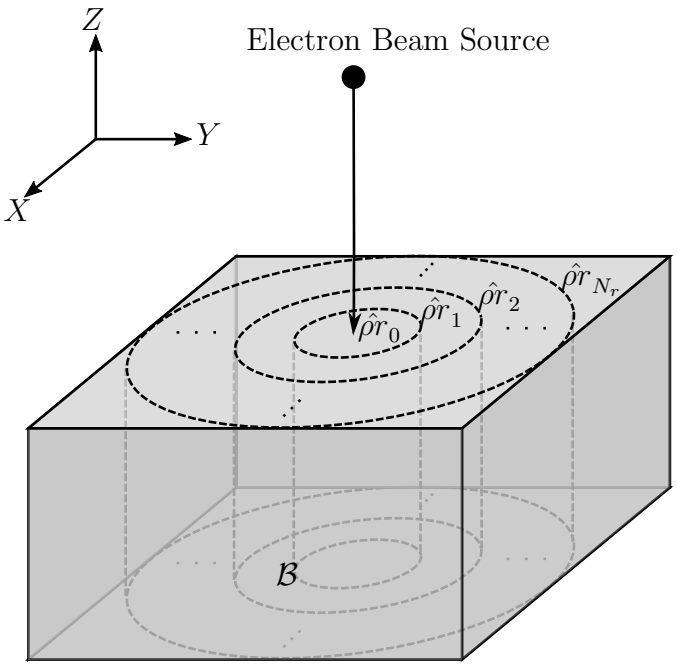

Figure 11: Discretization of the radial distance ρr

The electron density matrix $N = [N_{ij}] \in \mathbb{R}^{N_R \times N_E}$ is obtained using

$$N_{ij} = \frac{\sum \begin{pmatrix} \text{electron path segments with energies between } \hat{E}_{j-1} \text{ and } \hat{E}_j \\ \text{at radial distances between } \hat{\rho r}_{i-1} \text{ and } \hat{\rho r}_i \end{pmatrix}}{\text{total no. of electrons}}. \tag{60}$$

The histogram of $\phi(\rho r)$, $[\phi(\rho r_i)] \in \mathbb{R}^{N_r}$, is then obtained from

$$\phi(\rho r_i) = \frac{1}{Q_{nl}(E_0)} \sum_{j=1}^{N_e} \frac{Q(E_j) N_{ij}}{2\pi \rho r_i \Delta \rho r_i}. \tag{61}$$

The pseudo-code is the same as algorithm 2, but when subdividing electron paths along ρr care must be taken to account for paths that may cut across one or more inner bins before ending up in an outer bin, for example, as shown in figure 12.

3.6 Examples

Figure 13 contains examples of $\phi(\rho r)$ obtained from `NISTMonte` Monte-Carlo simulations. We can see a similar peak at $\rho r = 0$ as seen at $\rho x = 0$ in the previous case. But, here the peak is more pronounced.

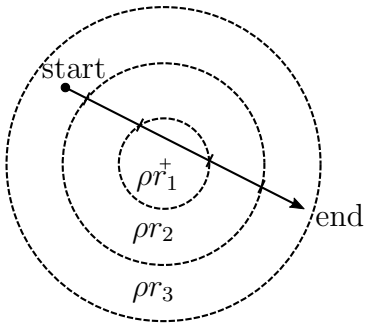

Figure 12: Electron trajectories can cut across ρr bins

3.7 Two Dimensional Distribution of Generated X-Ray Intensity along Radial and Vertical Directions

The two dimensional distribution $\phi(\rho r, \rho z)$ is a measure of the intensity of locally generated X-rays in the radial and vertical directions. While ignoring effects of fluorescence, It is related to the total emitted X-ray intensity through the integral

$$I_A = C_A Q_{nl}(E_0) \int_0^\infty \int_0^\infty \phi(\rho r, \rho z) \exp\left[-\mu_A g(\rho r, \rho z)\right] 2\pi \rho r \mathrm{d}\rho r \mathrm{d}\rho z, \tag{62}$$

where I_A, C_A, $Q_{nl}(E)$, μ_A have the same meaning as in equation (32).

$\phi(\rho r, \rho z)$ can be determined from the two dimensional electron density distribution $N(E, \rho r, \rho z)$ as

$$\phi(\rho z) = \frac{1}{Q_{nl}(E_0)} \int_{E_{nl}}^{E_0} \frac{Q_{nl}(E) N(E, \rho r, \rho z)}{2\pi \rho r \delta \rho r \delta \rho z} \mathrm{d}E. \tag{63}$$

where E_0 is the electron beam energy. When there is radial symmetry, $\phi(\rho r, \rho z)$ describes the complete three dimensional distribution, i.e. under radial symmetry,

$$\phi_{xyz}(\rho x, \rho y, \rho z) = \phi_{rz}\left(\rho r = \sqrt{(\rho x)^2 + (\rho y)^2}, \rho z\right). \tag{64}$$

3.7.1 Obtaining the Distribution from Monte Carlo Simulations

As discussed in the earlier sections we start by discretizing the material, now, both along ρr and ρz as $\{\hat{\mathcal{G}}_{\rho r}, \mathcal{G}_{\rho r}, \Delta\mathcal{G}_{\rho r}\}$ and $\{\hat{\mathcal{G}}_{\rho z}, \mathcal{G}_{\rho z}, \Delta\mathcal{G}_{\rho z}\}$ respectively, and then the energy as $\{\hat{\mathcal{G}}_E, \mathcal{G}_E, \Delta\mathcal{G}_E\}$ (see sections 3.3.2 and 3.5.1). Figure 14a illustrates the discretization of the material and figure 14b shows an individual at a radial distance ρr_i and depth ρz_j. Note that the volume of such an element is given by $2\pi \rho r_i \Delta\rho r_i \Delta\rho z_j$.

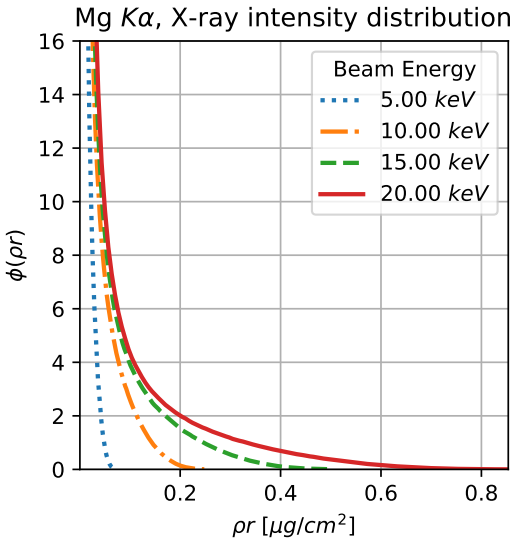

(a) Mg $K\alpha$ line in Mg

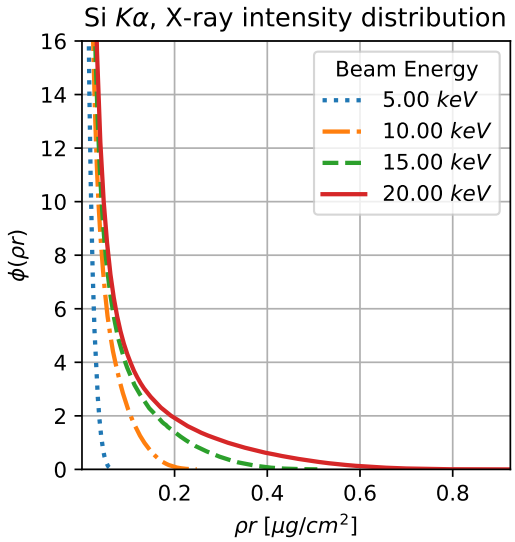

(b) Si $K\alpha$ line in Si

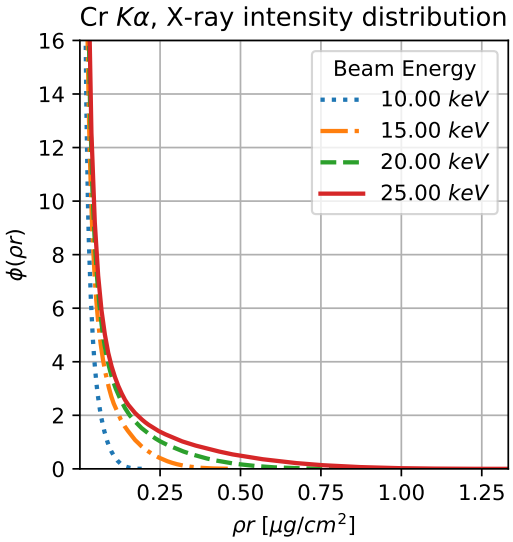

(c) Cr $K\alpha$ line in Cr

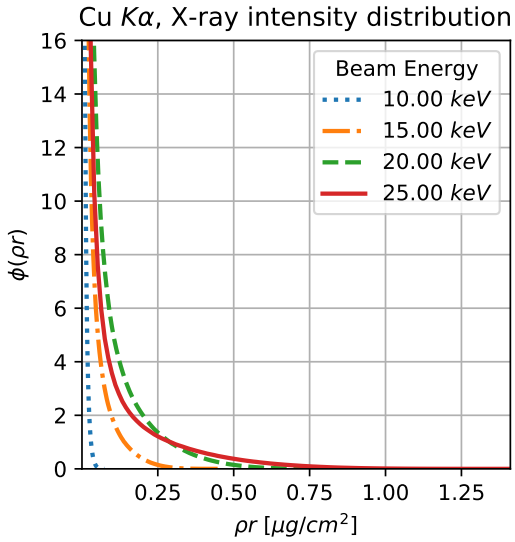

(d) Cu $K\alpha$ line in Cu

Figure 13: Generated X-ray intensity distributions in pure elemental materials obtained from Monte-Carlo simulations

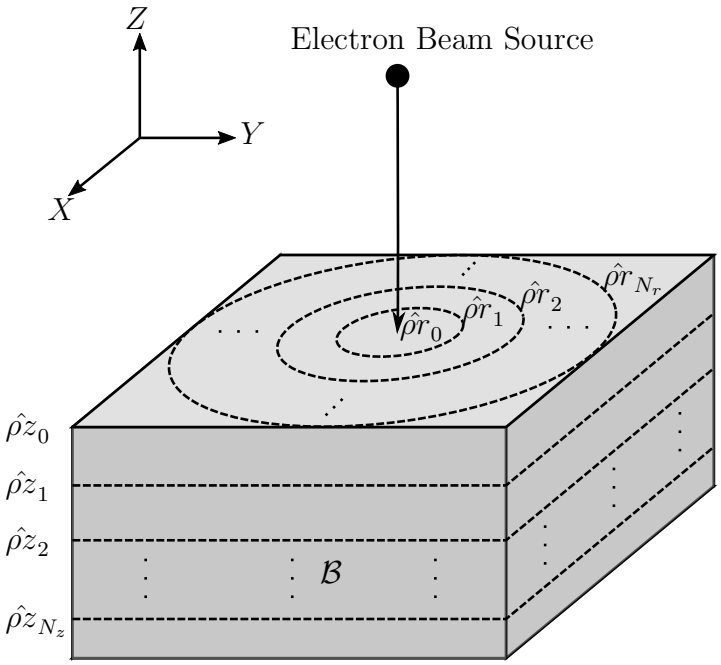

(a) Discretization of the radial and vertical distances - ρr and ρz respectively.

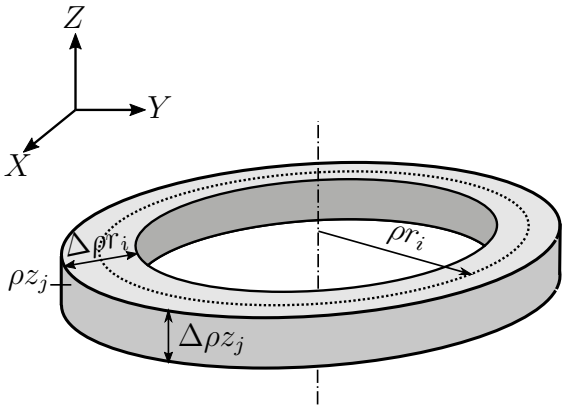

(b) An individual bin at depth ρz and radial distance ρr.

Figure 14: Discretization of the material.

Now, if we have the discrete form of the electron density distribution given by $N = [N_{ijk}] \in \mathbb{R}^{N_R \times N_r \times N_z}$ such that

$$N_{ij} = \frac{\sum \begin{pmatrix} \text{electron path segments with energies between } \hat{E}_{k-1} \text{ and } \hat{E}_k \\ \text{at radial distances between } \hat{\rho r}_{i-1} \text{ and } \hat{\rho r}_i \\ \text{and at depths between } \hat{\rho z}_{j-1} \text{ and } \hat{\rho z}_j \end{pmatrix}}{\text{total no. of electrons}}, \tag{65}$$

we can obtain $[\phi_{ij}] = [\phi(\rho r_i, \rho z_j)] \in \mathbb{R}^{N_r \times N_z}$ from

$$\phi(\rho r_i) = \frac{1}{Q_{nl}(E_0)} \sum_{k=1}^{N_e} \frac{Q(E_j) N_{ijk}}{2\pi \rho r_i \Delta \rho r_i \Delta \rho z_i}. \tag{66}$$

3.7.2 Pseudocode

The algorithm is similar to algorithm 2 but will require three levels of segmentation for the electron paths - once along ρr, then along ρz and finally for energy E. This is codified in algorithm 3.

3.7.3 Examples

Figure 15 and figure 16 show some examples of $\phi(\rho r, \rho z)$. The peak found in $\phi(\rho r)$ at $\rho r \sim 0$ is also found here. Here it is concentrated more at $\rho r = 0$ and $\rho z = 0$. The high value of the peak completely obscures the rest of the plot.

Data: A Monte-Carlo simulation `MCSim`; ρz bins ($\hat{\mathcal{G}}_{\rho z}$, $\mathcal{G}_{\rho z}$, $\Delta\mathcal{G}_{\rho z}$ and N_z); E bins ($\hat{\mathcal{G}}_E$, $\mathcal{G}_E$, $\Delta\mathcal{G}_E$, and N_E); Beam energy E_0.
Result: $[\phi(\rho z_i)] \in \mathbb{R}^{N_z}$
initialize;
$N \leftarrow [0]^{N_z \times N_E}$;
$\phi \leftarrow [0]^{N_z}$;
start `MCSim`
  when *any event* $\in$ {*`scatter`, `barrier_transport`, `trajectory_end`*} *fired* **do**
    `electron` $\leftarrow$ `current_electron(MCSim)`;
    $\boldsymbol{x}_s \leftarrow$ `previous_position(electron)`;
    $\boldsymbol{x}_e \leftarrow$ `position(electron)`;
    $\rho r_s \leftarrow$ `radial_distance(`$\boldsymbol{x}_{prev}$`, electron)`;
    $\rho r_e \leftarrow$ `radial_distance(`$\boldsymbol{x}$`, electron)`;
    $P \leftarrow$ `path(`$\boldsymbol{x}_{prev}$`,` $\boldsymbol{x}$`, electron)`;
    $\{p_i\ ;\ i \in i_s\ to\ i_e\} \leftarrow$ `segment_path(`P`,` ρr_s`,` ρr_e`,` $\hat{\mathcal{G}}_{\rho r}$`)`;
    for $i \leftarrow i_s\ to\ i_e$ **do**
      $\rho z_s \leftarrow$ `mass_depth(start_point(`p_i`))`;
      $\rho z_e \leftarrow$ `mass_depth(end_point(`p_i`))`;
      $\{q_j\ ;\ k \in j_s\ to\ j_e\} \leftarrow$ `segment_path(`p_i`,` ρz_s`,` ρz_e`,` $\hat{\mathcal{G}}_{\rho z}$`)`;
      for $j \leftarrow j_s\ to\ j_e$ **do**
        $E_s \leftarrow$ `start_energy(`q_j`, electron)`;
        $E_e \leftarrow$ `end_energy(`q_j`, electron)`;
        $\{r_k\ ;\ k \in k_s\ to\ k_e\} \leftarrow$ `segment_path(`q_j`,` E_s`,` E_e`,` $\hat{\mathcal{G}}_E$`)`;
        for $k \leftarrow k_s\ to\ k_e$ **do**
          $\rho s \leftarrow$ `path_length(`r_k`)`;
          $N_{ijk} \leftarrow N_{ijk} + \rho s$;
        end
      end
    end
  end
end
for $i \leftarrow 1\ to\ N_r$ **do**
  for $j \leftarrow 1\ to\ N_z$ **do**
    `sum` $\leftarrow 0$;
    for $k \leftarrow 1\ to\ N_E$ **do**
      `sum` $\leftarrow$ `sum` $+Q_{nl}(E_k)N_{ijk}$;
    end
    $\phi_{ij} \leftarrow \dfrac{\texttt{sum}}{Q_{nl}(E_0) \cdot 2\pi\rho r_i \Delta\rho r_i \Delta\rho z_j}$;
  end
end

Algorithm 3: Pseudocode for obtaining $\phi(\rho r, \rho z)$ from a Monte-Carlo simulation

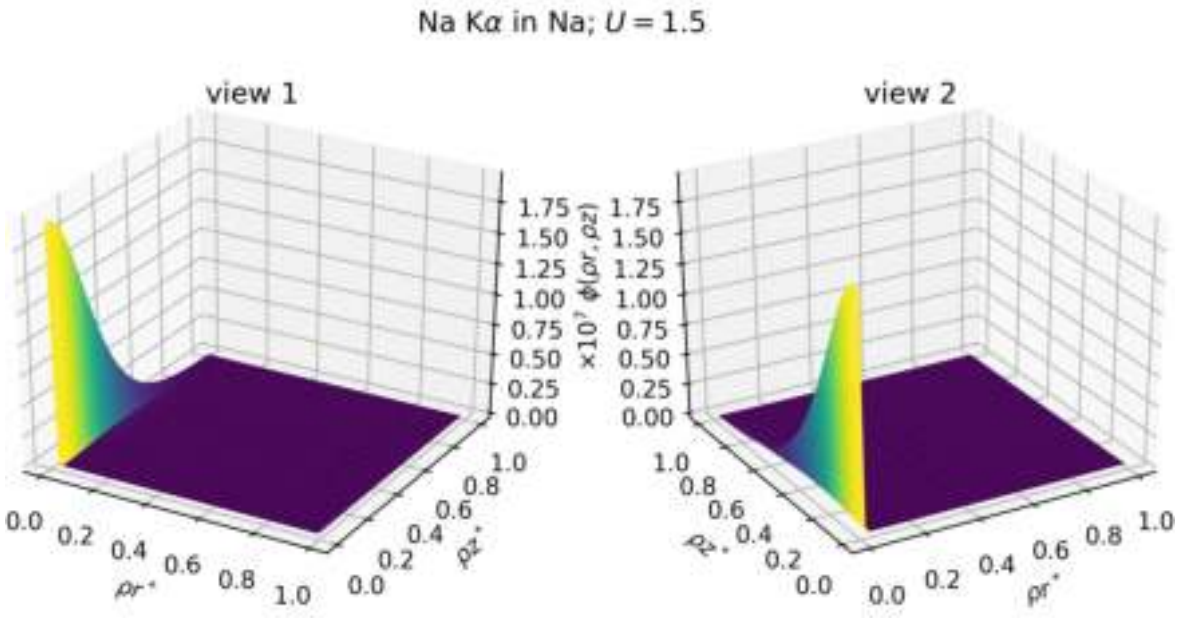

(a) Na $K\alpha$ line in Na; U = 1.5

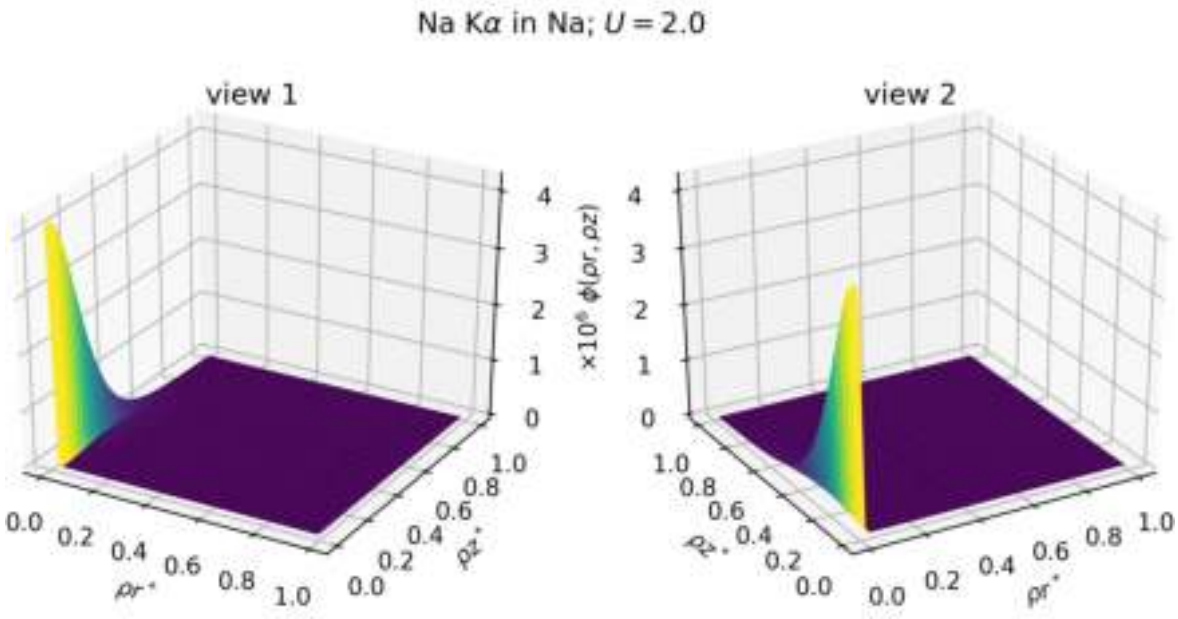

(b) Na $K\alpha$ line in Na; U = 2.0

Figure 15: Generated X-ray intensity distributions in Na K-α in Na obtained from Monte-Carlo simulations

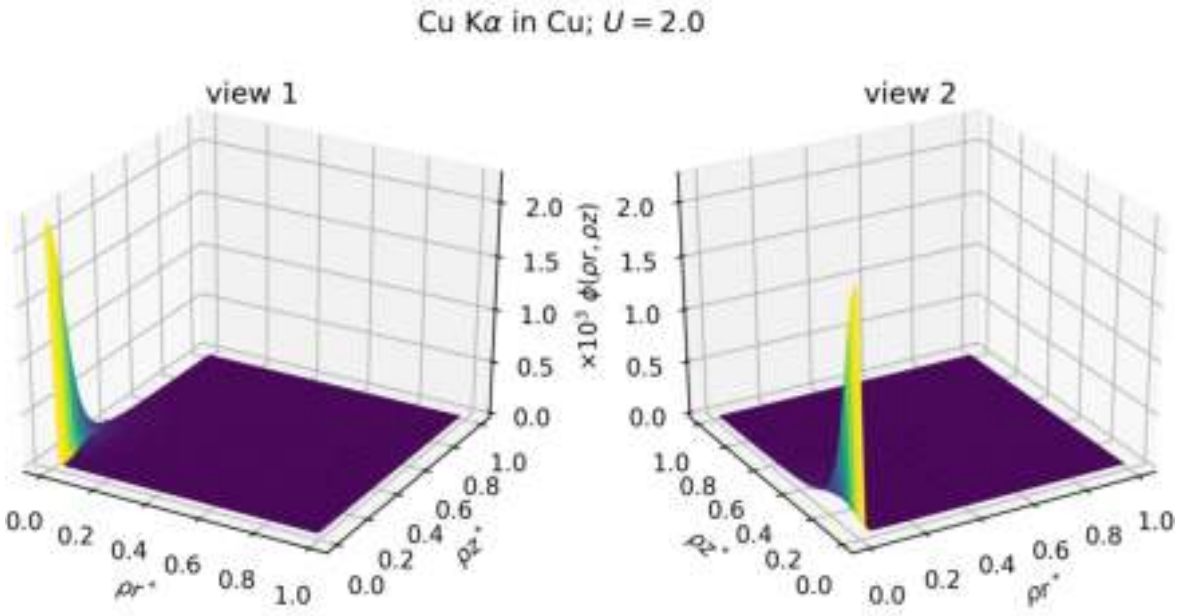

(a) Cu $K\alpha$ line in Cu; U = 2.0

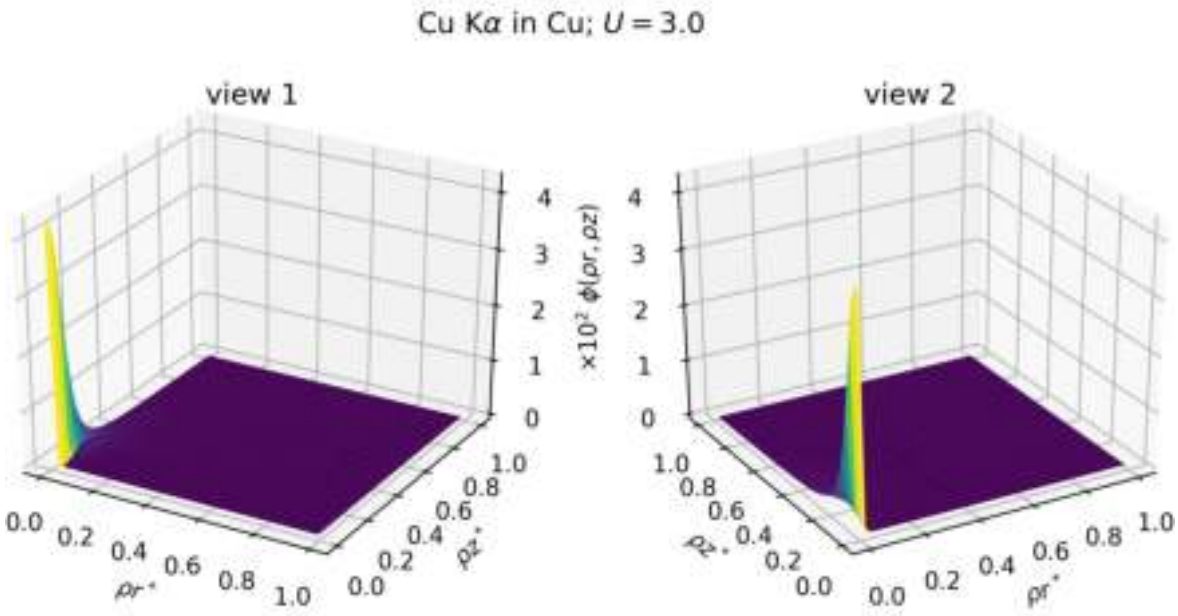

(b) Cu $K\alpha$ line in Cu; U = 3.0

Figure 16: Generated X-ray intensity distributions in Cu K-α in Cu obtained from Monte-Carlo simulations

4 Empirical Expression for the Generated X-ray Intensity Distribution

This section will describe the process involved in obtaining function fits. We decided to obtain an empirical function $\phi(\rho r, \rho z)$ in particular because, as discussed earlier, when the interaction volume has radial symmetry, this distribution describes the complete three dimensional distribution of generated X-ray intensities. Moreover, when there exists an analytical function for $\phi(\rho r, \rho z)$, it can be extended to the base cases of all other forms of distributions such as $\phi(\rho x, \rho y, \rho z)$, $\phi(\rho x, \rho z)$ and $\phi(\rho x)$ which are for homogeneous bulk materials and then be manipulated to include cases of heterogeneity. For example,

$$\phi(\rho x, \rho y, \rho z) = \phi\left(\rho r = \sqrt{(\rho x)^2 + (\rho y)^2}, \rho z\right), \tag{67}$$

$$\phi(\rho x, \rho z) = \int_{-\infty}^{\infty} \phi(\rho x, \rho y, \rho z) \mathrm{d}\rho y, \tag{68}$$

$$\phi(\rho x) = \int_{0}^{\infty} \phi(\rho x, \rho z) \mathrm{d}\rho z. \tag{69}$$

4.1 Challenges Faced while Predicting an Emperical Model for the Distribution

Three primary challenges had to be overcome while searching for functions that fit the data obtained from Monte-Carlo simulations well. They are as follows.

4.1.1 The Intensity at r = 0

As seen in the previous sections (sections 3.4.2, 3.6 and 3.7.3), the intensity close to the point of incidence of the beam is not well defined for both lateral distribution $\phi(\rho x)$ and radial distributions $\phi(\rho r)$ and $\phi(\rho r, \rho z)$. The value in this region blows up to infinity.

This is caused because a point beam is used as the source of electrons and the way in which the Monte-Carlo algorithm is structured. In the first step of the electron trajectory the electron is inserted into the material along the line of the electron beam, i.e along the negative Z-axis. As a result, there is always a certain amount of X-ray generation at $\rho r = 0$ and $\rho x = 0$, irrespective of how small we make the bin sizes, the minimum of which is determined by the distribution resulting from the very first step of electron trajectories. The distribution resulting from the first step of the electron trajectories can even be explicitly determined from the physical models used in the Monte-Carlo method. In our case, it can be determined from the distribution resulting

from equation (12) as

$$(\phi(\rho z))_{1^s tstep} = Q_{nl}\left(E_0 - \Delta E\left(|z|\right)\right) exp\left(-\frac{|z|}{\lambda}\right) \tag{70}$$

where λ is the mean free path defined in equation (13) , E_0 is the beam energy and $E_0 - \Delta E(z)$ is the distribution of energy with depth. $\Delta E(z)$ can be determined using an energy loss expression such as the one from Joy and Luo given in equation (18) by substituting path length s with $|z|$. As this distribution always persists along the line of incidence of the beam, the values of $\phi(\rho x = 0)$ and $\phi(\rho r = 0)$ increase indefinitely as we reduce the respective bin sizes.

4.1.2 Extreme Variation in Function Values

As can be seen in figure 15 and figure 16, the distribution from $\rho r = 0$ to $\rho r = D_x$ has values spanning several orders of magnitude. This becomes a problem while fitting curves because the residual from one part of the curve will dominate and skew the results. Using a different scale such as the logarithmic scale was not advantageous because the peak at $\rho r = 0$ still persists and the noise in the simulation at regions close to R_x and D_x is amplified. Other alternate solutions were considered, such as:

- Splitting the distribution into two parts along ρr, one close to $\rho r = 0$ and another covering the rest was attempted. However, a suitable metric defining the position of such a splitting could not be found. Also this method results in two functions and, potentially, more parameters and complexity.
- Obtaining two separate distributions, one considering all electron paths which have not yet deflected by at least $\pi/2$ (90°) from the direction of the incident electron beam and the other for the remainder of their trajectories. This was investigated because after the electron has deflected by a total at least $\pi/2$ from it's initial direction, the future deflections can be truly random, i.e. any information about the initial direction of travel is lost and diffusion is the dominant part of electron motion. But, this procedure did not simplify curve fitting because the problem of scale still existed in the first distribution and the second part is still influenced by the initial direction of travel. The latter was mostly because the electron density distribution itself is significantly affected by the initial direction of travel until the point of a trajectory where the deflection is more than $\pi/2$.

4.1.3 Variation in the Interaction Volume

Another challenge was the large variations in interaction volumes for the different cases considered. This made the function parameters vary drastically for the different cases and it would be difficult to obtain relations between the function parameters and physical parameters, i.e. the atomic number and over voltage ratio.

4.1.4 The Partial Cumulative Generated X-ray Intensity distribution

Our solution for the challenges discussed in section 4.1 is to use a new form the distribution $\phi(\rho r, \rho z)$ for curve fitting. Denoted as $\Phi_r(\rho r, \rho r)$, it is obtained by integrating $\phi(\rho r, \rho z)$ along ρr as follows:

$$\Phi_r(\rho r, \rho z) := \int_0^{\rho r} \phi(\hat{\rho r}, \rho z) 2\pi \hat{\rho r} \mathrm{d}\hat{\rho r} \tag{71}$$

The resulting distribution is much easier to predict and still carries most of the information required without much distortion. Figure 17 and figure Figure 18 give us a good representation of this cumulative distribution $\Phi_r(\rho r, \rho z)$. Since the integration is only along ρr, the distribution is a partial cumulative distribution. Similarly, integrating again along ρz would result in the complete cumulative distribution, but doing so makes it harder to accurately approximate features near $\rho z = 0$ and the maximum at $\rho z = R_m$.

To handle variations in the dimensions of the interaction volume, normalized values of ρr and ρz, given by $\rho r^* = 2\rho r / D_x$ and $\rho z^* = \rho z / R_x$ respectively, are used. D_x is the diameter of the interaction volume and R_x is the maximum depth range of the interaction volume. This results in ρr^* and ρz^* that only vary between 0 and 1 within the interaction volume. The empirical functions investigated as possible fits for the distribution in the following sections will be along these scaled axes, i.e. $\Phi_r^*(\rho r^*, \rho z^*)$.

4.1.5 Getting back the Non-Cumulative Generated X-ray Intensity Distribution

As described so far, the empirical functions will be designed for the X-ray Intensity distribution accumulated along ρr and with scaled co-ordinates ρr^* and ρz^*, i.e., ϕ. The non-cumulative distribution can be retrieved from this distribution as follows:

- $\Phi_r(\rho r, \rho z)$ can be obtained from $\Phi_r^*(\rho r, \rho z)$ as

$$\Phi_r(\rho r, \rho z) = \Phi^*(\rho r^*, \rho z^*) = \Phi_r^* \left(\frac{2\rho r}{D_x}, \frac{\rho z}{R_x} \right). \tag{72}$$

- $\phi(\rho r, \rho z)$ can be obtained from $\Phi_r(\rho r, \rho z)$ as

$$\phi(\rho r, \rho z) = \begin{cases} \dfrac{1}{2\pi \rho r} \dfrac{\partial \Phi_r(\rho r, \rho z)}{\partial \rho r} & \rho r \neq 0 \\ \Phi_r(\rho r = 0, \rho z) & \rho r = 0 \end{cases}. \tag{73}$$

4.2 Create a Database for Fitting

We need a database containing generated X-ray intensity distribution data on which we can fit our predicted function. Six X-ray lines were chosen for which the database

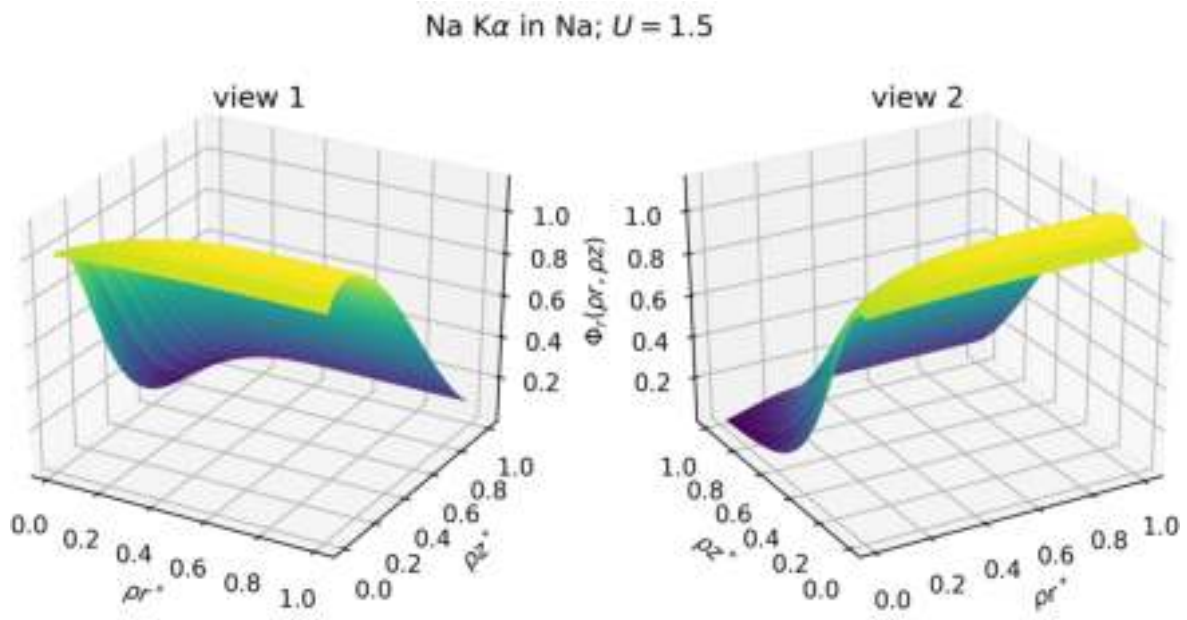

(a) Na $K\alpha$ line in Na; U = 1.5

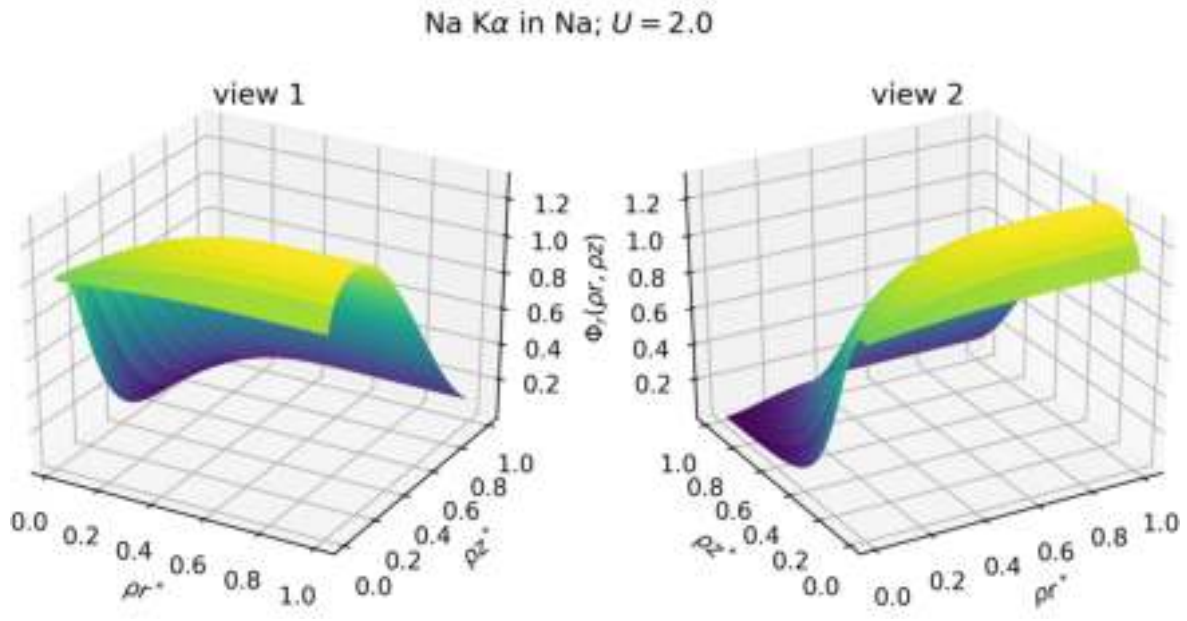

(b) Na $K\alpha$ line in Na; U = 2.0

Figure 17: $\Phi_r(\rho r, \rho z)$ for the same configurations in figure 15

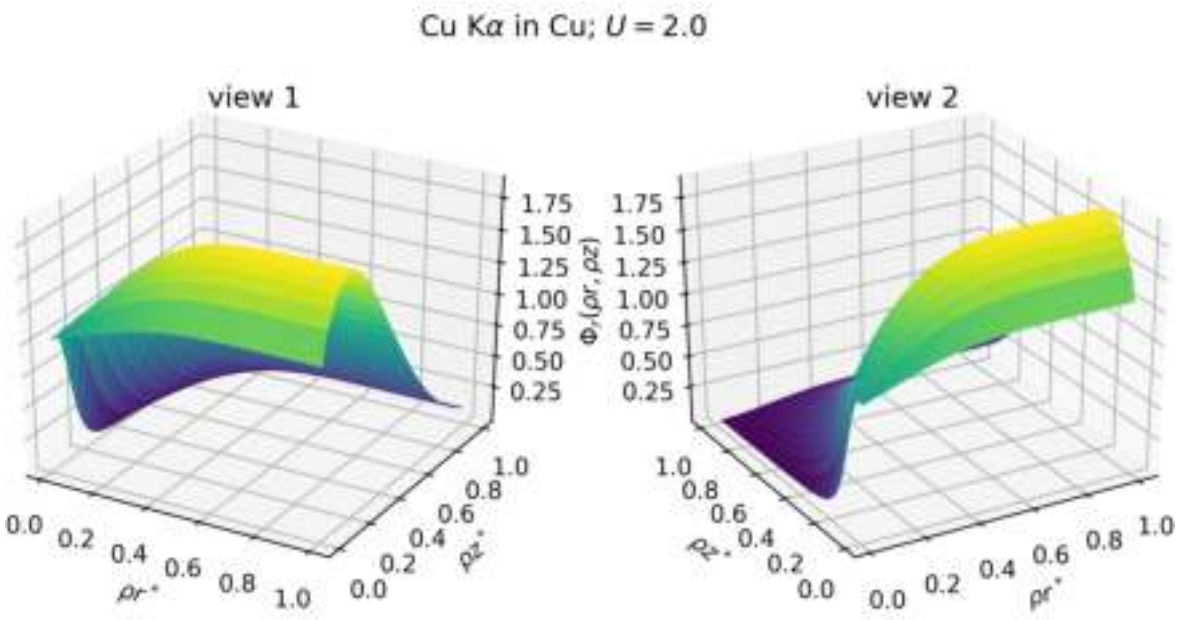

(a) Cu $K\alpha$ line in Cu; U = 2.0

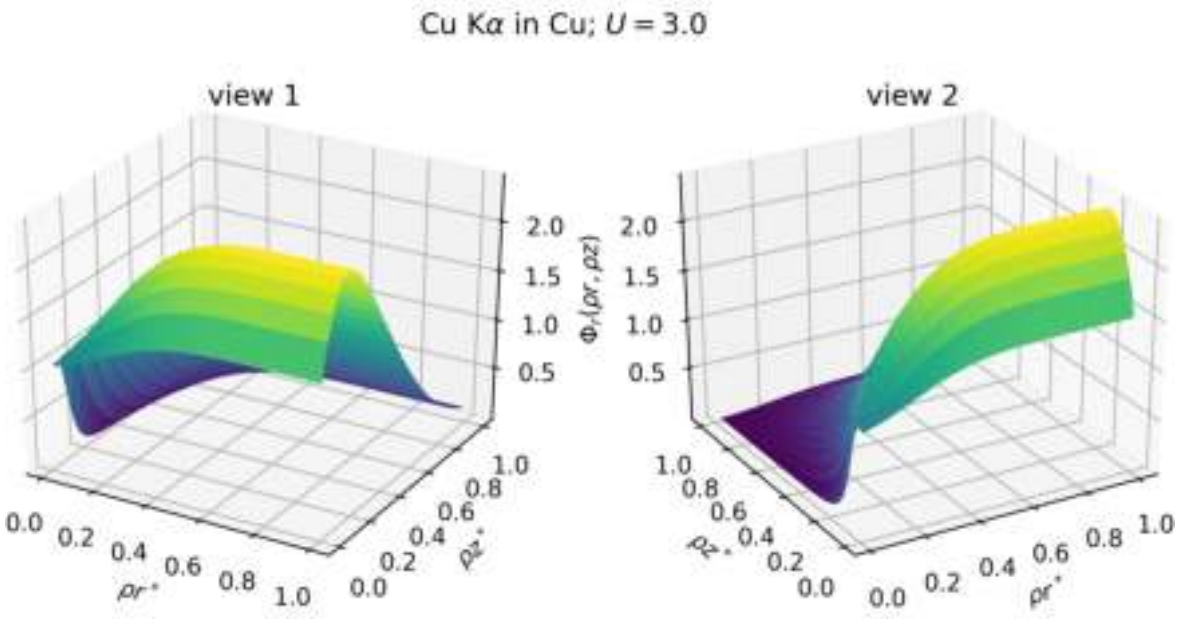

(b) Cu $K\alpha$ line in Cu; U = 3.0

Figure 18: $\Phi_r(\rho r, \rho z)$ for the same configurations in figure 16

X-ray \ U	1.2	1.5	2.0	3.0	5.0	7.0
C K-α	0.3492	0.4365	0.5820	0.8730	1.4550	2.0370
Na K-α	1.2768	1.5960	2.1280	3.1920	5.3201	7.4481
Si K-α	2.1942	2.7428	3.657	5.4855	9.1425	12.7995
Ca K-α	4.8182	6.0227	8.0303	12.0454	20.0757	28.1060
Cr K-α	7.1556	8.9446	11.9261	17.8891	29.8152	–
Cu K-α	10.7403	13.4254	17.9005	26.8508	–	–

Table 1: Beam energies in keV for different combinations of X-ray lines and over voltage ratios U.

Z	Element	Z	Element	Z	Element
3	Li	15	P	25	Mn
4	Be	16	S	26	Fe
5	B	19	K	27	Co
6	C	20	Ca	28	Ni
11	Na	21	Sc	29	Cu
12	Mg	22	Ti	30	Zn
13	Al	23	V	31	Ga
14	Si	24	Cr	32	Ge

Table 2: List of chosen matrix elements

would be generated. They are C K-α, Na K-α, Si K-α, Ca K-α, Cr K-α and Cu K-α lines. For each X-ray line six different over voltage ratios were also chosen. They are 1.2, 1.5, 2.0, 3.0, 5.0 and 7.0. The beam energies corresponding for all the combinations of X-ray lines and over voltage ratios are given in table 1. Over voltage ratios resulting in beam energies more than 30 keV were ignored and hence a few entries in table 1 are empty. Generated X-ray intensity distribution data for all the aforementioned cases in 24 different pure elemental material matrices with elements of atomic numbers ranging from 3 to 32 were obtained. Only elements that have solid forms at standard room temperatures are feasible as material matrices and they are listed in table 2. This results in a total of $(6 \times 6 - 3) \times 24 = 792$ unique experimental setups in the generated database.

4.3 Predicted empirical expression

As discussed earlier in section 4.1.4, the goal is to find functional fits for the distribution $\Phi_r^*(\rho r^*, \rho z^*)$. In a first step, the one dimensional distribution $\Phi_r^*(\rho r^* = \text{const}, \rho z^*)$ was investigated for different values of ρr^*. The distributions appear like a skewed form exponential or Gaussian distributions. Thus, first attempts were choosing simple modified exponential and Gaussian functions, such as $p_1(\rho x^*)\varphi(\rho x^*)$ where $p_1(\rho x^*)$ is

a linear polynomial in ρx^* and $\varphi(\rho x^*)$ is either an exponential or a Gaussian distribution. Then, other well known skewed distributions such as the log-normal distribution, gamma distribution, exponentially modified Gaussian distribution and skewed normal distribution were examined. Upon visual inspection of the plots of closest fits, it was found that the skewed normal distribution gave good approximations, especially for $\Phi_r^*(\rho r* \approx 1, \rho z^*)$ for many of the distributions in our accumulated database.

The skewed normal distribution was first described by O'Hagan and Leonard [41] as

$$f(x) = 2\varphi\left(\frac{x-\mu}{\sigma}\right)\Phi\left(\alpha\left(\frac{x-\mu}{\sigma}\right)\right) \tag{74}$$

where $\varphi(x)$ is the probability density function (PDF) of the Gaussian distribution and $\Phi(x)$ is the cumulative density function (CDF) of the same distribution. σ is the standard deviation and μ is the mean of the Gaussian distribution. Thus the skew normal distribution can be expanded as

$$\begin{aligned} f(x) &= 2 \cdot \frac{1}{\sigma\sqrt{2\pi}} \exp\left(-\frac{1}{2}\left(\frac{x-\mu}{\sigma}\right)^2\right) \cdot \int_{-\infty}^{\alpha\left(\frac{x-\mu}{\sigma}\right)} \frac{1}{\sqrt{2\pi}} \exp\left(-\frac{t^2}{2}\right) \mathrm{d}t \\ &= \frac{1}{\sigma\sqrt{2\pi}} \exp\left(-\frac{1}{2}\left(\frac{x-\mu}{\sigma}\right)^2\right)\left[1 + \operatorname{erf}\left(\frac{x-\mu}{\sigma\sqrt{2}}\right)\right], \end{aligned} \tag{75}$$

where erf is the error function. While, this function gave good fits for $\Phi_r^*(\rho r^* \approx 1, \rho z^*)$, it was not ideal for smaller values of $\rho r*$. In fact the distribution close to $\rho r^* \approx 0$ is much closer to an exponential distribution. Hence, the skew normal distribution had to be generalized. Azzalini [4] described a generalized class of functions of which the skew normal distribution would be a specific case of. This class of distributions is given by the same expression as in equation (74) but where $\varphi(x)$ could be any distribution with a PDF symmetric about its mean and $\Phi(x)$ is any CDF symmetric about the same mean.

Using the same principle a function based on a version of the generalized normal distribution was defined. The PDF and CDF of the generalized normal distribution are given by

$$\begin{aligned} \varphi(x) &= \frac{\beta}{2\sigma\Gamma(1/\beta)} \exp\left(-\left|\frac{x-\mu}{\sigma}\right|^\beta\right) \qquad \text{and} \\ \Phi(x) &= \frac{1}{2}\left[1 + \operatorname{sign}(\mathrm{x}-\mu)\frac{\gamma\left(\frac{1}{\beta}, \left|\frac{x-\mu}{\sigma}\right|^\beta\right)}{\Gamma(1/\beta)}\right] \end{aligned} \tag{76}$$

respectively, where Γ is the gamma function and γ is the lower incomplete gamma function. β is a positive real number which defines the power of the term in the exponent. Hence this distribution is also called exponential power distribution. Finally

a function $f_{1D}(\rho z^*) = \Phi_r^*(\rho r^* = \text{const.}, \rho z^*)$ was defined by using the expressions provided in equation (76) with mean $\mu = 0$ and formulating them as in equation (74), which results in

$$f_{1D}(\rho z^*) = k \exp\left(-\left|\frac{\rho z^*}{\sigma}\right|^{\beta}\right)\left[1 + \text{sign}\left(\frac{\alpha \rho z^*}{\sigma}\right)\frac{\gamma\left(\frac{1}{\beta}, \left|\frac{\alpha \rho z^*}{\sigma}\right|^{\beta}\right)}{\Gamma(1/\beta)}\right], \tag{77}$$

where $\sigma \in \mathbb{R}$, $\beta \in \mathbb{R}$, $\alpha \in \mathbb{R}$ and $k \in \mathbb{R}$ are the unknown function parameters. This function can be denoted as $f_{1D}(\rho z^*; \sigma, \beta, \alpha, k)$. Defining bounds for the arguments and parameters in this expression can make the function more easily differentiable and hence, easier to fit and manipulate.

- $\rho z \geq 0$ can be assumed since the origin of the co-ordinate system is generally placed at the point of incidence of the beam and by our convention, as discussed in section 3.3.2, ρz is positive along the depth.
- σ which is a measure of the standard deviation or the variance can also be restricted to be positive, i.e $\sigma \in (0, \infty]$. σ cannot be 0 because it appears in the denominator at several places.
- β is the power inside the exponential and is related to the kurtosis of the distribution. It was observed to be at least 1 at $\rho r^* \approx 0$ and increase as ρr^* is increased. Hence we can restrict β as $\beta \in [1, \infty)$
- α controls skewness of the distribution. When α is positive the distribution skews to the right (positive side) of the origin and when it is negative the distribution skews to the left. Since in our case the skewness is caused by the electrons exiting the material sample as back-scattered electrons, the distribution can only skew towards the positive side of the origin. Hence α can be restricted to be greater than 0, i.e., $\alpha \in [0, \infty)$.
- k is a parameter that controls the scale of the distribution. At $\rho z^* = 0$ the equation (77) reduces to

  $$f_{1D}(\rho z^* = 0) = k \cdot (1) \cdot [1 + 0] = k. \tag{78}$$

  Hence k is also a direct measure of the back-scattered electrons. $k = 1$ when there is no back-scattering. For any distribution $\Phi_r^*(\rho r^* = \text{const.}, \rho z^*)$, $k = 1 + b$, where $b \in [0, \infty)$ is a factor proportional to the total number of backscattered electrons and thus the amount of X-rays generated very close to the material surface, within a radius of $\rho r^* = \text{const.}$ from the origin or the point of electron beam incidence. Hence, the value of k can be constrained as $k \in [1, \infty)$

We can summarize the bounds for the function arguments and parameters as $\rho r^* \geq 0$, $\sigma \in (0, \infty)$, $\beta \in [1, \infty)$, $\alpha \in [0, \infty)$ and $k \in [1, \infty)$. By using these bounds we can get rid of the 'modulo' and 'sign' operators in equation (77), which makes the function

differentiable. The final form is given by,

$$f_{1D}(\rho z^*) = k \exp\left(-\left(\frac{\rho z^*}{\sigma}\right)^{\beta}\right)\left[1 + \frac{\gamma\left(\frac{1}{\beta}, \left(\frac{\alpha\rho z^*}{\sigma}\right)^{\beta}\right)}{\Gamma(1/\beta)}\right]. \tag{79}$$

4.3.1 Extension to two dimensions

The function presented in equation (79) was fitted for all values of available ρr^* for a subset of the database and from the visual inspection of plots comparing the data and the fitted function, it was found to fit reasonably well. The obtained function parameters were studied and it was found that they all vary with respect to ρr^* in a, more or less, similar way which closely resembled the error function. Hence, the 2D formulation was arrived at as follows:

- A set of function parameters for the $f_{1D}(\rho z^*; \sigma, \beta, \alpha, k)$ were obtained by curve fitting at $\rho r^* \approx 0$ and analysed, say σ_0, β_0, α_0 and k_0 respectively. It was found that setting $\beta_0 = 1$, $\alpha_0 = 1$ and $k = 1$ didn't make much difference and the function would fit well just with one variable parameter σ_0. Thus the distribution at $\rho r^* \approx 0$ can be summarized as

$$f_{1D}(\rho r^* \approx 0, \rho z^*) = \exp\left(-\frac{\rho z^*}{\sigma_0}\right)\left[1 + \frac{\gamma\left(1, \frac{\rho z^*}{\sigma_0}\right)}{\Gamma(1)}\right]. \tag{80}$$

  Using the CDF of the exponential distribution for the second term we can also write the distribution as

$$f_{1D}(\rho r^* \approx 0, \rho z^*) = \exp\left(-\frac{\rho z^*}{\sigma_0}\right)\left[2 - \exp\left(-\frac{\rho z^*}{\sigma_0}\right)\right]. \tag{81}$$

- Similarly, the function parameters that best fit the distribution at $\rho r \approx 1$ were obtained and analysed. Let us call them say σ_1, β_1, α_1 and k_1 respectively. Here, all the parameters vary depending on simulation parameters and no simplification was possible. We can write the distribution as

$$f_{1D}(\rho r^* \approx 1, \rho z^*) = k_1 \exp\left(-\left(\frac{\rho z^*}{\sigma_1}\right)^{\beta_1}\right)\left[1 + \frac{\gamma\left(\frac{1}{\beta_1}, \left(\frac{\alpha_1\rho z^*}{\sigma_1}\right)^{\beta_1}\right)}{\Gamma(1/\beta_1)}\right]. \tag{82}$$

  This distribution, in actuality, must represent the more popular $\phi(\rho z)$ because we are already accumulating the distribution along ρr as shown in equation (71).

- We then defined a way in which the distribution could grow gradually from that shown in equation (80) to that in equation (82) as we move from $\rho r^* = 0$ to

$\rho r^* = 1$. The function $g(\rho r^*)$, based on the error function, describes this growth -

$$g(\rho r^*) = \text{erf}\left(\frac{\rho x^*}{\lambda}\right). \tag{83}$$

The error function when differentiated gives a Gaussian. $\lambda \in (0, \infty)$ should be small enough to yield $g(\rho r^* = 1) \approx 1$.

The two dimensional function obtained using this method can be represented as follows:

$$f_{2D}(\rho r^*, \rho z^*) = k(\rho r^*) \exp\left(-\left(\frac{\rho z^*}{\sigma(\rho r^*)}\right)^{\beta(\rho r^*)}\right)\left[1 + \frac{\gamma\left(\frac{1}{\beta(\rho r^*)}, \left(\frac{\alpha(\rho r^*)\rho z^*}{\sigma(\rho r^*)}\right)^{\beta(\rho r^*)}\right)}{\Gamma(1/\beta(\rho r^*))}\right] \tag{84}$$

where

$$\begin{aligned}
&\sigma(\rho r^*) = \sigma_0 + (\sigma_1 - \sigma_0) \cdot g(\rho r^*),\\
&\beta(\rho r^*) = 1 + (\beta_1 - 1) \cdot g(\rho r^*),\\
&\alpha(\rho r^*) = 1 + (\alpha_1 - 1) \cdot g(\rho r^*),\\
&k(\rho r^*) = 1 + (k_1 - 1) \cdot g(\rho r^*),\\
&g(\rho r^*) = \text{erf}\left(\frac{\rho r^*}{\lambda}\right).
\end{aligned} \tag{85}$$

This results in a function with constant parameters λ, σ_0, σ_1, β_1, α_1 and k_1. The distribution can be represented as $f_{2D}(\rho r^*, \rho z^*; \lambda, \sigma_0, \sigma_1, \beta_1, \alpha_1, k_1)$.

4.4 The Process of Curve-Fitting

Once a candidate function is chosen with a specific set of function parameters, the parameters can be estimated to best for the data using an optimization algorithm. Consider a function that connects the inputs X to the output Y as

$$f(X; \Omega) = Y \tag{86}$$

where $\Omega = (\omega_1, \omega_2, \ldots, \omega_m)$ is a set of m parameters in the function definition of f. For example:

- When fitting for the one-dimensional function given in equation (79), the function f would be $f_{1D}(\rho z^*; \sigma, \beta, \alpha, k)$, where $X \equiv \rho z^*$, $Y \equiv \Phi_r^*(\rho r^* = \text{const.}, \rho z^*)$ and $\Omega \equiv (\sigma, \beta, \alpha, k)$;

- When fitting for the two-dimensional function in equation (84), the function f would be $f_{2D}(\rho r^*, \rho z^*; \lambda, \sigma_0, \sigma_1, \beta_1, \alpha_1, k_1)$, where $X \equiv (\rho r^*, \rho z^*)$, $Y \equiv \Phi_r^*(\rho r^*, \rho z^*)$ and $\Omega \equiv (\lambda, \sigma_0, \sigma_1, \beta_1, \alpha_1, k_1)$.

In order to estimate the function m parameters Ω, we need at least $n \geq m$ data points in X and Y, denoted by $[x_1, x_2, \ldots, x_n]$ and $[y_1, y_2, \ldots, y_n]$ respectively. Typically, the parameters can only fall within specified bounds depending on the problem. We shall denote the lower bounds as $(\omega_1^{lb}, \omega_2^{lb}, \ldots, \omega_m^{lb})$ and the upper bounds as $(\omega_1^{ub}, \omega_2^{ub}, \ldots, \omega_m^{ub})$. Then the problem of obtaining the function parameters can be stated as follows.

Problem 1 *Given a function $f(X;\Omega) = Y$, find the m parameters*

$$\Omega = \left(\omega_1 \in [\omega_1^{lb}, \omega_1^{ub}], \omega_2 \in [\omega_2^{lb}, \omega_2^{ub}], \ldots, \omega_m \in [\omega_m^{lb}, \omega_m^{ub}]\right)$$

such that the system of $n \geq m$ equations

$$\begin{aligned} f(x_1;\Omega) &= y_1 \\ f(x_1;\Omega) &= y_1 \\ \vdots &= \vdots \\ f(x_n;\Omega) &= y_n \end{aligned}$$

is satisfied.

It is not always possible to find an exact solution to problem 1 and hence an approximate solution can be arrived at by using iterative methods that minimize the residual $r_i = f(x_i;\Omega) - y_i$ or a function of the residual $\rho(r_i)$ called the loss function, where $i = 1, 2, \ldots, n$ corresponding to the data points used for fitting. The most popular class of methods used in this regard are the least squares method, which minimize the sum of the square of the residual or loss, i.e. $\sum_{i=1}^{n}(\rho(r_i))^2$. Examples of the loss function include:

- $\rho(r) = r$ - a simple linear loss function,
- $\rho(r) = 2(\sqrt{1 + |r|} - 1)$ - a non-linear loss function which is a smooth approximation of the $l1$ loss,
- $\rho(r) = \log(1 + |r|)$ - a non-linear loss function which is also called as the Cauchy loss, etc.

The simple linear loss function is significantly affected by data outliers and hence, makes the least square methods employing them less robust. The Non-linear loss functions have been developed, particularly, to address this problem. These non-linear loss functions, when used, improve the robustness of the least squares algorithm, and they differ from each other on how aggressively they ignore outliers.

The problem of minimising the loss function can thus be stated as

Problem 2 *Given a function* $f(X;\Omega) = Y$*, find the* m *parameters*

$$\Omega = \left(\omega_1 \in [\omega_1^{lb}, \omega_1^{ub}], \omega_2 \in [\omega_2^{lb}, \omega_2^{ub}], \ldots, \omega_m \in [\omega_m^{lb}, \omega_m^{ub}]\right)$$

which minimizes

$$\bar{\rho} = \sum_{i=1}^{n} \rho(r_i)^2$$

where,

$$r_i = f(x_i;\Omega) - y_i.$$

The approximate solution for problem 2 Ω_{sol} can be summarized as

$$\Omega_{sol} = \min_{\Omega} \left\{ \sum_{i=1}^{n} \left[\rho\left(f(x_i;\Omega) - y_i\right)\right]^2 \right\}. \tag{87}$$

The most popular methods used for least squares approximations include the Levenberg-Marquardt method and the trust region based methods. We used a trust region based method, more generally called the trust region method, for the purpose of curve fitting. The reasons for this choice include better handling of bounds, better compatibility with non-linear loss functions and better overall robustness.

4.4.1 The Trust-Region Method

The trust region method starts with an initial approximation and makes a series of incremental updates to this approximation until a target condition is reached. At each k-th iteration an approximate solution Ω_k obtained as an incremental update over the previous approximation Ω_{k-1} is evaluated. A trust region defined by Δ_k is defined around this approximation, and a new approximate solution Ω_{k+1} is obtained within this region by moving in a certain ideal direction and not exceeding the bounds of the trust region. If the new approximation is substantially better than the current approximation, the step is accepted and the trust region is moved to the new approximation and expanded. If the new approximation is only slightly better compared to the current approximation, the step is accepted and the trust region is moved without altering its size. Whereas, if the new approximation is worse than the current approximation, the step is rejected and the trust region is contracted. This procedure is repeated until a suitable approximation is obtained. The specifics of the trust region method varies with implementations, some of the more robust implementation being quite non-trivial. Hence, the following description will only be a representation of a simple trust region based algorithm

Let us assume that the algorithm is at its k-th iteration of the algorithm and that our current approximation for $\Omega \in \mathbb{R}^m$ is $\Omega_k \in \mathbb{R}^m$ and the corresponding sum of squared loss is $\bar{\rho}_k$. A candidate step increment $\boldsymbol{p}_k$ is then computed as a minimiser of the quadratic equation which is given by

$$\boldsymbol{p}_k = \min_{\boldsymbol{p}} \left\{ m_k(\boldsymbol{p}) = \bar{\rho}_k + \boldsymbol{g}_k^{\mathrm{T}} \boldsymbol{p} + \frac{1}{2} \boldsymbol{p}^{\mathrm{T}} \boldsymbol{B} \boldsymbol{p} \right\}, \qquad \text{such that } \|\boldsymbol{p}\| \leq \Delta_k, \tag{88}$$

where Δ_k represents the size of the trust region, $\boldsymbol{g}_k \in \mathbb{R}^m$ is the gradient at the current approximation Ω_k and $\boldsymbol{B}_k \in \mathbb{R}^{m \times m}$ is the Hessian or an approximation to the Hessian at the current approximation. This sub problem is the same as the Newton method of second order and definitions of this sub-problem can vary with implementations. The solution $\boldsymbol{p}_k$ can be computed using several methods such as the Cauchy-point method, the dog-leg method and the conjugate gradient Steihaug's method. After the step increment $\boldsymbol{p}_k$ is computed, the new candidate solution $\Omega_{k+1} = \Omega_k + \boldsymbol{p}_k$ and the corresponding squared loss $\bar{\rho}_{k+1}$ are computed. To measure the relative goodness of the new candidate solution a new quantity τ is computed as

$$\tau = \frac{\bar{\rho}_{k+1} - \bar{\rho}_k}{0 - m_k(\boldsymbol{p}_k)}. \tag{89}$$

τ is the ratio of the real improvement $(\bar{\rho}_{k+1} - \bar{\rho}_k)$ to the predicted improvement $(0 - m_k(\boldsymbol{p}_k))$. To evaluate τ, three different thresholds η_1, η_2 and η_3 are defined such that $0 \leq \eta_1 < \eta_2 < \eta_3$. The evaluation is carried out as follows.

- $\tau < \eta_1$ indicates a poor approximation and results in the rejection of the new solution Ω_{k+1}. The trust region is contracted.
- If $\eta_1 \leq \tau < \eta_2$, the new solution is just good enough to be accepted, but the trust region needs expansion.
- If $\eta_2 \leq \tau < \eta_3$, the new solution is quite good and hence is accepted, while the size of the trust region Δ_k is not altered.
- If $\tau \geq \eta_3$, the new solution is considerable good and hence the trust region can be expanded after accepting the increment.

Two scaling factors t_1 and t_2, such that $0 < t_1 < 1 < t_2$, are defined and used in the contraction and expansion of the trust region, respectively. A pseudocode for the trust region described above is given in algorithm 4

We used the implementation of the curve-fitting and least-squares methods provided in the `scipy` library for python, as found in the `scipy.optimize.curve_fit` and `scipy.optimize.least_squares` routines respectively. We used the smooth $l1$ loss function (`'soft_l1'` in `scipy`) given by $\rho(r) = 2(\sqrt{1 + |r|} - 1)$ as our loss function. The trust region method implemented in the `least_squares` routine is derived from [11]. The `Curve Fitting toolbox` available in `Matlab` was also used to prototype and improve our predicted functions, as it provides an intuitive and real-time GUI.

Data: The function $f(X, \Omega)$;
loss function ρ;
data $X = \{x_1, x_2, \ldots, x_n\}$ and $Y = \{y_1, y_2, \ldots, y_n\}$;
initial approximation Ω_0; tolerance ϵ;
max. no. of iterations k_{max};
thresholds η_1, η_2 and η_3;
scaling factors t_1 and t_2;
max. trust region size Δ_{max}.
Result: Approximate solution Ω_{trm}.
$\Omega_1 \leftarrow \Omega_0$;
$\bar{\rho}_1 \leftarrow \sum_{i=1}^{1} [\rho(f(x_i, \Omega_1) - y_i)]^2$;
for $k \leftarrow 1, 2, \ldots, k_{max}$ **do**
  $\boldsymbol{p}_k \leftarrow \min_{\boldsymbol{p}} \left\{ m_k(\boldsymbol{p}) = \bar{\rho}_k + \boldsymbol{g}_k^{\mathrm{T}} \boldsymbol{p} + \frac{1}{2} \boldsymbol{p}^{\mathrm{T}} \boldsymbol{B} \boldsymbol{p} \right\}$, such that $\|\boldsymbol{p}\| \leq \Delta_k$;
  $\Omega_{k+1} \leftarrow \Omega_k + \boldsymbol{p}_k$;
  $\bar{\rho}_{k+1} \leftarrow \sum_{i=1}^{1} [\rho(f(x_i, \Omega_k) - y_i)]^2$;
  $\tau \leftarrow \dfrac{\bar{\rho}_{k+1} - \bar{\rho}_k}{0 - m_k(\boldsymbol{p}_k)}$;
  if $\tau < \eta_2$ **then**
    $\Delta_{k+1} \leftarrow t_1 \Delta_k$;
  else if $\tau \geq \eta_3$ **then**
    $\Delta_{k+1} \leftarrow \min(t_2 \Delta_k, \Delta_{Max})$;
  else
    $\Delta_{k+1} \leftarrow t_1 \Delta_k$;
  end
  if $\tau < \eta_1$ **then**
    $\Omega_{k+1} \leftarrow \Omega_k$;
    $\bar{\rho}_{k+1} \leftarrow \bar{\rho}_k$;
  end
  if $\bar{\rho}_{k+1} < \epsilon$ **then**
    break out of loop;
  end
end
$\Omega_{trm} \leftarrow \Omega_{k+1}$;

Algorithm 4: Pseudocode for the basic Trust Region Method

4.5 Results of Curve-Fitting

Curve fitting for the predicted function was performed on all the distributions in the generated database. We evaluated the obtained plots by tabulating the root mean squared (rms) errors and by visually inspecting plots of the fitted function overlaid on the data. It was observed the obtained fits were a good approximation for all the distributions in our database with rms errors exceeding 0.1 only for a very few cases. Figures 19, 20, 21 are a good representation of this. The distributions in these figures were chosen so as to include all major variations in the shape of the distributions and as can be seen from these plots the model provides good approximation for all of them, i.e. there are not any major deviations in the shape of the curves compared to the data.

Figure 22 shows plots of the rms error of the obtained fits for each of the considered X-rays against the over-voltage ratios U and atomic numbers Z of the matrices. The error seems to increase with increase in the over-voltage ratio and seems to be unaffected by the atomic number of the matrix. Fig 19a, which shows the distribution and fit for the C Kα line for a high over-voltage ratio of 7, represents one such case of a high rms error of about 1.2. As can be seen from the plot there is still only a minor deviation from the data.

4.5.1 Comparison with the PAP Model

Since our model describes the partial cumulative distribution $\Phi_r(\rho r, \rho z)$, the approximation for $\phi(\rho z)$ is already contained in the model, i.e.

$$\phi(\rho z) = \int_0^\infty \phi(\rho r, \rho z) 2\pi\rho r \mathrm{d}\rho z \approx \int_0^{D_x/2} \phi(\rho r, \rho z) 2\pi\rho r \mathrm{d}\rho z = \Phi_r\left(\rho r = \frac{D_x}{2}, \rho z\right). \tag{90}$$

Transforming both sides to the scaled co-ordinate ρr^* and ρz^* would result in

$$\phi^*(\rho z^*) = \Phi_r^*\left(\rho r^* = 1, \rho z^*\right). \tag{91}$$

This distribution can be readily obtained from equation (82). Hence, we wanted to compare $\phi(\rho z)$ obtained from our model with the popular PAP model. The PAP model is defined based on the features of the distribution - the integral of the distribution F, the range of ionization R_x, the depth of maximum generated X-ray intensity R_m and the surface X-ray generation intensity $\phi(0)$. Hence the PAP model can be computed easily if we already have the distribution from which F, R_x, R_m and $\phi(0)$ can be determined, the PAP description for the distribution can be obtained. Some, comparisons of our model and the PAP model can be found in Figure 23. From the plots it can be seen that our model more closely approximates the distribution. This is likely because our model is more flexible and accommodates various curvatures controlled by the power β inside the exponential term, whereas the PAP model is restricted to be parabolic or quadratic in nature.

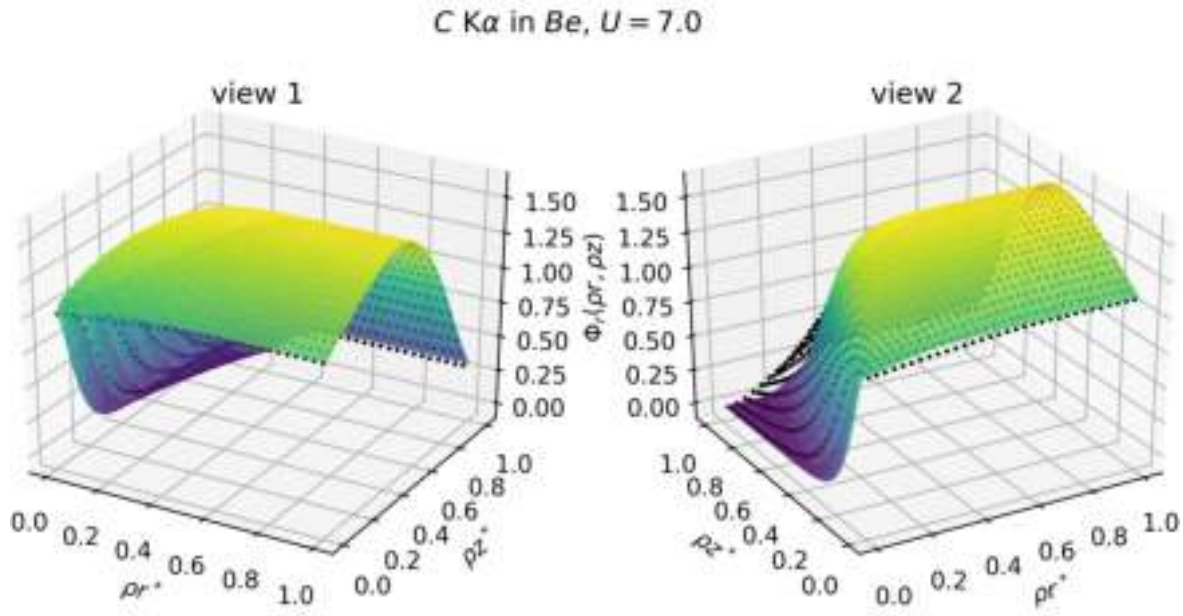

(a) C Kα line in Be; $U = 7.0$

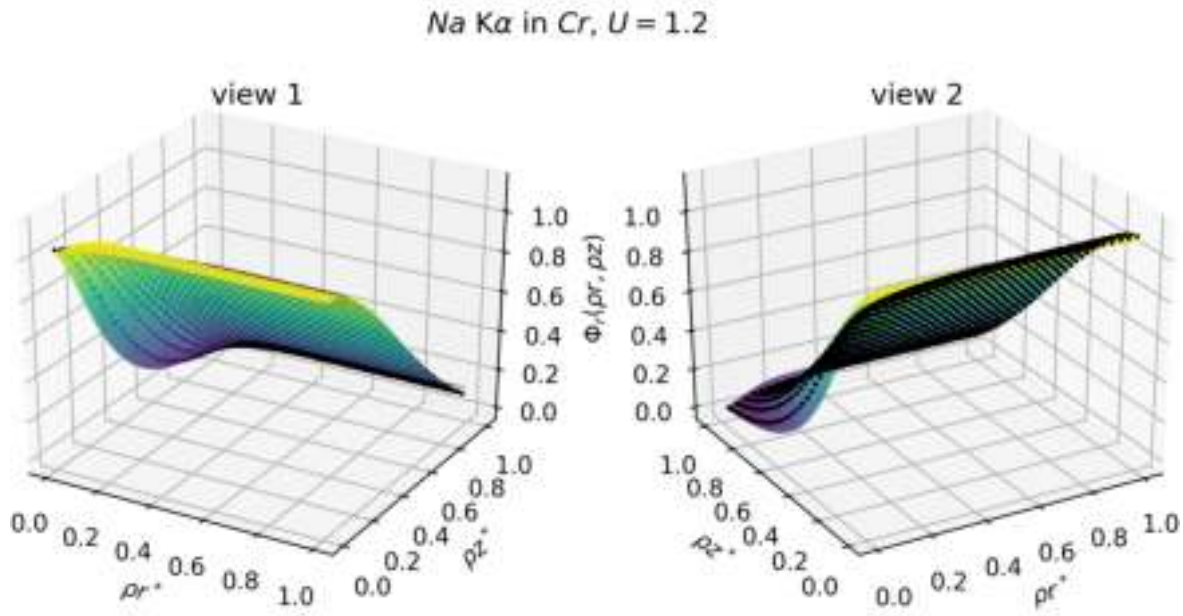

(b) Na Kα line in Cr; $U = 1.2$

Figure 19: Curve fits for $\Phi_r(\rho r, \rho z)$; points represent data and the surface represents the fitted function

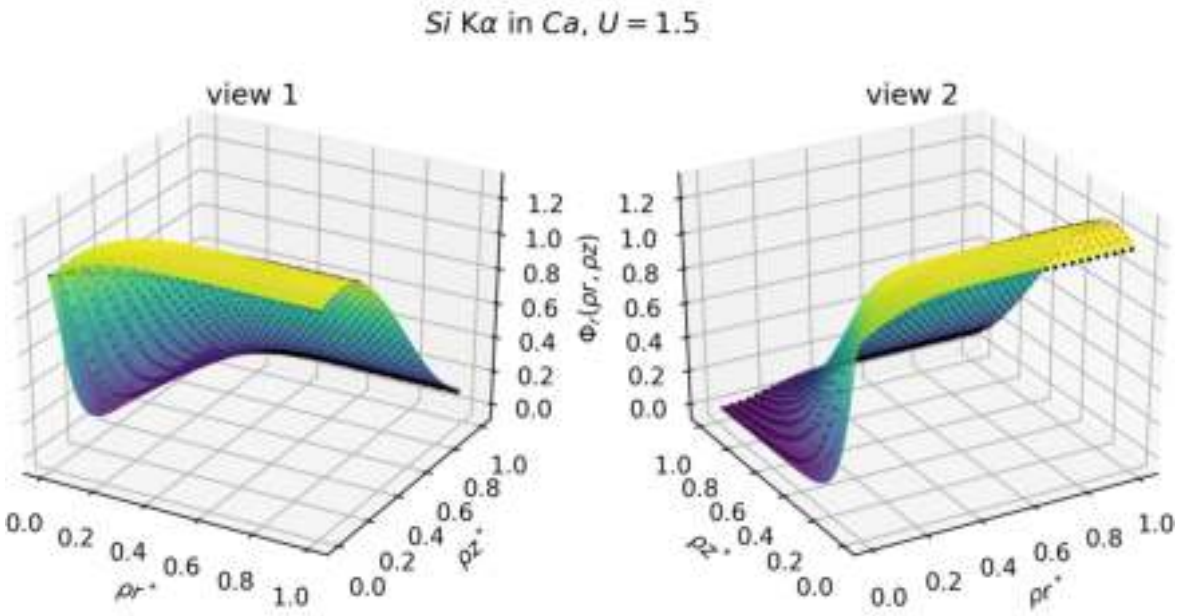

(a) Si Kα line in Ca; $U = 1.5$

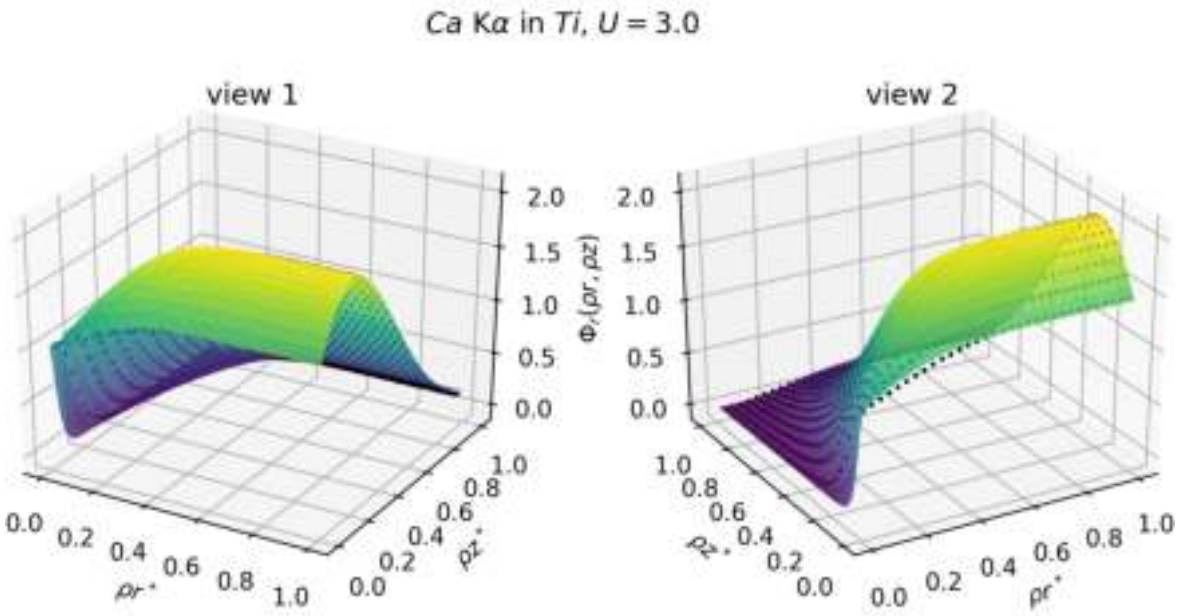

(b) Ca Kα line in Ti; $U = 3.0$

Figure 20: Curve fits for $\Phi_r(\rho r, \rho z)$; points represent data and the surface represents the fitted function

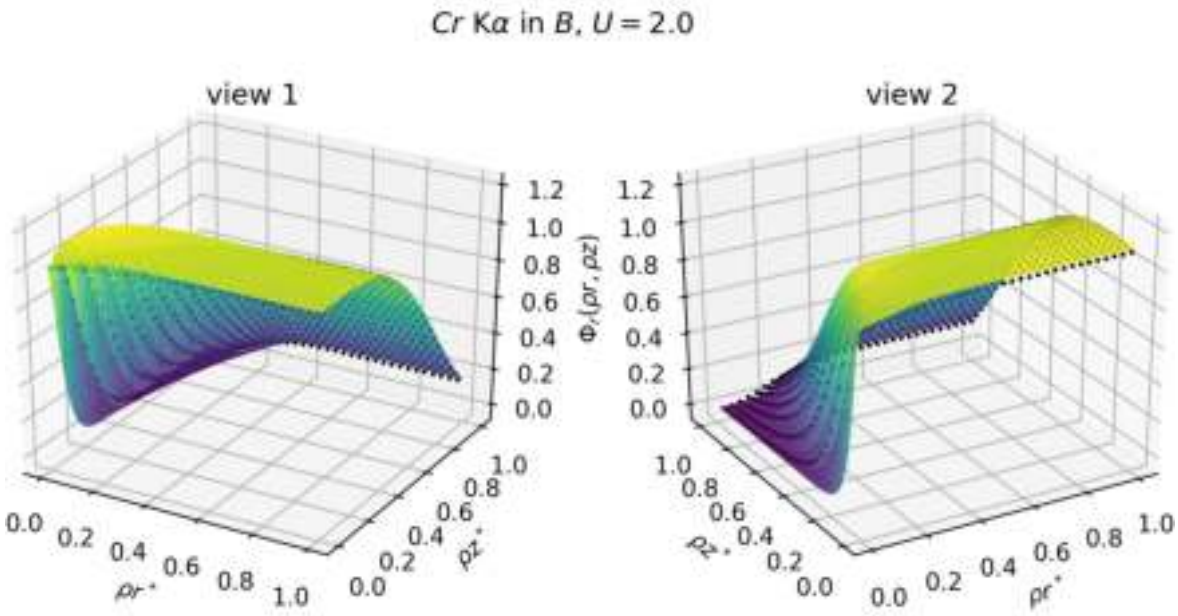

(a) Cr Kα line in B; $U = 2.0$

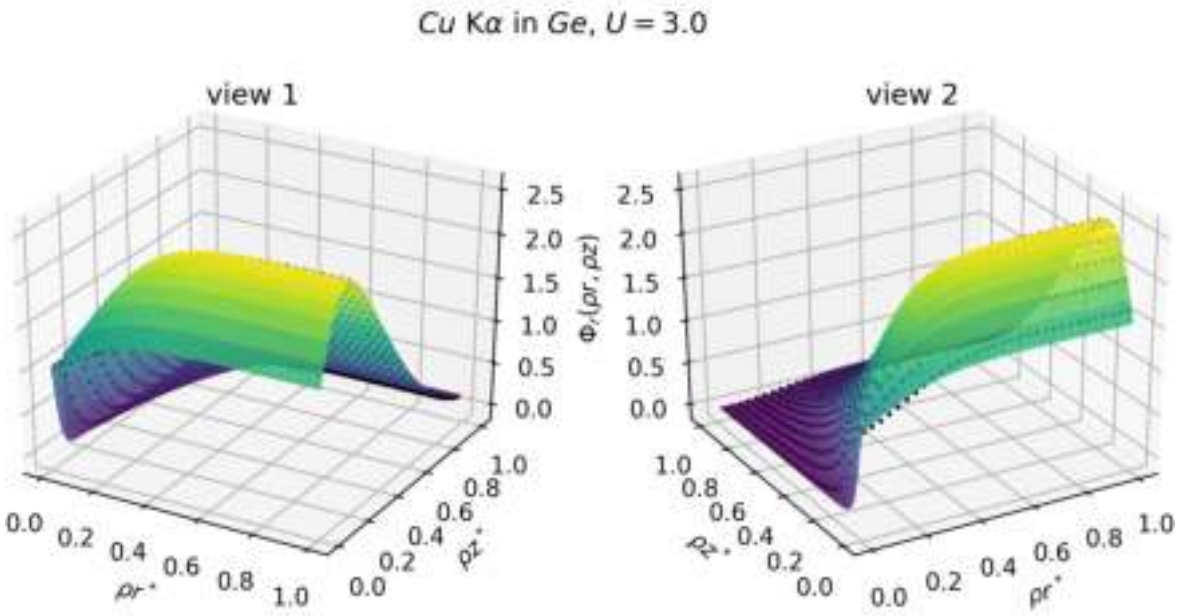

(b) Cu Kα line in Ge; $U = 3.0$

Figure 21: Curve fits for $\Phi_r(\rho r, \rho z)$; points represent data and the surface represents the fitted function

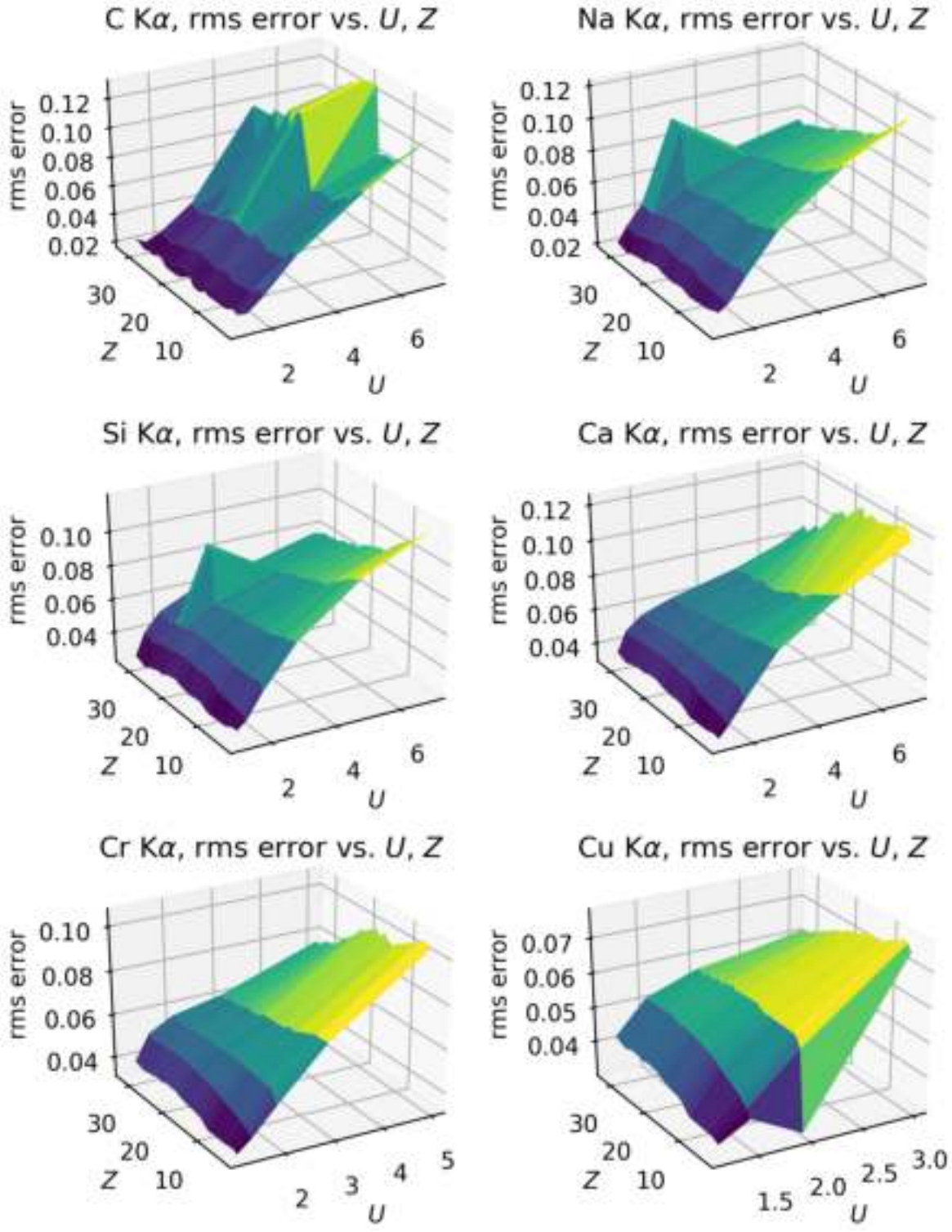

Figure 22: The root mean squared (rms) error in the obtained curve fits

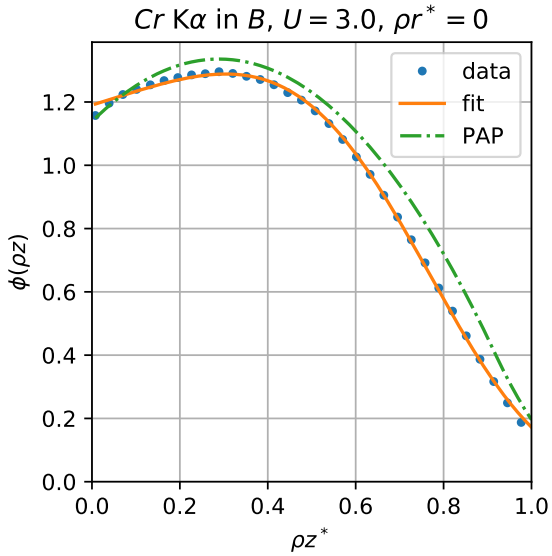

(a) Cr Kα in B, $U = 3$

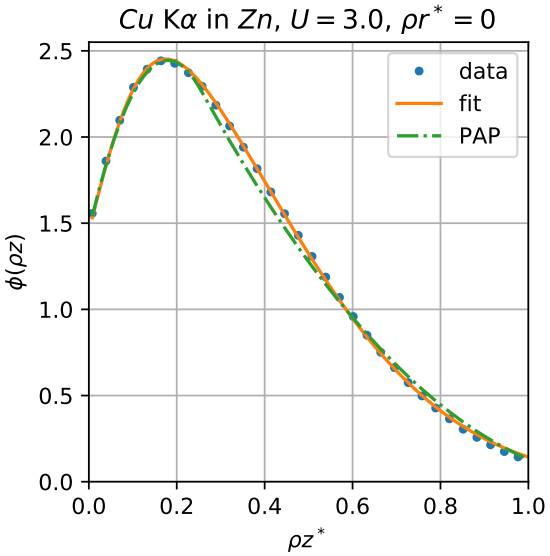

(b) Cu Kα in Zn, $U = 3$

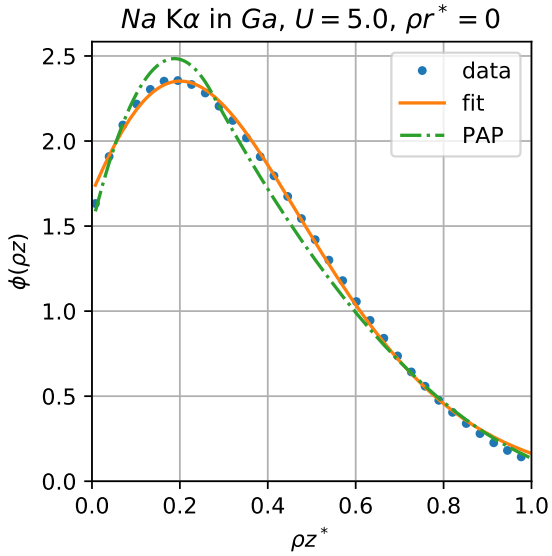

(c) Na Kα in Ga, $U = 3$

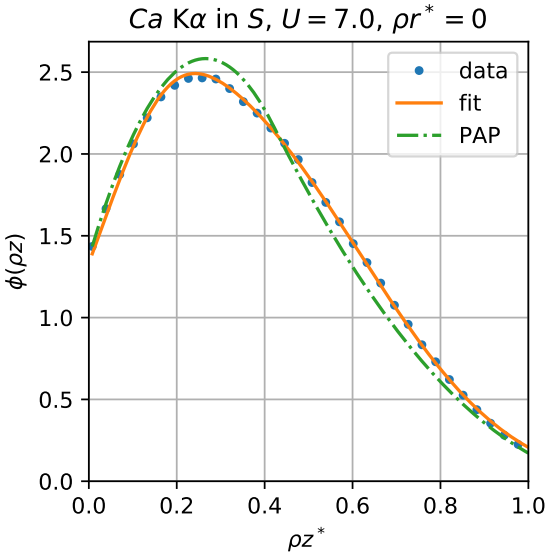

(d) Ca Kα in S, $U = 7$

Figure 23: Comparison of $\phi(\rho z)$ obtained from our model with the PAP model.

4.5.2 Limitations of our Model

Our model approximates very well the distribution $\Phi_r^*(\rho r^*, \rho z^*)$ near $\rho r = 1$. Close to $\rho r = 0$, the distribution changes more drastically, in general, compared to what can be estimated using our model. Hence our distribution lags the actual distribution as we move from $\rho r^* = 0$ to $\rho r^* = 1$, but catches up pretty quickly. Figure 24 shows how the function performs at various radial distances. It should also be noted when moving along ρr^* from 0 to 1 much of the change happens close to $\rho r^* = 0$. This is also depicted in the plots in figure 24. A side effect of our model underestimating the drastic changes near $\rho r = 0$ is that when the expression is differentiated, according to equation (73), in order to obtain $\phi(\rho r, \rho z)$ the resulting peak distribution at $\rho r \approx 0$ would deviate much more from the data. This is depicted in figure 25 for two example cases. This can be a problem when there are heterogeneities in the sample with changes in concentrations particularly in this region, i.e. close to $\rho r \approx 0$.

4.6 Dependence of the Parameters on Simulation parameters

The variation of the obtained fitted function parameters with respect to the simulation parameters, namely the atomic number Z of the material matrix and the electron beam energy E_0, here expressed as over-voltage ratio U, was also investigated. Several polynomial based functions of U and Z were found to predict these parameters. These functions are listed below.

$\boldsymbol{\lambda}$: A two dimensional polynomial of degree 2 and 1 with respect to U and Z respectively was found to give a decent approximation for λ. The polynomial is as follows:

$$\lambda(U, Z) = {p^{\lambda}}_{00} + {p^{\lambda}}_{10}U + {p^{\lambda}}_{01}Z + {p^{\lambda}}_{20}U^2 + {p^{\lambda}}_{11}UZ. \tag{92}$$

$\boldsymbol{\sigma_0}$: A similar two dimension polynomial of degree 2 and 1 with respect to U and Z respectively, but inverted, was found to give a good approximation of σ_0, i.e.

$$\frac{1}{\sigma_0(U, Z)} = {p^{\sigma_0}}_{00} + {p^{\sigma_0}}_{10}U + {p^{\sigma_0}}_{01}Z + {p^{\sigma_0}}_{20}U^2 + {p^{\sigma_0}}_{11}UZ \tag{93}$$

or

$$\sigma_0(U, Z) = \left[{p^{\sigma_0}}_{00} + {p^{\sigma_0}}_{10}U + {p^{\sigma_0}}_{01}Z + {p^{\sigma_0}}_{20}U^2 + {p^{\sigma_0}}_{11}UZ\right]^{-1}. \tag{94}$$

$\boldsymbol{\sigma_1}$: It was found observed σ_1 and β_1 varied somewhat similarly and hence curve fitting was attempted for the quantity $1/(\sigma_1\beta_1)$. With this manipulation, a simple two dimensional polynomial, linear in both U and Z was found to be sufficient in

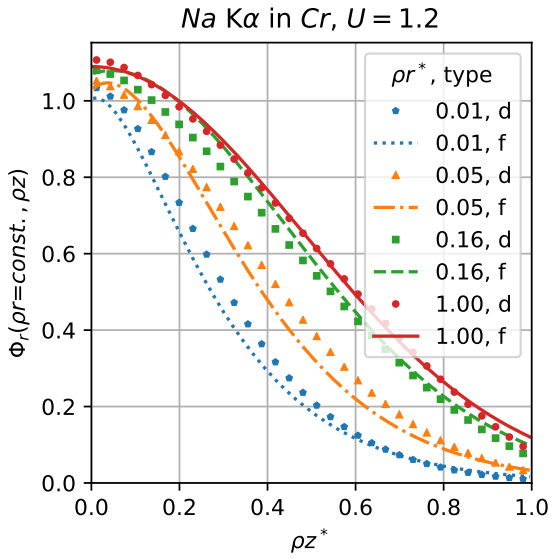

(a) Na Kα in Cr, $U = 1.2$

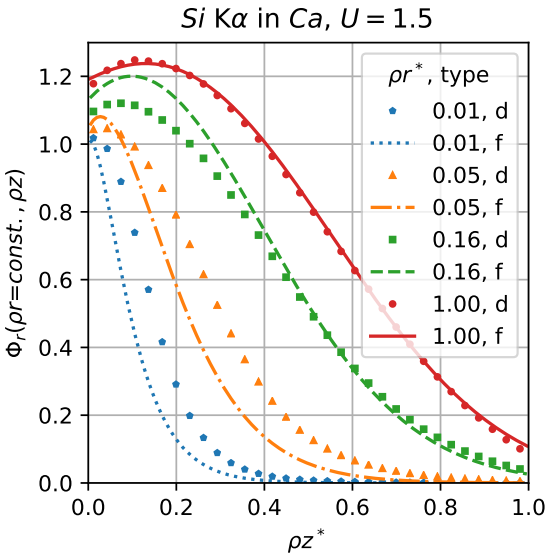

(b) Si Kα in Ca, $U = 1.5$

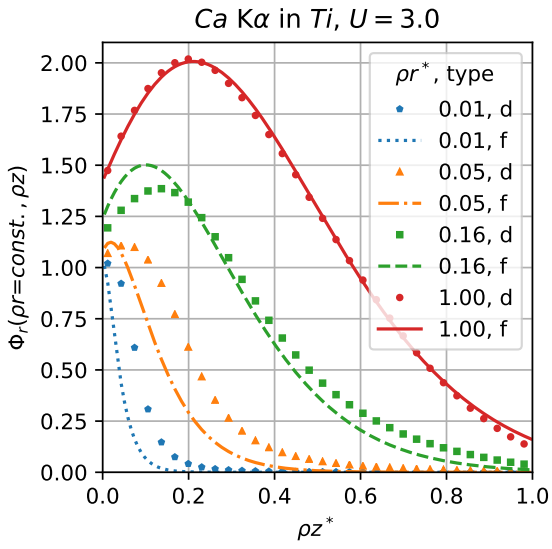

(c) Ca Kα in Ti, $U = 3$

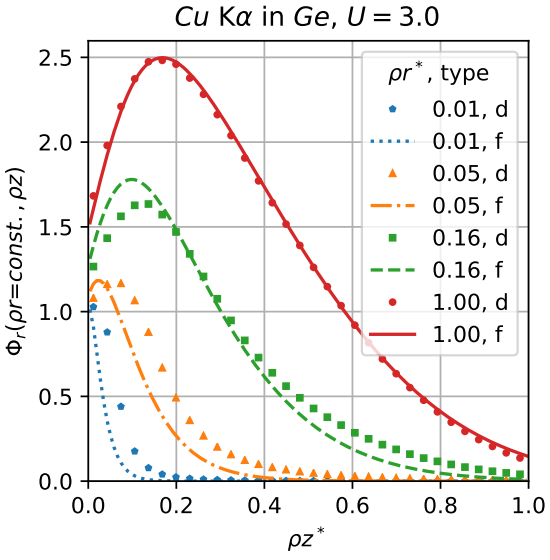

(d) Ca Kα in S, $U = 3$

Figure 24: Fit obtained by our model w.r.t ρz at various radial distances ρr^*. 'd' represents data and 'f' represents the fitted model

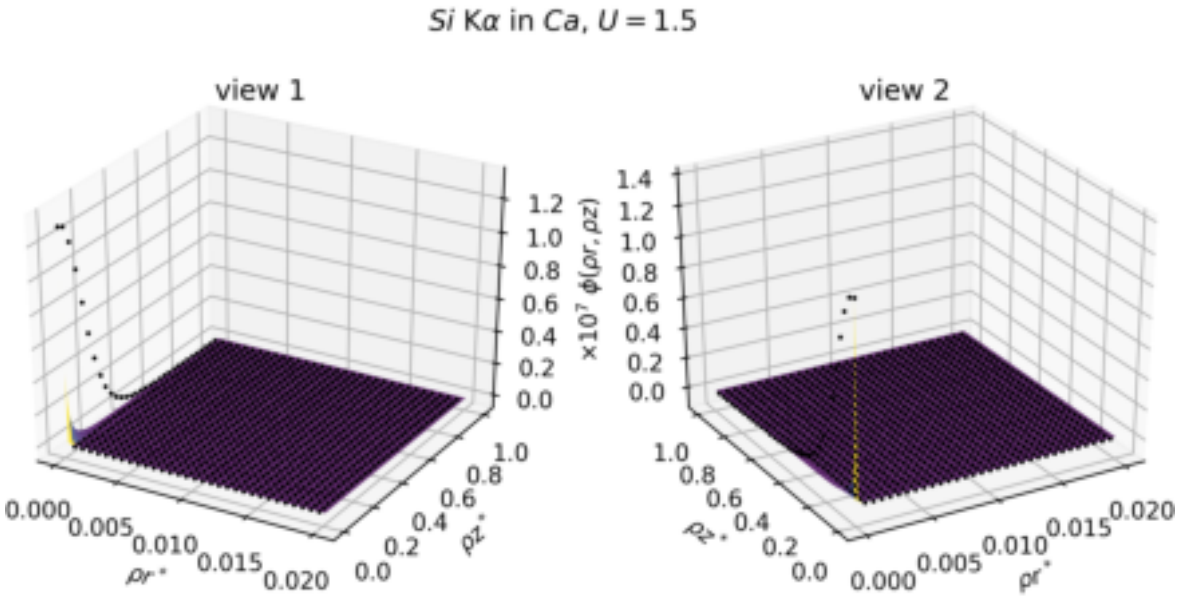

(a) Si Kα line in Ca; $U = 1.5$

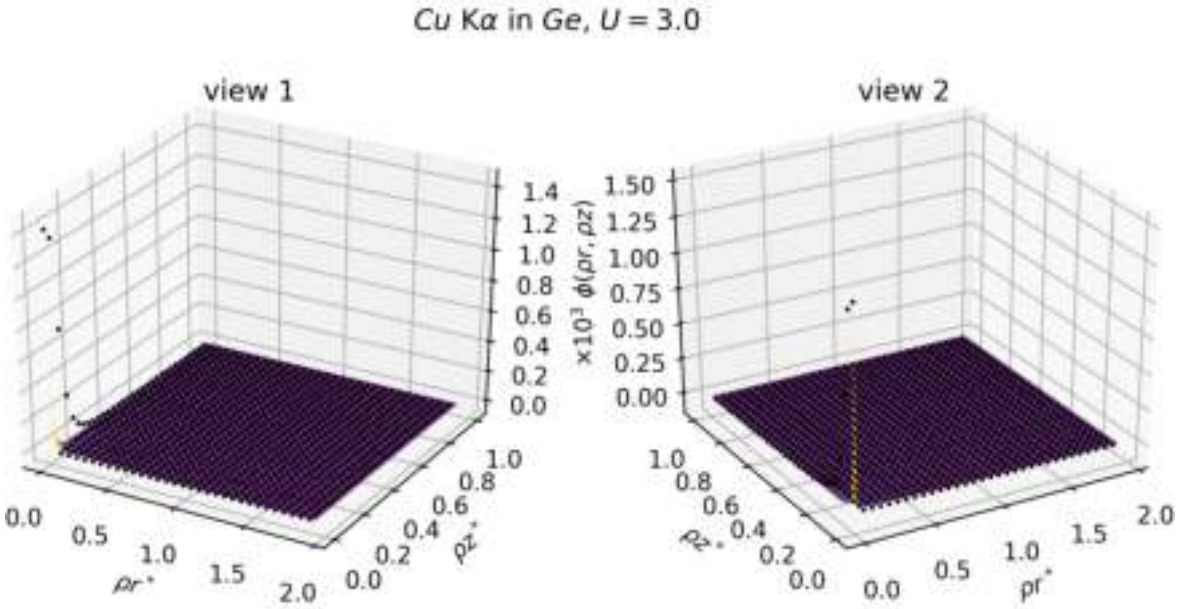

(b) Cu Kα line in Ge; $U = 3.0$

Figure 25: Comparizon between $\phi(\rho r, \rho z)$ obtained from numerical differentiation of the fitted model and the data from Monte-Carlo Simualtions. Deviation near $\rho r \approx 0$ is apparent.

order to approximate the σ_1. The polynomial approximation used can be is as follows

$$\frac{1}{\sigma_1(U,Z)\beta_1(U,Z)} = p^{\sigma_1}{}_{00} + p^{\sigma_1}{}_{10}U + p^{\sigma_1}{}_{01}Z \tag{95}$$

or

$$\sigma_1(U,Z) = \frac{1}{\beta_1(U,Z)}\left[p^{\sigma_1}{}_{00} + p^{\sigma_1}{}_{10}U + p^{\sigma_1}{}_{01}Z\right]^{-1}. \tag{96}$$

$\boldsymbol{\beta_1}$: The approximation for β_1 is obtained by an inverted two dimensional polynomial similar to σ_0. The approximating function is given by,

$$\frac{1}{\beta_1(U,Z)} = p^{\beta_1}{}_{00} + p^{\beta_1}{}_{10}U + p^{\beta_1}{}_{01}Z + p^{\beta_1}{}_{20}U^2 + p^{\beta_1}{}_{11}UZ \tag{97}$$

or

$$\beta_1(U,Z) = \left[p^{\beta_1}{}_{00} + p^{\beta_1}{}_{10}U + p^{\beta_1}{}_{01}Z + p^{\beta_1}{}_{20}U^2 + p^{\beta_1}{}_{11}UZ\right]^{-1}. \tag{98}$$

$\boldsymbol{\alpha_1}$: It was found that a two dimensional polynomial of degree 2 in U ad degree 1 in Z could approximate α_1 well. It is given by,

$$\alpha_1(U,Z) = p^{\alpha_1}{}_{00} + p^{\alpha_1}{}_{10}U + p^{\alpha_1}{}_{01}Z + p^{\alpha_1}{}_{20}U^2 + p^{\alpha_1}{}_{11}UZ \tag{99}$$

$\boldsymbol{k_1}$: A similar two dimensional polynomial to that used for the approximation of α could be used for the approximation of k_1, i.e.

$$k_1(U,Z) = p^{k_1}{}_{00} + p^{k_1}{}_{10}U + p^{k_1}{}_{01}Z + p^{k_1}{}_{20}U^2 + p^{k_1}{}_{11}UZ \tag{100}$$

Curve fitting was performed using the `Curve Fitting` toolbox available in `Matlab`. The parameters of these functions that estimate the parameters used in the empirical model for $\Phi_r^*(\rho r^*, \rho z^*)$ as functions of U and Z are tabulated in table 3 for the six X-ray lines considered. Further, as examples, figure 26 shows the obtained fits for the parameters of C Kα line and figure 27 shows the obtained fits for the parameters of Cr Kα line. As can be noted from the aforementioned tables and figures, we require a separate set of parameters for every X-ray line. This could be a major drawback of the method. Since the effect of inelastic cross-sections, corresponding to the X-ray line being measured, is integrated into the approximation of ϕ it is not possible to isolate the influence of the X-ray line being measured.

X-ray / param.	C K-α	Na K-α	Si K-α	Ca K-α	Cr K-α	Cu K-α
$p^{\lambda}{}_{00}$	0.2152	0.2689	0.2793	0.2871	0.2704	0.2502
$p^{\lambda}{}_{10}$	0.0628	0.06632	0.06185	0.05712	0.05084	0.03492
$p^{\lambda}{}_{01}$	-0.01137	-0.004052	-0.0017	0.0005057	0.002787	0.005897
$p^{\lambda}{}_{20}$	-0.0119	-0.02148	-0.01971	-0.01508	-0.009105	-0.002875
$p^{\lambda}{}_{11}$	-0.0005675	0.0001905	-0.0007542	-0.004203	-0.003621	-0.002234
$p^{\sigma_0}{}_{00}$	10.88	29.09	43.24	70.04	77.19	76.02
$p^{\sigma_0}{}_{10}$	5.545	15.93	22.91	31.06	30.38	19.09
$p^{\sigma_0}{}_{01}$	-0.8858	-1.739	-1.733	2.007	0.966	1.432
$p^{\sigma_0}{}_{20}$	-0.5978	-1.94	-3.345	-7.382	-9.066	-5.986
$p^{\sigma_0}{}_{11}$	-0.6198	-1.022	-0.8613	2.968	2.984	3.025
$p^{\sigma_1}{}_{00}$	3.152	3.297	3.31	3.402	3.431	3.452
$p^{\sigma_1}{}_{10}$	0.03859	0.04248	0.005444	0.04325	0.000894	0
$p^{\sigma_1}{}_{01}$	-0.04529	-0.0743	-0.08516	-0.1023	-0.1082	-0.1218
$p^{\beta_1}{}_{00}$	0.5847	0.5313	0.5192	0.5289	0.5324	0.5362
$p^{\beta_1}{}_{10}$	-0.02038	-0.04227	-0.02896	-0.01926	-0.00466	0.007629
$p^{\beta_1}{}_{01}$	0.04023	0.05032	0.04999	0.04966	0.05157	0.05639
$p^{\beta_1}{}_{20}$	-0.02318	0.005762	0.003811	-0.02527	-0.02491	-0.02426
$p^{\beta_1}{}_{11}$	-0.0002961	-0.007288	-0.007887	-0.006772	-0.008086	-0.008156
$p^{\alpha_1}{}_{00}$	1.665	1.696	1.822	1.839	1.782	1.559
$p^{\alpha_1}{}_{10}$	0.7576	0.6344	0.6709	0.8395	0.8429	0.6898
$p^{\alpha_1}{}_{01}$	0.2317	0.2349	0.2739	0.3857	0.4103	0.4269
$p^{\alpha_1}{}_{20}$	-0.3451	-0.2102	-0.2485	0.05064	-0.0237	0.01342
$p^{\alpha_1}{}_{11}$	0.09934	0.02213	0.0544	0.1314	0.1157	0.08212
$p^{k_1}{}_{00}$	1.285	1.417	1.438	1.498	1.424	1.335
$p^{k_1}{}_{10}$	0.1874	0.2001	0.2	0.2	0.1707	0.09984
$p^{k_1}{}_{01}$	0.009355	0.06924	0.08309	0.09207	0.08387	0.07635
$p^{k_1}{}_{20}$	-0.03206	-0.06352	-0.0593	-0.1062	-0.08182	-0.04631
$p^{k_1}{}_{11}$	0.01749	0.03971	0.03238	0.02966	0.02984	0.03078

Table 3: Results of curve fitting for the parameters obtained in section 4.5 as functions of the over-voltage ratio U and atomic no. Z of the matrix element

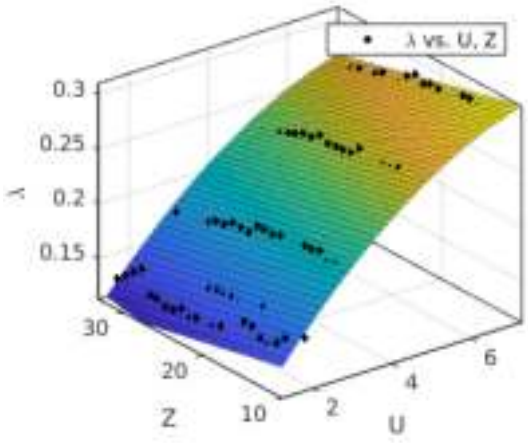

(a) Parameter λ

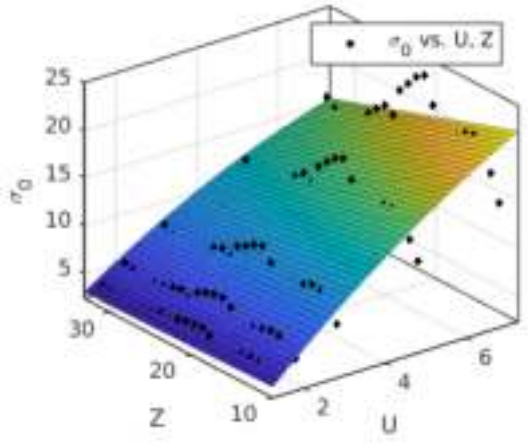

(b) Parameter σ_0

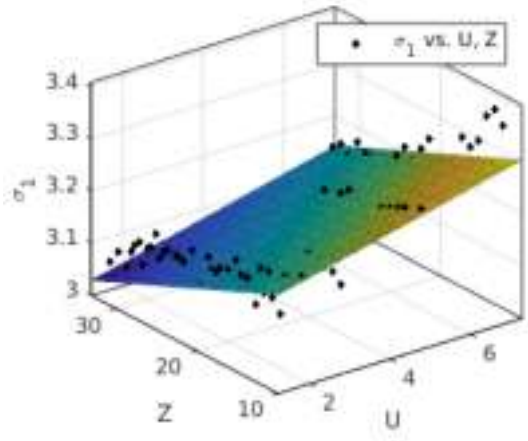

(c) Parameter σ_1

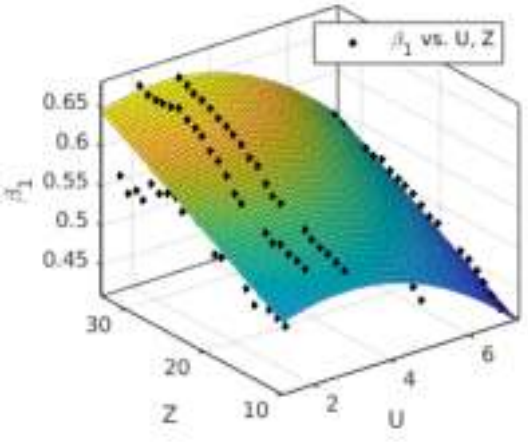

(d) Parameter β_1

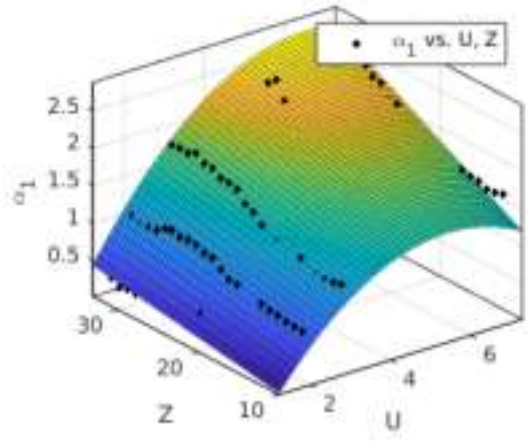

(e) Parameter α_1

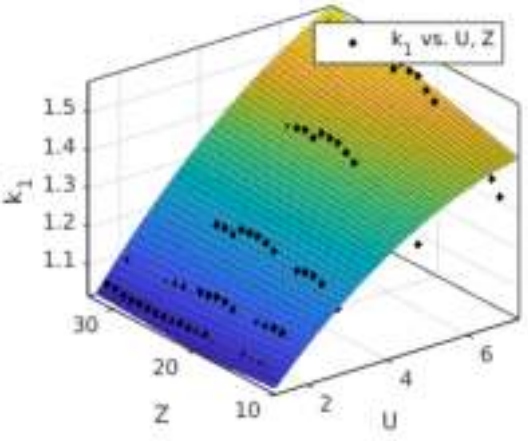

(f) Parameter k_1

Figure 26: Curve fitting results for the model parameters for C Kα X-ray line as functions of over-voltage ratio U and atomic no. of the matrix element Z

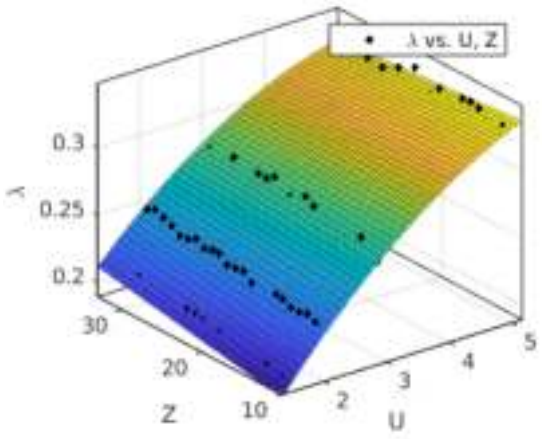

(a) Parameter λ

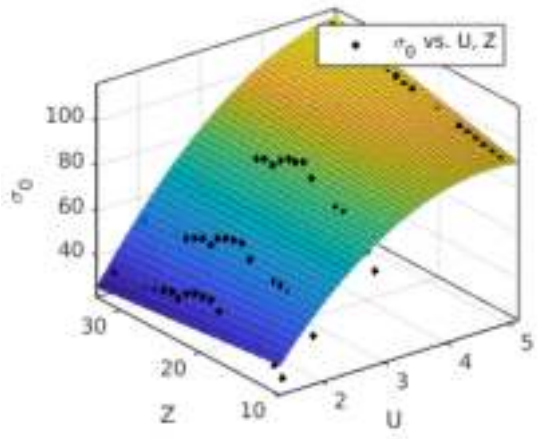

(b) Parameter σ_0

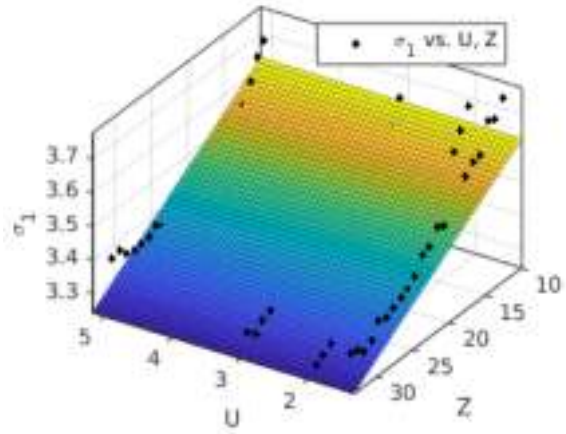

(c) Parameter σ_1

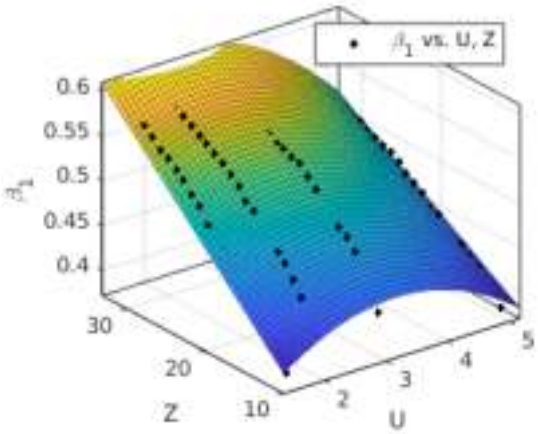

(d) Parameter β_1

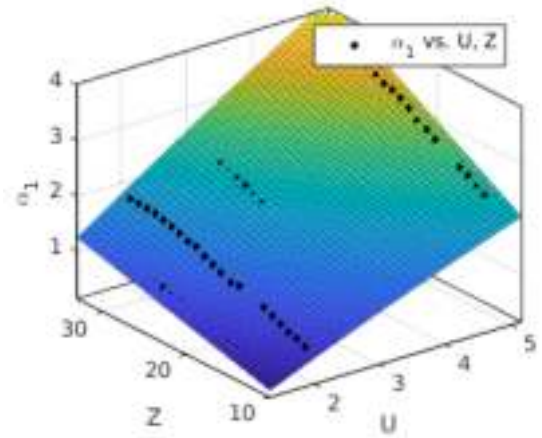

(e) Parameter α_1

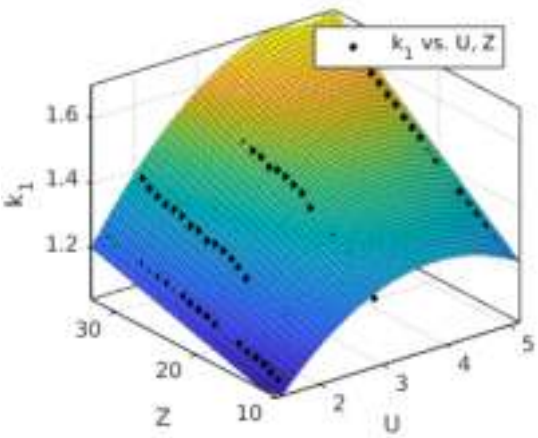

(f) Parameter k_1

Figure 27: Curve fitting results for the model parameters for Cr Kα X-ray line as functions of over-voltage ratio U and atomic no. of the matrix element Z

5 Conclusion

The goal of this project was to develop an empirical model for the generated X-ray intensity distribution ϕ in Electron Probe Micro-analysis in multiple dimensions. In this regard, the vertical distribution $\phi(\rho z)$, the lateral distribution $\phi(\rho x)$, the radial distribution $\phi(\rho r)$ and the two dimensional distribution $\phi(\rho r, \rho z)$ were obtained from Monte-Carlo simulations for several examples and studied. The possibility of modelling $\phi(\rho r, \rho z)$ was investigated. Due to difficulties involved in directly modelling $\phi(\rho r, \rho z)$, an empirical model for describing a partial cumulative version of this distribution, given by $\Phi_r(\rho r, \rho z) = \int_0^{\rho r} \phi(\hat{\rho r}, \rho z) 2\pi \hat{\rho r} \mathrm{d}\hat{\rho r}$ was developed. The model is given by

$$\Phi_r(\rho r, \rho z) = k(\rho r^*) \exp\left(-\left(\frac{\rho z^*}{\sigma(\rho r^*)}\right)^{\beta(\rho r^*)}\right) \left[1 + \frac{\gamma\left(\frac{1}{\beta(\rho r^*)}, \left(\frac{\alpha(\rho r^*)\rho z^*}{\sigma(\rho r^*)}\right)^{\beta(\rho r^*)}\right)}{\Gamma(1/\beta(\rho r^*))}\right],$$

$$\begin{aligned}
\sigma(\rho r^*) &= \sigma_0 + (\sigma_1 - \sigma_0) \cdot g(\rho r^*), \\
\beta(\rho r^*) &= 1 + (\beta_1 - 1) \cdot g(\rho r^*), \\
\alpha(\rho r^*) &= 1 + (\alpha_1 - 1) \cdot g(\rho r^*), \\
k(\rho r^*) &= 1 + (k_1 - 1) \cdot g(\rho r^*), \\
g(\rho r^*) &= \mathrm{erf}\left(\frac{\rho r^*}{\lambda}\right), \\
\rho r^* = \frac{2\rho r}{D_x} \quad &\text{and} \quad \rho z^* = \frac{\rho r}{R_x},
\end{aligned}$$

where D_x and R_x are the maximum diameter and depth range of X-ray generation respectively. The model was evaluated using curve fitting on a database of 792 unique examples and was found to approximate the distributions quite well with root mean squared errors generally lower than 0.1. Visual inspection of the plots of the fitted functions overlaid on the distribution data also reveal the same. Another set of empirical functions are proposed that approximate the parameters λ, σ_0, σ_1, β_1, α_1 and k_1 as functions of the over-voltage ratio U and the atomic number of the matrix element Z. Curve fitting was also performed on these functions and they were indeed found to be good approximations. The drawbacks of the model include - slightly poor approximation near $\rho r = 0$ and the relatively large number of parameters required to estimate the model parameters from U and Z and their dependence on the X-ray line being measured. Nevertheless, the project shows that the generated X-ray intensity in two dimensions can indeed be modelled using empirical expressions and has revealed the challenges and limitations involved. Thus, we believe that the major goals of this project have been achieved.

5.1 Outlook

In this section possible improvements to the model suggested in this work as well as alternate techniques for modelling the distribution will be discussed.

The empirical model suggested in this work is fitted and thereby verified only on homogeneous single element bulk matrices. The implications of using homogeneous composition of elements as matrices on the proposed model must be investigated. Similarly, more types of samples such as thin layer samples, horizontal and vertical multi-layered samples and micro-particles must be investigated. The Monte-Carlo simulations used to acquire data can also be improved by carefully selecting the physical models used for the many interactions along simulated electron trajectories. For instance, the inclusion of secondary electron generation, which was ignored in the Monte-Carlo simulations used in the project, could be investigated. Insights from experimentally obtained X-ray intensity distribution can also be helpful.

A complete sensitivity analysis of the parameters in the empirical model must also be carried out. This can reveal flaws in the model and help in optimizing and making the model more manipulatable. Further, it would be helpful if the number of free parameters can be reduced. This can be done, for instance, by relating the obtained parameters to special features of the distribution such as the total ionization probability (area/volume under the X-ray intensity distribution) as is done in the PAP model [46] or to the physics and physical properties involved in the motion and scattering of electrons as is done in the modified Gaussian model for $\phi(\rho z)$ [42]. In our model, only the parameter k_1 is related to such a feature, i.e. the value $\phi(\rho z = 0)$ which has been studied by extensively in the context of thin film coatings [37], [3] [53] [32]. Restricting the parameters in this way will reduce the degrees of freedom for curve fitting, which will help avoid the common pitfalls of least squares curve-fitting such as convergence to local minima. It will also make the road for further improvements easier as better approximations are obtained for these individual features the function parameters could be based on.

Further, alternative ways to model the generated X-ray intensity distribution can be explored. One such way would be to model the electron energy density distribution N and then integrate it with the inelastic cross-section $Q_{nl}(E)$ separately to obtain the generated electron intensity distribution ϕ. The electron energy distribution has one more dimension than ϕ because it contains information about both the density of electrons in a region of the sample and the distribution of energies for the electrons in that region. Hence, it might be necessary to employ some form of dimensionality reduction to make this method viable. But, this method has the advantage of isolating the effect of the X-ray line being measured. Such a model would only have parameters that depend on the matrix and the electron beam unlike our model which currently has different sets of parameters depending on the X-ray line being measured.

References

[1] N Ammann. Monte carlo simulation der röntgenstrahlungs-erzeugung durch elektronenbeschuß in schicht-substrat-systemen. Master's thesis, RWTH Aachen University, 1989.

[2] John T. Armstrong. *Quantitative Elemental Analysis of Individual Microparticles with Electron Beam Instruments*, pages 261–315. Springer US, Boston, MA, 1991. ISBN 978-1-4899-2617-3. doi: 10.1007/978-1-4899-2617-3_15. URL https://doi.org/10.1007/978-1-4899-2617-3_15.

[3] H-J. August and J. Wernisch. Calculation and comparison of the surface ionization $\phi(0)$. *Scanning*, 12(1):14–22, 1990. doi: 10.1002/sca.4950120104. URL https://doi.org/10.1002/sca.4950120104.

[4] A. Azzalini. A class of distributions which includes the normal ones. *Scandinavian Journal of Statistics*, 12(2):171–178, 1985. ISSN 03036898, 14679469. URL http://www.jstor.org/stable/4615982.

[5] Ian Barkshire, Peter Karduck, Werner P. Rehbach, and Silvia Richter. High-spatial-resolution low-energy electron beam x-ray microanalysis. *Microchimica Acta*, 132(2):113–128, Apr 2000. ISSN 1436-5073. doi: 10.1007/s006040050052. URL https://doi.org/10.1007/s006040050052.

[6] M. J. Berger and S. M. Seltzer. Stopping powers and ranges of electrons and positrons, us dept. of commerce publ. no. nbsir 82-2550-a, 1983.

[7] H. Bethe. Zur theorie des durchgangs schneller korpuskularstrahlen durch materie. *Annalen der Physik*, 397(3):325–400, 1930. doi: 10.1002/andp.19303970303. URL https://onlinelibrary.wiley.com/doi/abs/10.1002/andp.19303970303.

[8] H. E. Bishop. Electron scattering in thick targets. *British Journal of Applied Physics*, 18(6):703–715, jun 1967. doi: 10.1088/0508-3443/18/6/302. URL https://doi.org/10.1088%2F0508-3443%2F18%2F6%2F302.

[9] David Bote and Francesc Salvat. Calculations of inner-shell ionization by electron impact with the distorted-wave and plane-wave born approximations. *Phys. Rev. A*, 77:042701, Apr 2008. doi: 10.1103/PhysRevA.77.042701. URL https://link.aps.org/doi/10.1103/PhysRevA.77.042701.

[10] David Bote, Francesc Salvat, Aleksander Jablonski, and Cedric J. Powell. Cross sections for ionization of k, l and m shells of atoms by impact of electrons and positrons with energies up to 1gev: Analytical formulas. *Atomic Data and Nuclear Data Tables*, 95(6):871 – 909, 2009. ISSN 0092-640X. doi: 10.1016/j.adt.2009.08.001. URL https://doi.org/10.1016/j.adt.2009.08.001.

[11] Mary Ann Branch, Thomas F. Coleman, and Yuying Li. A subspace, interior, and conjugate gradient method for large-scale bound-constrained minimization problems. *SIAM Journal on Scientific Computing*, 21(1):1–23, 1999. doi: 10.1137/S1064827595289108. URL https://doi.org/10.1137/S1064827595289108.

[12] J. Bünger, S. Richter, and M. Torrilhon. A deterministic model of electron transport for electron probe microanalysis. In *IOP Conference Series: Materials Science and Engineering*, volume 304, page 012004. IOP Publishing, jan 2018. doi: 10.1088/1757-899x/304/1/012004. URL https://doi.org/10.1088%2F1757-899x%2F304%2F1%2F012004.

[13] E. Casnati, A. Tartari, and C. Baraldi. An empirical approach to k-shell ionisation cross section by electrons. *Journal of Physics B: Atomic and Molecular Physics*, 15(1):155–167, jan 1982. doi: 10.1088/0022-3700/15/1/022. URL https://doi.org/10.1088%2F0022-3700%2F15%2F1%2F022.

[14] R. Castaing. *Application of electron probes to metallographic analysis*. PhD thesis, University of Paris, 1951.

[15] Raymond Castaing. Electron probe microanalysis. *Advances in electronics and electron physics*, 13:317–386, 1960.

[16] Raymond Castaing and Jacques Descamps. Sur les bases physiques de l'analyse ponctuelle par spectrographie x. *J. Phys. Radium*, 16(4):304–317, 1955. doi: 10.1051/jphysrad:01955001604030400. URL https://doi.org/10.1051/jphysrad:01955001604030400.

[17] C. T. Chantler. Detailed tabulation of atomic form factors, photoelectric absorption and scattering cross section, and mass attenuation coefficients in the vicinity of absorption edges in the soft x-ray ($z = 30^{\smile}36$, $z = 60^{\smile}89$, $e = 0.1\,kev$–$10\,kev$), addressing convergence issues of earlier work. *Journal of Physical and Chemical Reference Data*, 29(4):597–1056, 2000. doi: 10.1063/1.1321055. URL https://doi.org/10.1063/1.1321055.

[18] Hendrix Demers, Paula Horny, Raynald Gauvin, and Eric Lifshin. Winx-ray: A new monte carlo program for the simulation of x-ray and charging materials. *Microscopy and Microanalysis*, 8(S02):1498–1499, 2002. doi: 10.1017/S1431927602104120. URL https://doi.org/10.1017/S1431927602104120.

[19] Richard D. Deslattes, Ernest G. Kessler, P. Indelicato, L. de Billy, E. Lindroth, and J. Anton. X-ray transition energies: new approach to a comprehensive evaluation. *Rev. Mod. Phys.*, 75:35–99, Jan 2003. doi: 10.1103/RevModPhys.75.35. URL https://link.aps.org/doi/10.1103/RevModPhys.75.35.

[20] Z. -J. Ding, R. Shimizu, and K. Obori. Monte carlo simulation of x-ray spectra in electron probe microanalysis: Comparison of continuum with experiment. *Journal*

of Applied Physics, 76(11):7180–7187, 1994. doi: 10.1063/1.357998. URL https://doi.org/10.1063/1.357998.

[21] Dominique Drouin, Alexandre Réal Couture, Dany Joly, Xavier Tastet, Vincent Aimez, and Raynald Gauvin. Casino v2. 42—a fast and easy-to-use modeling tool for scanning electron microscopy and microanalysis users. *Scanning: The Journal of Scanning Microscopies*, 29(3):92–101, 2007. doi: 10.1002/sca.20000. URL https://doi.org/10.1002/sca.20000.

[22] H. J. Fitting and J. Reinhardt. Monte-carlo simulation of kev-electron scattering in solid targets. *physica status solidi (a)*, 88(1):245–259, 1985. doi: 10.1002/pssa.2210880127. URL https://onlinelibrary.wiley.com/doi/abs/10.1002/pssa.2210880127.

[23] J. I. Goldstein and R. E. Ogilvie. A re-evaluation of the iron-rich portion of the fe-ni system. *AIME MET SOC TRANS*, 233(12):2083–2087, 1965.

[24] Joseph I. Goldstein, Dale E. Newbury, Patrick Echlin, David C. Joy, Charles E. Layman, Eric Lifshin, Linda Sawyer, and Joseph R. Michael. *Scanning Electron Microscopy and X-Ray Microanalysis*. Springer, 2003. ISBN 978-0-306-47292-3. doi: 10.1007/978-1-4615-0215-9.

[25] M. Green. A monte carlo calculation of the spatial distribution of characteristic x-ray production in a solid target. *Proceedings of the Physical Society*, 82(2):204–215, aug 1963. doi: 10.1088/0370-1328/82/2/307. URL https://doi.org/10.1088%2F0370-1328%2F82%2F2%2F307.

[26] M. Green. The angular distribution of characteristic x radiation and its origin within a solid target. *Proceedings of the Physical Society*, 83(3):435–451, mar 1964. doi: 10.1088/0370-1328/83/3/311. URL https://doi.org/10.1088%2F0370-1328%2F83%2F3%2F311.

[27] Kurt F. J. Heinrich. *Electron beam X-ray microanalysis*. Van Nostrand Reinhold Co., 1981. ISBN 9780442232863.

[28] A. Jablonski, F. Salvat, and C. J. Powell. Evaluation of elastic-scattering cross sections for electrons and positrons over a wide energy range. *Surface and Interface Analysis*, 37(12):1115–1123, 2005. doi: 10.1002/sia.2123. URL https://onlinelibrary.wiley.com/doi/abs/10.1002/sia.2123.

[29] D. C. Joy and S. Luo. An empirical stopping power relationship for low-energy electrons. *Scanning*, 11(4):176–180, 1989. doi: 10.1002/sca.4950110404. URL https://doi.org/10.1002/sca.4950110404.

[30] David C. Joy. An introduction to monte carlo simulations. *Scanning microscopy*, 5(2):329–337, 1991. URL http://www.geology.wisc.edu/~johnf/g777/ScanMicro/Joy_MC_1991_a5.pdf.

[31] K. Kanaya and S. Okayama. Penetration and energy-loss theory of electrons in solid targets. *Journal of Physics D: Applied Physics*, 5(1):43–58, jan 1972. doi: 10.1088/0022-3727/5/1/308. URL https://doi.org/10.1088%2F0022-3727%2F5%2F1%2F308.

[32] Peter Karduck and Werner Rehbach. *The use of Tracer Experiments and Monte Carlo Calculations in the $\phi(\rho z)$ Determination for Electron Probe Microanalysis*, pages 191–217. Springer US, 1991. ISBN 978-1-4899-2617-3. doi: 10.1007/978-1-4899-2617-3_4. URL https://doi.org/10.1007/978-1-4899-2617-3_4.

[33] Masatoshi Kotera, Kenji Murata, and Koichi Nagami. Monte carlo simulation of 1–10-kev electron scattering in a gold target. *Journal of Applied Physics*, 52 (2):997–1003, 1981. doi: 10.1063/1.328746. URL https://doi.org/10.1063/1.328746.

[34] H. W. Lewis. Multiple scattering in an infinite medium. *Phys. Rev.*, 78:526–529, Jun 1950. doi: 10.1103/PhysRev.78.526. URL https://link.aps.org/doi/10.1103/PhysRev.78.526.

[35] Xavier Llovet and Francesc Salvat. Penepma: A monte carlo program for the simulation of x-ray emission in electron probe microanalysis. *Microscopy and Microanalysis*, 23(3):634–646, 2017. doi: 10.1017/S1431927617000526. URL https://doi.org/10.1017/S1431927617000526.

[36] G. Love, M. G. C. Cox, and V. D. Scott. A simple monte carlo method for simulating electron-solid interactions and its application to electron probe microanalysis. *Journal of Physics D: Applied Physics*, 10(1):7–23, jan 1977. doi: 10.1088/0022-3727/10/1/002. URL https://doi.org/10.1088%2F0022-3727%2F10%2F1%2F002.

[37] G. Love, M. G. Cox, and V. D. Scott. The surface ionisation function $\phi(0)$ derived using a monte carlo method. (correction procedure development for electron-probe microanalysis). *Journal of Physics D: Applied Physics*, 11(1):23–31, jan 1978. doi: 10.1088/0022-3727/11/1/005. URL https://doi.org/10.1088%2F0022-3727%2F11%2F1%2F005.

[38] Niklas Mevenkamp. Inverse modeling in electron probe microanalysis based on deterministic transport equations. Master's thesis, RWTH Aachen, 2016.

[39] Kenji Murata, Takayuki Matsukawa, and Ryuichi Shimizu. Monte carlo calculations on electron scattering in a solid target. *Japanese Journal of Applied Physics*, 10(6):678–686, jun 1971. doi: 10.1143/jjap.10.678. URL https://doi.org/10.1143%2Fjjap.10.678.

[40] Robert L. Myklebust, Dale E. Newbury, and Harvey Yakowitz. Nbs m0nte carl0 electr0n traject0ry calculati0n pr0gram. In *Use of Monte Carlo calculations in electron probe microanalysis and scanning electron microscopy: proceedings of a*

workshop held at the National Bureau of Standards, Gaithersburg, Maryland, October 1-3, 1975, number 460, page 105. US Dept. of Commerce, National Bureau of Standards: for sale by the Supt. of Docs., US Govt., 1976.

[41] A. O'Hagan and Tom Leonard. Bayes estimation subject to uncertainty about parameter constraints. *Biometrika*, 63(1):201–203, 04 1976. ISSN 0006-3444. doi: 10.1093/biomet/63.1.201. URL https://doi.org/10.1093/biomet/63.1.201.

[42] R. H. Packwood and J. D. Brown. A gaussian expression to describe $\phi(\rho z)$ curves for quantitative electron probe microanalysis. *X-Ray Spectrometry*, 10(3):138–146, 1981. doi: 10.1002/xrs.1300100311. URL https://onlinelibrary.wiley.com/doi/abs/10.1002/xrs.1300100311.

[43] J. Philbert. A method for calculating the absorption correction in electron-probe microanalysis. In H. H. Pattee, V. E. Cosslett, and Arne Engström, editors, *X-ray Optics and X-ray Microanalysis*, pages 379 – 392. Academic Press, 1963. ISBN 978-1-4832-3322-2. doi: https://doi.org/10.1016/B978-1-4832-3322-2.50039-1. URL http://www.sciencedirect.com/science/article/pii/B9781483233222500391.

[44] J. Philibert and R. Tixier. Electron penetration and the atomic number correction in electron probe microanalysis. *Journal of Physics D: Applied Physics*, 1(6):685–694, jun 1968. doi: 10.1088/0022-3727/1/6/302. URL https://doi.org/10.1088%2F0022-3727%2F1%2F6%2F302.

[45] P. T. Pinard and S. Richter. Improving the quantification at high spatial resolution using a field emission electron microprobe. In *IOP Conference Series: Materials Science and Engineering*, volume 55, page 012016. IOP Publishing, 2014.

[46] Jean-Louis Pouchou and Françoise Pichoir. *Quantitative Analysis of Homogeneous or Stratified Microvolumes Applying the Model "PAP"*, pages 31–75. Springer US, 1991. ISBN 978-1-4899-2617-3. doi: 10.1007/978-1-4899-2617-3_4. URL https://doi.org/10.1007/978-1-4899-2617-3_4.

[47] C. J. Powell. Cross sections for inelastic electron scattering in solids. *Ultramicroscopy*, 28(1):24 – 31, 1989. ISSN 0304-3991. doi: 10.1016/0304-3991(89)90264-7. URL https://doi.org/10.1016/0304-3991(89)90264-7.

[48] C. J. Powell, A. Jablonski, and F. Salvat. Nist databases with electron elastic-scattering cross sections, inelastic mean free paths, and effective attenuation lengths. *Surface and Interface Analysis*, 37(11):1068–1071, 2005. doi: 10.1002/sia.2098. URL https://onlinelibrary.wiley.com/doi/pdf/10.1002/sia.2098.

[49] C. A. Quarles. Semiempirical analysis of electron-induced k-shell ionization. *Phys. Rev. A*, 13:1278–1280, Mar 1976. doi: 10.1103/PhysRevA.13.1278. URL https://link.aps.org/doi/10.1103/PhysRevA.13.1278.

[50] S. J. B. Reed. Characteristic fluorescence corrections in electron-probe microanalysis. *British Journal of Applied Physics*, 16(7):913–926, jul 1965. doi: 10.1088/0508-3443/16/7/301. URL https://doi.org/10.1088%2F0508-3443%2F16%2F7%2F301.

[51] Stephen Jarvis Brent Reed. *Electron microprobe analysis and scanning electron microscopy in geology*. Cambridge university press, 2005.

[52] L. Reimer, H. Seidel, and H. Gilde. Einfluss der elektronendiffusion auf die bildentstehung im raster-elektronen-mikroskop. *Beitr. Elektronmikrosk. Direktabb. Oberfl.(Munster)*, 1:53, 1968.

[53] W Reuter. The ionization function and its application to the electron probe analysis of thin films. In *Proceedings of the sixth international conference on x-ray optics and microanalysis*, pages 121–137. University of Tokyo Press, 1972.

[54] Silvia Richter and Gemeinschaftslabor für Elektronenmikroskopie. Electron probe micro analyser. URL http://www.gfe.rwth-aachen.de/seiteninhalte_english/esma.htm. [Online; accessed April 18, 2020].

[55] Romano Rinaldi and Xavier Llovet. Electron probe microanalysis: A review of the past, present, and future. *Microscopy and Microanalysis*, 21(5):1053–1069, 2015. doi: 10.1017/S1431927615000409. URL https://doi.org/10.1017/S1431927615000409.

[56] Nicholas W. M. Ritchie. A new monte carlo application for complex sample geometries. *Surface and Interface Analysis*, 37(11):1006–1011, 2005. doi: 10.1002/sia.2093. URL https://onlinelibrary.wiley.com/doi/abs/10.1002/sia.2093.

[57] Nicholas WM Ritchie. Getting started with nist* dtsa-ii. *Microscopy Today*, 19(1):26–31, 2011. URL http://www.geoscience.wisc.edu/~johnf/g777/Ritchie2011a-MT.pdf.

[58] José A. Riveros, Gustavo E. Castellano, and Jorge C. Trincavelli. Comparison of ϕ (ρz) curve models in epma. In Abraham Boekestein and Miodrag K. Pavićević, editors, *Electron Microbeam Analysis*, pages 99–105, Vienna, 1992. Springer Vienna. ISBN 978-3-7091-6679-6.

[59] Francesc Salvat, José M Fernández-Varea, and Josep Sempau. Penelope-2006: A code system for monte carlo simulation of electron and photon transport. In *Workshop proceedings*, volume 4, page 7. Nuclear Energy Agency, Organization for Economic Co-operation and Development, 2006. URL http://www.asl-i.com/contents/upload-docs/201466123234.pdf.

[60] Ryuichi Shimizu and Kenji Murata. Monte carlo calculations of the electron-sample interactions in the scanning electron microscope. *Journal of Applied Physics*, 42(1):387–394, 1971. doi: 10.1063/1.1659606. URL https://doi.org/10.1063/1.1659606.

[61] CAMECA Science & Technology Solutions. Electron probe micro analyser, 2020. URL https://www.cameca.com/products/epma/technique. [Online; accessed April 18, 2020].

[62] J. Wernisch, C. Pöhn, W. Hanke, and H. Ebel. μ/ρ algorithm valid for $1\,kev \leq e \leq 50\,kev$ and $11 \leq z \leq 83$. *X-Ray Spectrometry*, 13(4):180–181, 1984. doi: 10.1002/xrs.1300130411. URL https://doi.org/10.1002/xrs.1300130411.

[63] Peter Willich and Reinhold Bethke. Practical aspects and applications of epma at low electron energies. In *Microbeam and nanobeam analysis*, pages 631–638. Springer, 1996.